Proton-^{3}He Elastic Scattering at Low Energies and the "A_y Puzzle"

by

Brian Michael Fisher

A dissertation submitted to the faculty of the University of North Carolina at Chapel Hill in partial fulfillment of the requirements for the degree of Doctor of Philosophy in the Department of Physics and Astronomy.

Chapel Hill

2003

Approved:

E. J. Ludwig, Advisor

H. J. Karwowski, Reader

T. B. Clegg, Reader

ABSTRACT

BRIAN MICHAEL FISHER: Proton-^{3}He Elastic Scattering at Low Energies and the "A_y Puzzle"
(Under the Direction of E. J. Ludwig)

Angular distributions of cross sections $\sigma(\theta)$ and proton analyzing powers A_y have been measured for proton-^{3}He elastic scattering at several energies at and below 5 MeV. A supersonic gas jet target has been refurbished, improved, and installed allowing these low energy cross section measurements to be performed. The $\sigma(\theta)$ distributions have been measured at $E_p = 0.99$, 1.59, 2.24, 3.11, and 4.02 MeV. Full angular distributions of A_y have been measured at $E_p = 1.60$, 2.25, 3.13, and 4.05 MeV. These data have been compared with recent theoretical calculations made using realistic two- and three-nucleon interactions. Using the Argonne v_{18} nucleon-nucleon potential and the Urbana IX three-nucleon interaction, these calculations show discrepancies from the measured $\sigma(\theta)$ distributions on the $\approx 5\%$ level, which increase at backward angles. When the measured A_y distributions are compared with the theoretical calculations, much larger discrepancies of approximately 40% are seen at the maximum of each distribution. The addition of the Urbana IX three-nucleon interaction has virtually no effect on this difference. This is analogous to the existing "A_y Puzzle" known for the past 20 years in nucleon-deuteron elastic scattering. Single energy phase-shift analyses have been performed on these new data. They show that increases ($\lessapprox 20\%$) relative to the theoretical predictions in key phase shifts and mixing parameters greatly improve the description of the new data.

ACKNOWLEDGMENTS

I arrived in Chapel Hill in June 1996 fairly certain that I wanted to study experimental nuclear physics. Now, seven[1] years later, I'm quite confident that I made the right decision. I have been very lucky to be able to work with a marvelously talented extended-family of professors, graduate students, technicians, and support staff, all of whom I feel immensely fortunate to be able to also call good friends. The work described in this document is as much theirs as it is mine.

My academic sages, Dr. Ed Ludwig and Dr. Hugon Karwowski, have provided excellent guidance, encouragement, and advice during this project. Under their tutelage, I've grown immensely as a scientist and as a human being. I have also benefited greatly from the advice of Dr. Carl Brune and Dr. Tom Clegg, both of whom have provided excellent advice when I was wrestling with experimental problems.

Experimental nuclear physics, perhaps more-so than in most scholarly endeavors, is a group activity. As a young graduate student, I learned much from those who came before me. Bill Geist, Kevin Veal, and Mike Wood were marvelous tutors in experimental setup, data acquisition, and data analysis. Without the TUNL technical staff of Chris Westerfeldt, John Dunham, Paul Carter, and especially Richard O'Quinn, the gas-jet target would've never become operational. Their contribution to this work is immeasurable.

Professors and graduate students alike put in long hours during my experimental runs. Mike Wood, Doug Leonard, Dhruba Gupta, Tatsuya Katabuchi, Dr. Tim Black, Geoff Milanovich, and Andy Danner all helped immensely. Shane Canon helped me port the XSYS software to Linux, and Alex Crowell and Sidney Edwards were always

[1] Pretty long eh?

there to help solve computer problems. Fellow research troglodytes Ryan Fitzgerald, Bob Runkle, Mitzi Boswell, and Tim Daniels have been great colleagues, friends, and lunch-buddies. Carrie Rowland, in particular, has been great help, a wonderful friend and commiserator, and fellow 3pm Bryan Center snack-er.

Our theoretical colleagues in Pisa, Italy – the prime motivators for this project – have also been a pleasure to work with and I have learned much from them. I'm grateful to Dr. Alejandro Kievsky for his ability to clearly explain the relevant theoretical issues to me. Dr. Michele Viviani has been a great help both by providing the theoretical calculations shown in this work, and in helping me with the development of the phase-shift analysis code that I used. The hospitality that Drs. Kievsky and Viviani showed during my stay in Pisa is very much appreciated.

My undergraduate physics education at SUNY-Geneseo was a very good preparation for graduate school. I feel truly blessed to have been involved in such a close-knit department where quality teaching is valued so strongly. Dr. Steve Padalino and Dr. Kurt Fletcher guided me through my first research experiences, and showed me how interesting and fun experimental nuclear physics can be. The physics department at SUNY-G should be held up as an example as to how an academic department at a university should be run.

Making this great "Carolina Experience" that much better, have been my friends outside of the laboratory. Terry Steckowich, Hank Tomlinson, Scott Boger, Rob Fox, Todd Steinwart, Kevin Brown, Christopher Gobert, Brian Martin, Andy Jacobs, Matt Hawkins, Ross Bradford, and Matt Guzy (among others) have all been there to help me enjoy my time away from the laboratory. I am especially grateful to Neil Watson for being such a good friend and neighbor. And my appreciation of my friendship with Jeffery DiFranco can not be adequately put into words.

Lastly, I have to thank my family. My parents Carole and Larry, while (understandably) not always comprehending why it took seven years for me to get to this point (I'm not entirely sure either, but here I am), have always been patient, supportive and amazingly generous. My sister Lisa and my brother-in-law Paul have also been great cheerleaders. Without all their support and understanding I could not have

made it this far in life. I love them all dearly.

Thank you all very much!

Brian Michael Fisher

June 2003

to my parents

CONTENTS

LIST OF TABLES

LIST OF FIGURES

Chapter 1

Introduction

The fundamental interaction between nucleons is a tangled, knotty problem at the heart of nuclear physics. Partially because of the myriad phenomena appearing in nature resulting from the interactions between nucleons, and partially because of the apparent complexity of the interaction and lack of a coherent underlying theoretical description, nuclear systems have often been described as "pathologically complicated." [Bed02]. The forces between constituent nucleons are strong and non-central, and the relatively small binding found in nuclei results from very precise cancellations between large competing contributions. Given our incomplete knowledge of the basic interaction between nucleons, especially at short distances, and given the difficulties of the numerical solution of the Schrödinger equation for systems with many fermions, it becomes clear why a sound microscopic description of nuclear structure remains an unsolved problem after many decades of heroic – perhaps Sisyphean – effort. However, despite (or perhaps because of) these difficulties, nuclear physics remains a vibrant, healthy, and active field.

We do know that Quantum Chromodynamics (QCD) *is* the theory of the fundamental interactions of the quarks and gluons that make up nucleons. It is so mathematically intractable that in its present state a detailed description of the interaction between two nucleons is very, very difficult, if not impossible. All nuclear processes are encoded in the QCD Lagrangian and, it is thought, parameter-free predictions could, in principle, be obtained. These would transform nuclear physics from a field

predominantly driven by phenomenology to a (potentially less interesting and less vibrant) field with much stronger theoretical foundations. It is this link that brings the high-energy realm of QCD to the lower energy realm of "traditional" meson-exchange interactions. Yet a complete picture of the nucleon-nucleon (NN) interaction continues to elude theorists.

That is not to say that nuclear physicists are adrift with no coherent picture of nuclei. Especially at low energies, the meson-exchange picture of the NN interaction has provided a very good description of nucleon dynamics. The one-pion-exchange potential (OPEP) [Yuk35], the basis for the long-range part of all modern NN potential models, describes the gross properties of the NN interaction very well; its short range, non-centrality, and strong spin dependence all arise from the exchange of virtual pions between nucleons. Much more sophisticated NN models, which will be discussed in Section 2.1, have grown out of the OPEP, which then include the spin-dependence, strongly repulsive core, and the (small) charge-symmetry and charge-independence breaking seen in experiments. These potentials describe a culled NN database below 300 MeV with a nearly perfect χ^2/datum ≈ 1 [Car98]. These potentials and the computational methods in which they are used to make predictions for larger nuclear systems will be discussed in Chapter 2.

Measurements of few nucleon observables provide very stringent tests of these interactions, and can provide confidence in their predictions of processes that cannot be measured in the laboratory. When these models do not predict the experimental data well that, at the very least, the weaknesses in the models can be discovered and fixed, or at the very most, we catch a glimpse of potentially new physics.

The long-standing "A_y puzzle", described below in Section 1.1, is an obvious instance of where the existing models do not accurately predict experimental observables, and fail rather spectacularly. While it is not the only discrepancy between theory and experiment in few-nucleon research (for instance, the Nd-star anomaly [How01]), it is certainly one of the most pronounced. This particularly stubborn problem provides motivation for investigations on many fronts in few-nucleon research, and is the primary motivation for this work.

1.1 The "A_y Puzzle"

The term "A_y puzzle" – or more precisely the nucleon-deuteron (Nd) analyzing power puzzle – refers to the inability of modern nucleon-nucleon models to describe the nucleon vector analyzing powers in Nd elastic scattering below an incident laboratory energy of $E_d = 30$ MeV [Glö96]. This under-prediction of analyzing powers became immediately evident once it was possible to perform calculations using realistic potential models that reproduced the NN database with high accuracy [Sto78, Koi78]. It became apparent that this "puzzle" was a very real discrepancy once a large-scale program of rigorous three-nucleon continuum Faddeev calculations for neutron-deuteron elastic scattering was initiated [Wit89]. Similarly, once calculations for proton-deuteron elastic scattering that treated the Coulomb interaction in a rigorous manner became available [Kie94, Kie95], showing the same $\approx 30\%$ under-prediction in the proton A_y and deuteron vector analyzing power iT_{11}, the large-scale systemic nature of the "A_y puzzle" became firmly established.

Conventional three-nucleon forces are needed to correctly predict the binding energy of ^{3}H and ^{3}He. When they are added to a realistic NN potential, the predictions for the Nd analyzing powers change only slightly, and generally do not significantly improve [Wit94, Kie95]. (Three-nucleon forces are discussed in Section 2.2.) As an example of the A_y puzzle, Figure 1.1 shows the proton-deuteron elastic scattering data at $E_{\text{c.m.}} = 667$ keV of Wood *et al.* compared with theoretical calculations using, first a two-nucleon potential (AV18) alone, and then including a three-nucleon potential (UR(IX)) [Woo02]. The calculations provide a very good description of the tensor analyzing powers and cross section (χ^2/datum ≈ 1 [Kie01]), but there is a very large discrepancy for both the proton analyzing power A_y and the deuteron vector analyzing power iT_{11}.

Since the discrepancy is seen in both p-d and n-d elastic scattering, and is seen no matter which realistic potential or computational method is used, the problem seems to be with the potentials themselves. There does seem to be a tantalizing difference in the energy dependence of this discrepancy, as discussed in [Nei03] and shown in

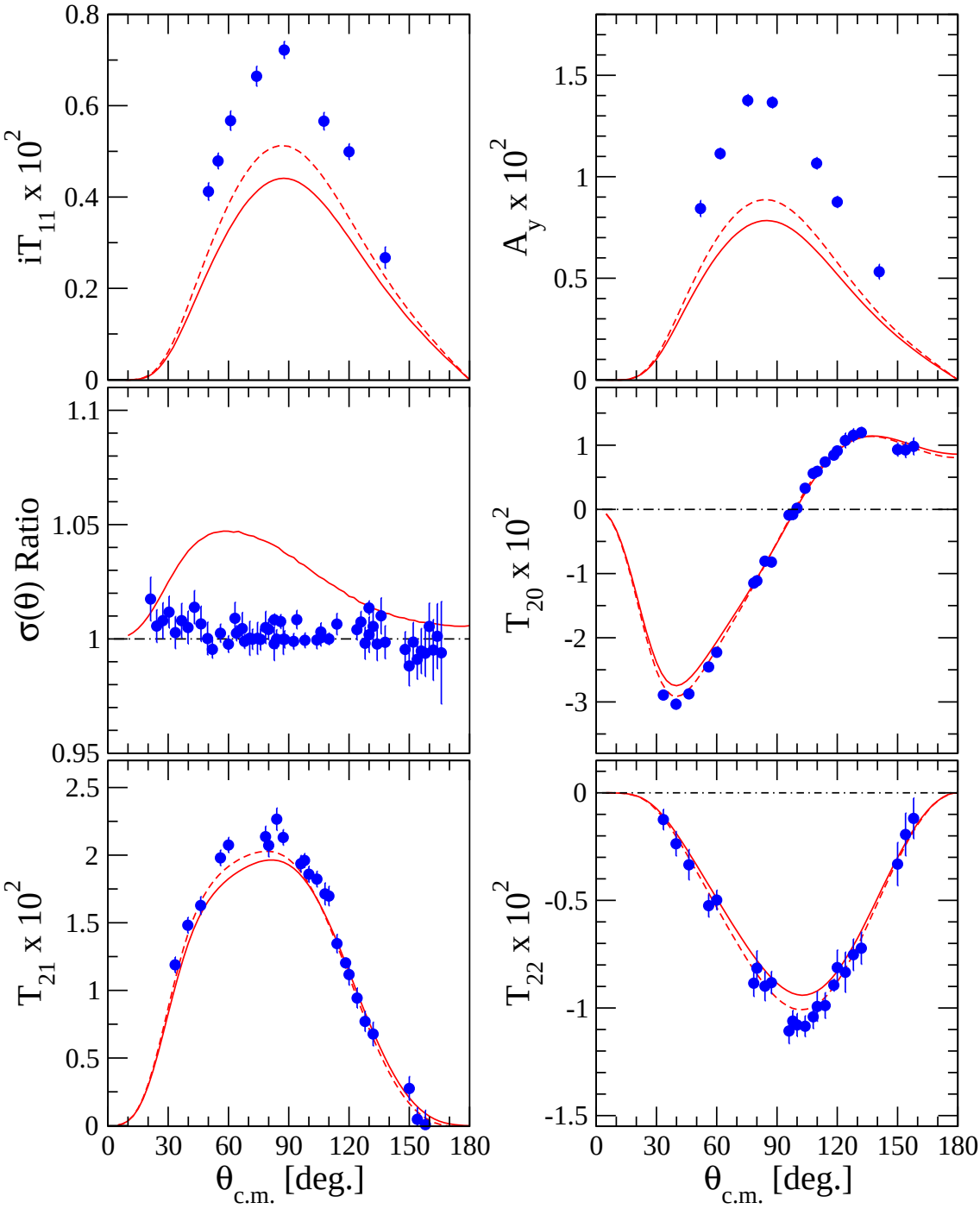

Figure 1.1: Angular distributions of $\sigma(\theta)$ and analyzing powers for p-d elastic scattering at $E_{\text{c.m.}} = 667$ keV, from [Woo02]. For all analyzing power plots shown, the solid and dashed curves are variational calculations with the AV18 and AV18 + UR(IX) potentials, respectively. The plot labeled "$\sigma(\theta)$ Ratio" shows the ratio of the cross-section to the AV18 + UR(IX) calculation, and the dots are the data divided by the AV18 + UR(IX) calculation. The solid line is the ratio of the AV18 calculation to the AV18 + UR(IX) calculation.

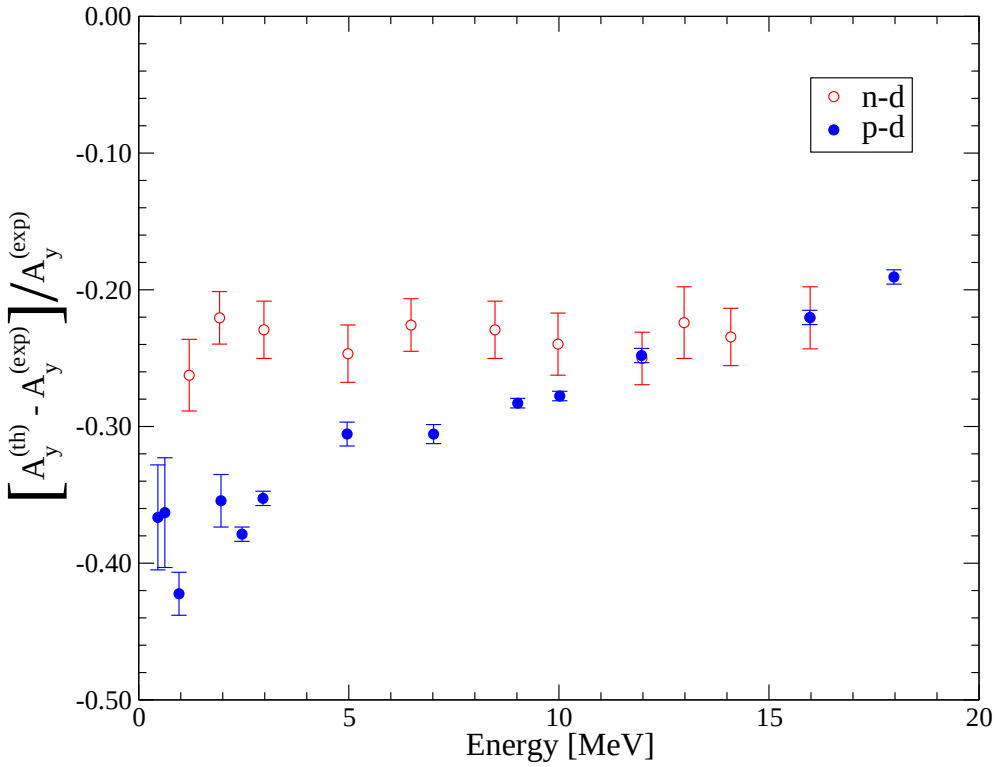

Figure 1.2: Comparison of the relative difference between calculations and data for A_y in n-d and p-d elastic scattering at the maximum of the distribution. The calculations were performed using the AV18 NN potential model. Taken from [Nei03].

Figure 1.2. In the p-d case the discrepancy grows in size with decreasing energy; however in the n-d case the data shows a constant 30% underprediction at energies below 20 MeV. Current theoretical discussions center around whether the problem is in the NN part of the potential (which describes the 4000+ datum NN database so well) [Bit79a, Wit91, Tor98, Ent02] or from an incomplete description of three-nucleon interaction [Hüb98, Bru98, Kie99], or even a "smoking gun" for new physics [Can01]. Potential solutions to the A_y puzzle will be discussed in Chapter 7.

1.2 Proton-^{3}He Elastic Scattering

Since the A_y puzzle is firmly established in the three-nucleon system, we can start to look to other systems for clues to its solution. The $A = 4$ system, with the advent of computational techniques and the computational power capable of performing *ab*

initio calculations, has increasingly become another testing ground for models of the nuclear force. While not the "imbroglio" [Car01] of levels as in heavy nuclei, the $A = 4$ system is the simplest system that presents the complexity – thresholds and resonances – that characterize nuclear systems [Til92].

It is with this intent to broaden the scope of the search for three-nucleon force effects and to look for their potential effects in a different system that measurements of proton-^{3}He elastic scattering cross sections and analyzing powers at energies below 5 MeV have been made.

1.2.1 Motivation

There are several reasons why the proton-^{3}He system is appealing for further study. Nucleons in ^{3}He are closer together ($E_b = 7.72$ MeV) than in the deuteron ($E_b = 2.225$ MeV), which may enhance three-nucleon force (3NF) effects, since they are thought to be short-ranged. The closer proximity of the three nucleons in ^{3}He could result in larger analyzing power (and perhaps even cross section) discrepancies from predictions using the standard two- and three-nucleon potentials.

Theoretical techniques have advanced to the point where calculations of these observables in the $A = 4$ system have become possible. These experiments provide a stringent test of present theoretical calculations. Accurate wavefunctions from such calculations are also of great interest in calculations of the astrophysically significant $p + {}^3\mathrm{He} \rightarrow {}^4\mathrm{He} + \nu_\mathrm{e} + \mathrm{e}^+$ reaction.

Simplifying the quest for clear indications of three-nucleon interaction effects, *four*-nucleon force effects do not seem to play a strong role. Calculations of the binding energy of the α-particle using potentials with $3N$-forces included do not show discrepancies from the experimental value. A discussion of this is given in Section 2.3 and a summary of the results is given in Table 2.2.

1.2.2 Previous Work – Experiment

The first theoretical calculations specifically for proton-^{3}He elastic scattering that can be found in the literature were performed in 1953 by Swan using several simple nuclear interaction models in a variational approach [Swa53]. The first measurements of the cross-section followed shortly in 1954 by Famularo *et al.* [Fam54][2], where $\sigma(\theta)$ measurements were made at four energies between 1 and 3.5 MeV. The first proton polarization data were taken in 1964 by McDonald *et al.* using the double-scattering method [McD64]. Other polarization observables followed; A_{0y} first in 1970 [McS70] and spin correlation coefficients in 1969 [McS69], and polarization transfer coefficients in 1976 [Har76].

Since 1955, there have been many measurements of $\sigma(\theta)$, A_y, and other spin observables at energies below 5 MeV. Table 1.1 summarizes the previous p-^{3}He elastic scattering measurements performed at proton energies at or below 5 MeV. A graphical representation of the same information for $\sigma(\theta)$ and A_y data-sets is given in Figure 1.3. In the region between $E_{\rm p} = 1$ and 4 MeV there is a dearth of high-quality $\sigma(\theta)$ data. Only the poorly-documented data of [Fam54] (the very first p-^{3}He data to be taken) exists in this energy region, and there are no complementary A_y measurements at the same energies (despite the large number of distributions measured.) There are many measurements of angular distributions of A_y in this region, though historically they have been fraught with problems. For instance, the data of Drigo *et al.* [Dri66] were found to be problematic in the R-Matrix analysis of Detomo *et al.* [Det79], which remeasured many A_y distributions as shown in Figure 1.3.

With this increasing database of proton-^{3}He elastic scattering data, there have been many attempts at performing phase-shift analyses, with limited success. Table 1.1 also lists these previous analyses, whether they were reported with experimental

[2]The reference [Fam54] is just a one-paragraph conference-proceedings abstract and contains no published data. The data-sets, however, were obtained from E. A. George [Geo98] at The University of Wisconsin at Madison. From where they were obtained is unclear. The apparatus with which the data were obtained is described in [Bro52].

Table 1.1: Previous p-^{3}He elastic scattering experiments at $E_{\rm p} \leq 5.0$ MeV. Papers which include a phase-shift analysis are indicated in the PSA column. Similarly, papers included in the analysis of [All93b] are indicated in the final column.

Reference	$E_{\rm p}$ [MeV]	Observable	PSA	In [All93b]?
[Fam54]	1.01 - 3.53	$\sigma(\theta)$		✓
[Low54]	1.0 - 3.5	PSA Only	✓	
[Fra55]	1.0 - 3.5	PSA Only	✓	
[Tom62]	2.01 - 4.54	$\sigma(\theta)$	✓	[b]
[Cle64]	4.55 - 11.48	$\sigma(\theta)$	✓	✓
[McD64]	4.05 - 12.79	$\sigma(\theta)$, A_{y0}		✓
[Tom65]	1.0 - 11.5	PSA Only	✓	
[Kav66]	0.125 - 2.0	$\sigma(\theta)$ [a]	✓	[c]
[Dri66]	3.38 - 4.46	A_{y0}		[b]
[Mor69]	4.0 - 10.8	A_{y0}	✓	✓
[McS70]	3.86 - 10.94	A_{0y}	✓	✓
[Bos72]	4.0 - 10.77	PSA Only	✓	
[Sza78a]	2.3 - 8.8	A_{0y}		✓
[Sza78b]	2.3 - 13.6	PSA Only	✓	
[Det79]	1.75 - 4.50	A_{y0}	✓	✓
[Ber80]	0.3 - 1.0	$\sigma(\theta)$, A_{y0}	✓	[c]
[Bel85]	0 - 10	PSA Only	✓	
[All93a]	4.01 - 10.01	A_{y0}, A_{0y}, A_{yy}		✓
[All93a]	5.54	A_{xx}, A_{xz}, A_{zx}, A_{zz}		✓
[All93b]	0 - 12	PSA Only	✓	
[Yos00]	4.0 - 19.48	PSA Only	✓	
[Viv01]	1.6, 2.25	A_{y0}		

[a] Excitation function performed at $\theta_{\rm lab} = 90^\circ$

[b] Excluded from [All93b].

[c] Not mentioned in [All93b] at all.

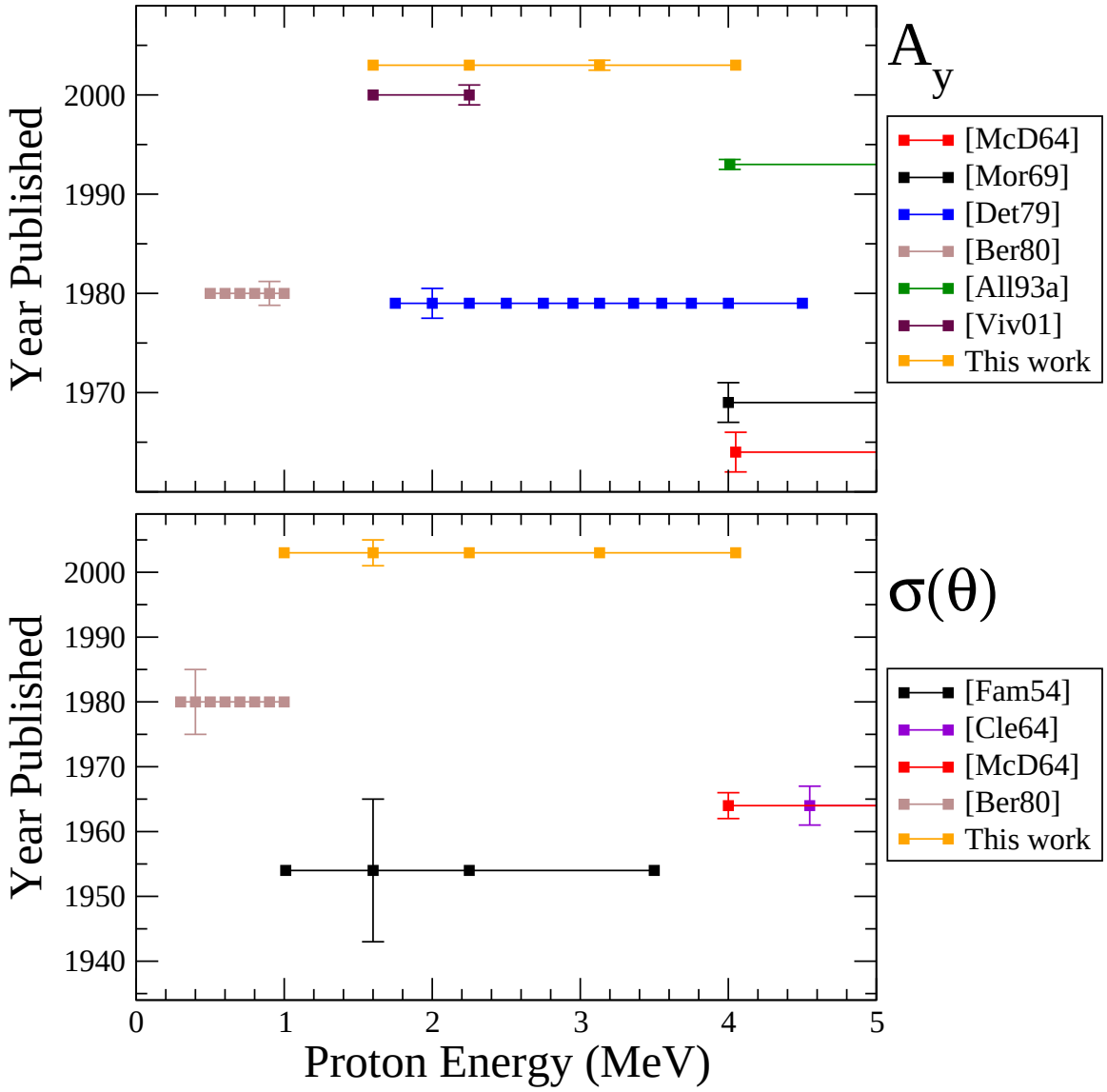

Figure 1.3: World p-^{3}He $\sigma(\theta)$ and A_y data-sets. The horizontal axis represents the proton energy at which the data were taken and the vertical axis gives the year that the data were published. The error bar on each data set gives a relative measure of the size of the error bars on each set of data. Only data-sets included in the PSA of [All93b] are presented, except for the very low-energy data of [Ber80] which are included in the re-analysis of [Geo03].

data, or as results on their own. Almost all of these are single-energy phase-shift analyses (PSA) of all the existing observables at that energy. The general trend, as would be expected, is that the more observables available to fit at a given energy, the better constrained the PSA solutions become. The existing single-energy PSAs that

have been performed have all suffered from this problem: multiple solutions from poor constraints provided by only one or two observables.

The advent of polarized ^{3}He technology [Col63] has allowed measurements of other spin-polarization observables such as the ^{3}He analyzing power A_{0y} and spin-correlation coefficients (i.e. A_{yy}, A_{zz}, A_{zx}, etc.) to be made. Later PSAs, of course, improved with the additional data to constrain the fits [McS69, Sza78b]. These observables are very hard to measure, however. No spin correlation measurements have been made below $E_{\rm p} = 5.54$ MeV, apart from a single A_{yy} measurement at 4.01 MeV [All93b].

The high-quality spin-correlation coefficient measurements made possible by the polarized target technology added significant new constraints to the p-^{3}He database making a new phase-shift analysis feasible. In [All93a], Alley *et al.* [All93b] performed an energy-dependent effective-range expansion phase-shift analysis, including most data sets measured before 1993. Each phase-shift is expressed as a power series in k^2 where k is the wave number. In all, 1085 total data points are included in the analysis between 1.0 - 12.0 MeV. With the constraints imposed by the added higher-order spin observables and the requirement that the phase-shifts be smoothly varying functions of energy, a unique phase-shift solution was found. The fit described the data with a χ^2 per degree of freedom (χ^2_ν) of 0.966. However, the very low energy data of Berg *et al.* were excluded from the data used in the fit, with no discussion as to why this choice was made. Consequences of this exclusion with respect to scattering length determinations will be discussed in Section 1.2.4.

1.2.3 Previous Work – Theory

Because of recent advances in computing power and computational techniques for solving the Schrödinger equation, predictions using realistic $NN + 3N$ potentials of observables in proton-^{3}He elastic scattering have become available. One of the interesting goals of these calculations is to determine whether there is an under-prediction of A_y, similar to that found in Nd scattering. The Pisa group has led the charge in this system by publishing predictions for the p-^{3}He singlet and triplet scattering

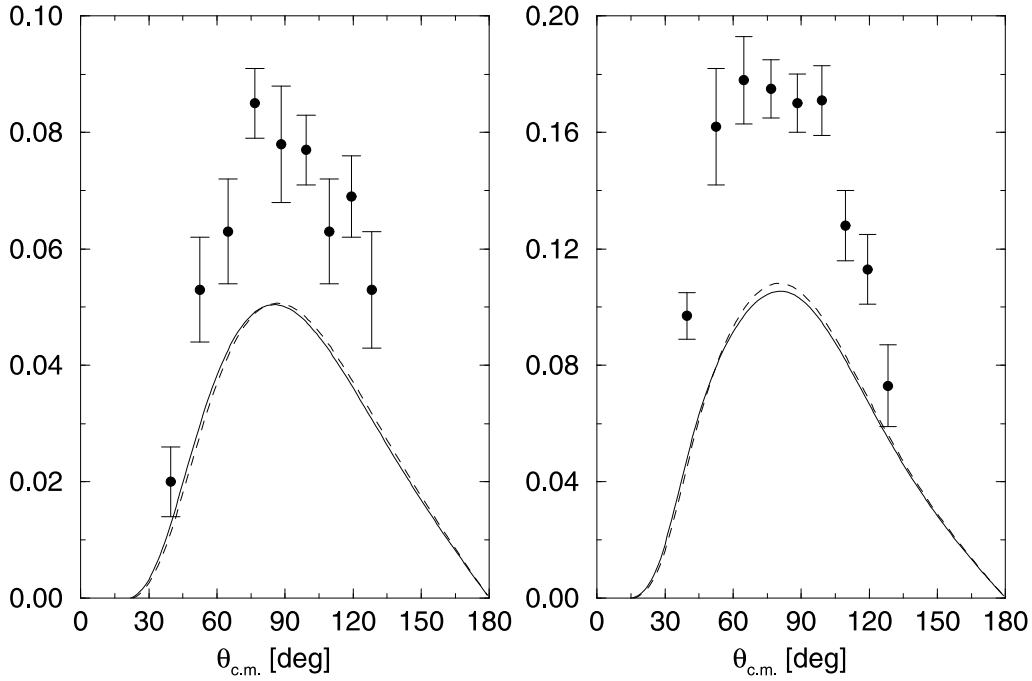

Figure 1.4: A_y results of [Viv01]. The plot on the left is for $E_{\rm p}$= 1.6 MeV, and $E_{\rm p}$= 2.25 MeV is on the right. The solid line indicates the calculation with the AV18 NN interaction and the dashed line the calculation with the Urbana IX $3N$ interaction added.

lengths in 1998 [Viv98] and their first calculations of the cross section $\sigma(\theta)$ and proton analyzing power A_y in 2001 [Viv01].

In [Viv01] the first evidence for the "A_y puzzle" in the proton-^{3}He system was presented. Calculations of $\sigma(\theta)$ and A_y were performed at $E_{\rm p}$= 1.6 and 2.25 MeV using the AV18 NN interaction only, and with the Urbana IX $3N$ force, are shown in Figure 1.4. New data taken at Wisconsin at those two energies are also shown. As can be seen, the calculations under-predict A_y by $\approx$ 40%. The addition of the three-nucleon interaction has little effect on the prediction for A_y. The error bars on these data are rather large and the scatter does not lend itself to a good quantitative comparison between theoretical predictions and data.

Similarly, a recent resonating group model (RGM) calculation by Pfitzinger *et al.* [Pfi01], which includes an updated R-matrix calculation of the available $T = 1$ data in the $A = 4$ system, also shows an under-prediction of A_y at $E_{\rm p} = 4.1$ MeV, where the data are of higher quality. Similar to [Viv01], it was found that the addition of

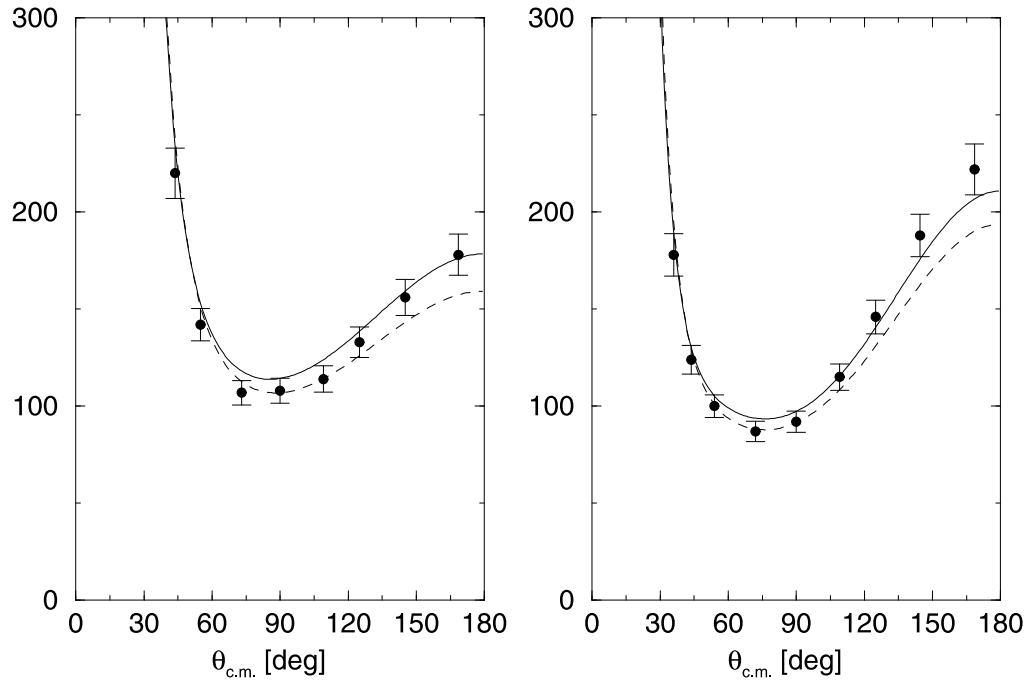

Figure 1.5: $\sigma(\theta)$ results of [Viv01]. The plot on the left is for $E_{\rm p}$= 1.6 MeV, and $E_{\rm p}$= 2.25 MeV is on the right. The data is that of [Fam54]. The solid line indicates the calculation with the AV18 NN interaction and the dashed line the calculation with the Urbana IX $3N$ interaction added.

three-nucleon force models to the calculation had nearly no effect on the predictions for A_y. Also, in [Rei03], similar RGM calculations show disagreements with the data. At $E_{\rm c.m.} = 5.20$ and 22.5 MeV, these theoretical calculations are all below the A_y data.

In each of [Viv01], [Pfi01], and [Rei03], P-waves play a very important part in predicting A_y. All of these theoretical calculations under-predict most of the P-waves with respect to the PSA of [All93b] or the R-matrix analysis in [Pfi01], and it was found that very small changes ($\approx$ 10%), particularly in the $^3P_2$ phase-shift, can change A_y significantly. In [Rei03] the effects of varying $\delta(^3P_2)$ were investigated. In [Viv01], A_y was found to be particularly sensitive to the combination $\Delta = \frac{1}{2}\left[\delta(^3P_1) + \delta(^3P_2)\right] - \delta(^3P_0)]$. Changes in one one of the three ^3P_j phase shifts can be balanced out by changes in another. This is very similar to the situation in the Nd case [Kie96].

A tantalizing potential discrepancy also exists in the differential cross section at these energies. As shown in Figure 1.5, the theoretical predictions of [Viv01] generally

agree with the data of [Fam54]. The addition of the $3N$ interaction improves this agreement at the minimum of the $\sigma(\theta)$ distribution. At backward angles, the AV18 + UR(IX) prediction moves away from the data. This discrepancy, again, is only suggested because the error bars on the data are large. More precise data are needed to make a truly meaningful comparison. In [Rei03], a similar discrepancy at backward angles was seen in the $\sigma(\theta)$ data at $E_{\text{c.m.}} = 5.20$ of [McD64]. An increase of 10.5° (a change of $\approx 20\%$ from theory) in $\delta(^3P_2)$ greatly improves the description of the differential cross section.

1.2.4 Scattering Lengths

There have been several attempts to theoretically calculate the singlet scattering length a_s and triplet scattering length a_t in proton-^{3}He elastic scattering. There is significant scatter in these predictions. Viviani *et al.* [Viv98] used the realistic AV18 NN potential and the Urbana IX $3N$ interaction in the correlated hyperspherical harmonic basis and the Kohn variational technique to predict values for the scattering lengths. Filikhin *et al.* [Fil00], however, solved the Fadeev-Yakubovsky equations using a cluster-reduction method (CRM). They employed the older Malfliet-Tjon I-III NN potential, and then parameterized their results with an eighth-order polynomial in scattering energy to extrapolate to zero-energy. Carlson *et al.* used a variational Monte-Carlo (VMC) technique including the older AV14 NN and Urbana VII $3N$ interactions. As can be seen in the upper half of Table 1.2, the current theoretical determinations of a_s and a_t for p-^{3}He zero-energy scattering do not agree with each other.

Experimentally, the situation is not much better. Typically, these values are determined by an extrapolating to zero energy an effective-range expansion of the nuclear phase-shifts determined from fitting to the existing data. Using the data of [Tom62] and [Ber80], Tegnér and Bargholtz obtained a value for a_t of 10.2 ± 1.4 fm [Teg83]. Alley and Knutson used a modified effective-range technique and a much larger database to determine the phase-shifts as a function of energy [All93b]. Using this analysis, val-

ues of $a_s = 10.8 \pm 2.6$ fm and $a_t = 8.1 \pm 0.5$ fm were obtained [Viv98, Car01].

With the addition of the newer A_y data of [Viv01], a re-analysis of the effective-range phase shift analysis of [All93b] was performed by George and Knutson [Geo03]. The addition of the data of [Viv01] had a negligible effect on the PSA, decreasing the χ^2_ν from 0.919 to 0.917. However the addition of the very low energy data of Berg *et al.* [Ber80] changes the phase-shift fits significantly from those of [All93b]. Two solutions were found that minimize χ^2, giving vastly different scattering length determinations. It was discovered that the very low energy $\sigma(\theta)$ data are responsible for the two minima in the χ^2 surface. This analysis shows that the scattering lengths for proton-^{3}He zero-energy scattering are currently not well determined experimentally. The current experimental determinations of a_s and a_t are summarized in the bottom half of Table 1.2. More high-precision data below 4 MeV is needed in order to obtain reliable phase-shifts and therefore a more precise determination of a_s and a_t.

These scattering length determinations also have an application to the astrophysically significant $p + {}^3\mathrm{He} \rightarrow {}^4\mathrm{He} + \nu_\mathrm{e} + \mathrm{e}^+$ reaction (abbreviated as the *hep* reaction). This reaction produces the highest energy neutrinos from the Sun, with an endpoint energy of 18.8 MeV. This process has recently received considerable attention [Mar00a] because of the observation of an excess over the Standard Solar Model (SSM) [Bah98] prediction of high-energy neutrinos in the Super-Kamiokande neutrino experiment in Japan [Fuk99]. While over most of the Super-K energy spectrum, a constant suppression of about 0.5 is observed relative to the SSM (the standard "Solar Neutrino Problem"), above 12.5 MeV there is an apparent excess of events, as shown in Figure 1.6.

In the SSM, the *hep* reaction is the only source of solar neutrinos with energy higher than 14 MeV. This fact has led to questions about the reliability of the calculations of the *hep* reaction cross section, upon which the SSM bases its currently accepted value for the astrophysical S-factor, 2.3×10^{-20} keV b [Sch92]. This is a rate far too small to measure in the laboratory. Figure 1.6 also shows how changes in the *hep* rate affect the description of the Super-K spectrum. As can be seen, increasing the *hep* rate by a factor of about 17 reproduces the Super-K neutrino energy spectrum.

Table 1.2: Experimental and theoretical values for the singlet a_s and triplet a_t scattering lengths for p-^{3}He elastic scattering.

Theoretical Predictions			
a_s [fm]	a_t [fm]	Method & Potential	Reference
11.5	9.13	CHH – AV18 + UR(IX)	[Viv98]
8.2	7.7	CRM – MTI-III	[Fil00]
	10.1 ± 0.5	VMC – AV14 + UR(VII)	[Car91]

Experimental Determinations			
a_s [fm]	a_t [fm]	Data Set	Reference
	10.2 ± 1.4	[Tom65], [Ber80]	[Teg83]
10.8 ± 2.6	8.1 ± 0.5	[All93b][a]	[All93b]
15.1 ± 0.8	7.9 ± 0.2	[All93b][a] + [Viv01] + [Ber80], solution 1	[Geo03]
7.2 ± 0.8	10.4 ± 0.4	[All93b][a] + [Viv01] + [Ber80], solution 2	[Geo03]

[a] Dataset in [All93b] includes 1085 data points from 1993 and earlier. References to specific data sets are found therein.

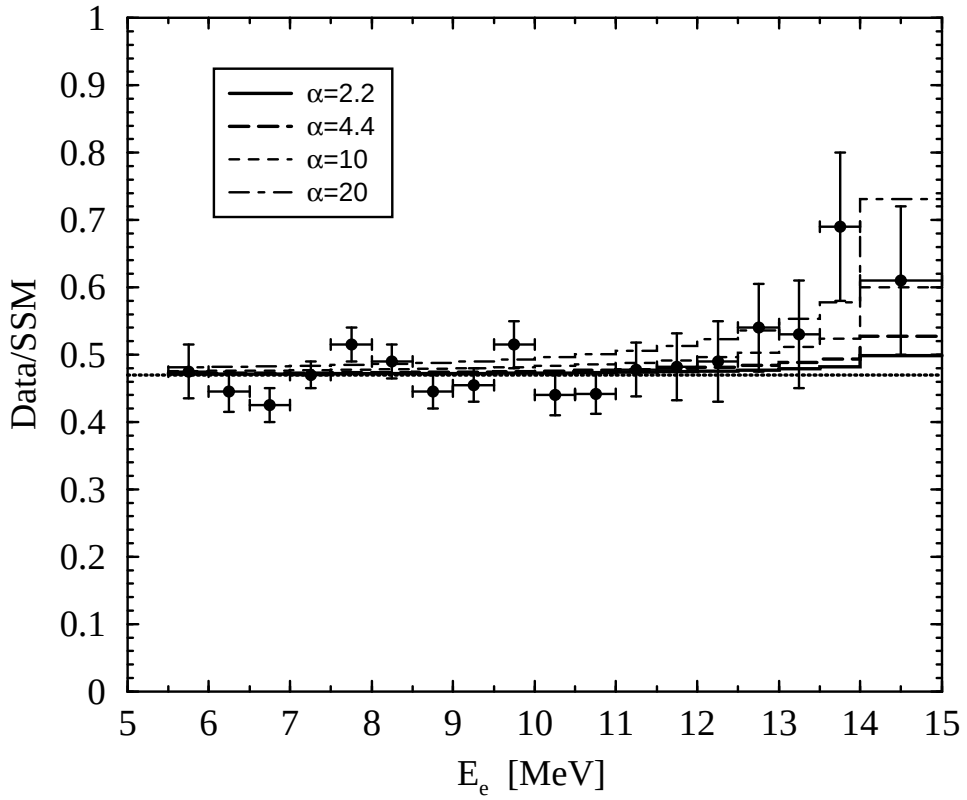

Figure 1.6: Ratio of the neutrino energy spectrum to that predicted by the standard solar model, assuming no neutrino oscillations [Fuk99]. An excess above the SSM prediction is shown at the highest energy bins. The *hep* rate has been varied in an attempt to reproduce this high energy discrepancy. The 5 curves correspond respectively to no *hep* enhancement α (dotted line), and an enhancement by a factor of 2.2 (solid line), 4.4 (long-dashed line), 10 (dashed line) and 20 (dot-dashed line). Taken from [Mar00c].

In a "Fermi's Golden Rule" picture, the transition amplitude between the initial proton + ^{3}He wavefunction and the final ^{4}He wavefunction is given by [Mar00a]

$$\langle f|H_W|i\rangle \propto \frac{G_V}{\sqrt{2}}\langle -\boldsymbol{q}; {}^4\mathrm{He}|j_\sigma^\dagger(\boldsymbol{q})|\boldsymbol{p}; \mathrm{p}{}^3\mathrm{He}\rangle \ , \tag{1.1}$$

where G_V is the Fermi constant, and $\mathbf{q}$ is the sum of the positron and neutrino momentum. The $|\boldsymbol{p}; \mathrm{p}{}^3\mathrm{He}\rangle$ and $|-\boldsymbol{q}; {}^4\mathrm{He}\rangle$ represent, respectively, the p+^{3}He scattering state wavefunction with relative momentum $\boldsymbol{p}$ and the ^{4}He bound state wavefunction recoiling with momentum $-\boldsymbol{q}$. Here, $j_\sigma(\boldsymbol{q})$ is the nuclear weak current. As can be seen, calculations of its rate require accurate proton + ^{3}He wavefunctions near zero-energy.

Recent calculations by Marcucci *et al.* [Mar00a, Mar00b] increase the *hep* rate by a factor of 5, but are limited because of the poor accuracy of the scattering length predictions. A high-precision database of low-energy proton-^{3}He elastic scattering data is needed in order to perform the phase-shift analysis needed to determine a_s and particularly a_t, the scattering length of importance in determining the *hep* rate.

1.3 Experiments

Seeking a solution to all these problems, a series of measurements of proton-^{3}He elastic scattering measurements have been performed. Angular distributions of the differential cross section $\sigma(\theta)$ and proton analyzing power A_y have been measured at several energies below 5 MeV. The nominal proton energy E_p at which each experiment was performed is listed in Table 1.3. These energies were chosen to maximize the improvement in the low energy database, and because theoretical calculations can be performed in this region. The analyzing power experiments were performed with a gas-cell target and the $\sigma(\theta)$ measurements were performed using a supersonic gas-jet target which was installed, refurbished, and improved for this work.

Details of these experiments are described in subsequent chapters. Chapter 2 discusses briefly modern realistic potential models and the methods used to calculate observables in the $A = 4$ system. A description of the jet-target and its operational parameters is given in Chapter 3; the description of the experiments is given in Chapter

Table 1.3: List of observables measured at each energy in this work.

E_p [MeV]	Observables
1.00	$\sigma(\theta)$
1.60	$\sigma(\theta)$ A_y
2.25	$\sigma(\theta)$ A_y
3.13	$\sigma(\theta)$ A_y
4.05	$\sigma(\theta)$ A_y

4; the analysis of the data is presented in Chapter 5; and conclusions drawn along with future directions for research are in presented in Chapters 6 and 7.

Chapter 2

Theory

Only recently, with the continuous march of Moore's Law in increasing computing power, have realistic *ab initio* calculations of proton-^{3}He elastic scattering become possible. The theoretical underpinnings of such calculations are too involved for an in-depth discussion here. However, in this chapter, a brief description of the realistic potential models used in these calculations, and the computational methods themselves are discussed.

2.1 Realistic Potential Models

Within the realm of non-relativistic quantum mechanics, making predictions of observables requires solving the Schrödinger equation for different potentials. Modern NN potentials are constructed phenomenologically by fitting a functional form of the potential to the global NN database. Different potentials, of course, use different functional forms either in momentum or configuration space. This potential is then inserted into the Hamiltonian and then the Schrödinger equation is solved by any means necessary.

Several potentials have been developed since the late 1970's when such efforts began: the Paris potentials [Lac80, Pig94], the charge-dependent Bonn (CD-Bonn) potentials [Mac87, Jia92, Mac01], the Nijmegen potentials [Sto94], and and the Argonne potentials, of which the v_{18} potential (AV18) is the latest [Wir95].

With each generation, great efforts have been made to improve the description of the nucleon-nucleon interaction. The two most popular potentials — CD-Bonn and AV18 — include explicitly both charge independence and charge symmetry breaking (CIB, CSB) terms. These two potentials are quite different in their functional form, most obviously because CD-Bonn is written in momentum-space whereas AV18 is in configuration space. However, they both describe the NN scattering data (pp, np, and nn) below $E_{lab} = 300$ MeV with a nearly perfect χ^2/datum ≈ 1.

Both of these potentials can be written down in the general form

$$v(NN) = v^{EM}(NN) + v^{\pi}(NN) + v^{R}(NN), \tag{2.1}$$

in which the potential is expanded as a sum of an electromagnetic part $v^{EM}(NN)$, a long range one-pion-exchange (OPEP) part $v^{\pi}(NN)$, and a phenomenological short range part $v^{R}(NN)$. In both AV18 and CD-Bonn, $v^{R}(NN)$ contains an operator structure [Gre96] with about 40 free parameters which are determined by fitting to the NN scattering data and the deuteron binding energy (BE).

The AV18 potential contains an extensive $v^{EM}(NN)$ part, taking into account both the fundamental Coulomb interaction between two point protons, and several higher order contributions such as one- and two-photon Coulomb terms, the Darwin-Foldy term, vacuum polarization and magnetic moment interactions. The finite size of the nucleon charge distributions is also included. It takes into account differences between proton-proton and neutron-proton interactions by including a Coulomb term for the neutron charge distribution and its magnetic moment interaction, but in the nn case the magnetic moment interaction only. An in-depth discussion of the AV18 potential is given in [Wir95]. In contrast, the electromagnetic terms in CD-Bonn are much simpler: $v^{EM}(pp)$ is the Coulomb force between two point protons and any EM interaction in the neutron-proton and neutron-neutron case is ignored ($v^{EM}(np) = v^{EM}(nn) = 0$).

These potentials are fit to the culled NN database of the Nijmegen group, used in their global NN phase-shift analysis (PSA) [Sto93]. This database includes about 4300 data from NN experiments below $E_{\rm lab} = 500$ MeV. Observables include cross-section and polarization data from elastic scattering, along with the experimental values for

Table 2.1: $3N$ binding energies from [Nog02] for both CD-Bonn 2000 and AV18 with and without three-nucleon forces included, compared to the experimental values. All results are given in MeV.

Potential Model	^{3}H	^{3}He
CD-Bonn 2000	8.005	7.274
CD-Bonn 2000 + TM	8.482	7.732
AV18	7.624	6.925
AV18 + UR(IX)	8.479	7.750
Experiment [Aud93]	8.482	7.718

the binding energy, the magnetic moment, and quadrupole moment of the deuteron, and determinations of the proton-proton, neutron-proton, and neutron-neutron scattering lengths. Not all of the experimental data in the literature are included by the Nijmegen group. Data are excluded from their database if they lie a certain number of standard deviations away from the PSA fits [Ber90]. This exclusion, of course, improves the χ^2 of the final PSA fit.

2.2 Three-Nucleon Interactions

When these realistic potential models are used to predict the simplest observable in the three-nucleon system, they fail; the binding energies for both ^{3}H and ^{3}He are under-predicted by about 1 MeV. This is found no matter which modern NN potential or computational method used [Nog00, Nog02, Nog03]. The most recent benchmark calculation of Nogga *et al.* shows this under-prediction for both the CD-Bonn and AV18 interactions. Their results are reproduced in Table 2.1.

Given the universality of this under-binding, it appears to be impossible to describe nuclear systems with $A > 2$ without adding a three-nucleon interaction (TNI) into the nuclear Hamiltonian. Several TNI models have been studied in the literature mostly based on the exchange of two pions with an intermediate Δ excitation, as shown in

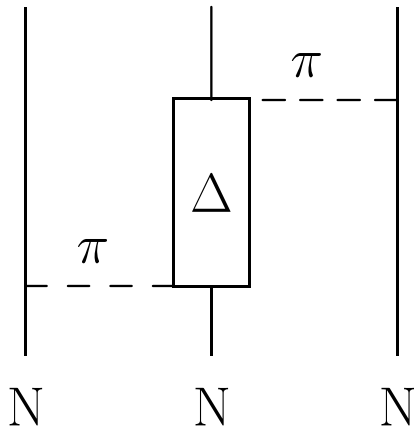

Figure 2.1: The Fujita-Miyazawa three-nucleon force model: two-pion-exchange with the Delta-isobar excitation in the intermediate state.

Figure 2.1. These interactions include a certain number of parameters not completely determined by theory, therefore some of them can be varied to reproduce the ^{3}H and ^{3}He binding energies. Examples of TNIs include the Tuscon-Melbourne (TM) interactions [Coo79] and the version TM$'$ corrected for chiral-symmetries [Fri99], the Brazil (BR) interaction [Coe83], and the Urbana (UR) series of interactions [Car83, Pud95]. For a recent review see [Car98].

When these realistic models (including the TNIs) are used to predict the simplest observable in the *four*-nucleon system — the ^{4}He binding energy — they do quite well. A summary of recent results of calculations of α-particle binding energies from several different groups is given in Table 2.2. As can be seen, NN interactions alone under-bind the α-particle by ≈ 2 MeV, but there is good agreement when $3N$-forces (UR(XII), UR(IX) and TM$'$) are included. This is good evidence that any sort of *four*-nucleon interactions in the $A = 4$ system are quite small, and can be neglected.

These $NN + 3N$ models do quite well in predicting $3N$ observables, apart from the Nd analyzing power as described in Section 1.1. It is hoped that using these interactions, *ab initio* calculations of few-nucleon processes and even nuclear structure of higher mass nuclei can be performed with high-accuracy [Wir00, Wir02, Bar02].

Table 2.2: α-particle binding energy E_α predictions from several NN and $3N$ potential models compared with the experimental value. Since there is little discrepancy between experiment and predictions made with $NN+3N$ models, *four*-nucleon effects are thought to be small.

Interaction	E_α [MeV]	Ref.
AV14	24.02	[Viv95]
AV14 + UR(XII)	27.85	[Viv95]
AV18	24.25	[Nog02]
AV18 + UR(IX)	28.50	[Nog02]
AV18 + UR(IX)	28.34	[Wir00]
CD-Bonn	26.26	[Nog02]
CD-Bonn + TM'	28.50	[Nog02]
Experiment	28.30	[Aud93]

2.3 Methods for $A = 4$ Calculations

To calculate predictions for observables in proton-^{3}He elastic scattering, a solution to the Schrödinger equation is needed. As any student of physics knows, this can be quite difficult for anything but the simplest potentials. Expansion methods have been developed which can obtain arbitrary accuracy for a solution, given enough computing power. The two predominant methods currently being used in the $A = 4$ system are the Faddeev-Yakubovsky (FY) method [Yak69] and the correlated hyperspherical harmonics (CHH) method using a variational approach [Viv95, Kie93, Kie97].

The two sets of Jacobi coordinates for calculations in both methods are shown graphically in Figure 2.2, and are defined as

$$\begin{array}{ll} \text{Set A } (3+1) & \text{Set B } (2+2) \\ \hline \boldsymbol{x}_{1p} = \sqrt{\frac{3}{2}}\left(\boldsymbol{r}_m - \frac{\boldsymbol{r}_i+\boldsymbol{r}_j+\boldsymbol{r}_k}{3}\right) & \boldsymbol{y}_{1p} = \boldsymbol{r}_m - \boldsymbol{r}_k \\ \boldsymbol{x}_{2p} = \sqrt{\frac{4}{3}}\left(\boldsymbol{r}_k - \frac{\boldsymbol{r}_i+\boldsymbol{r}_j}{2}\right) & \boldsymbol{y}_{2p} = \sqrt{2}\left(\frac{\boldsymbol{r}_m+\boldsymbol{r}_k}{2} - \frac{\boldsymbol{r}_i+\boldsymbol{r}_j}{2}\right) \\ \boldsymbol{x}_{3p} = \boldsymbol{r}_j - \boldsymbol{r}_i & \boldsymbol{y}_{3p} = \boldsymbol{r}_j - \boldsymbol{r}_i. \end{array} \tag{2.2}$$

The wavefunction for the four-nucleon system with total angular momentum J, total isospin T, and their respective conserved projections J_z and T_z, can be written

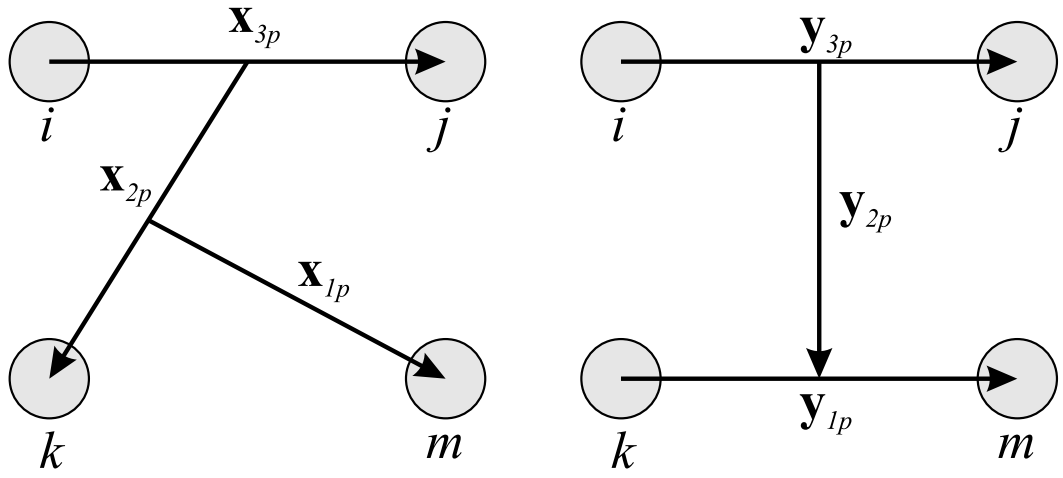

(a) Set A (b) Set B

Figure 2.2: The two sets of Jacobi coordinates used in 4-nucleon calculations. Set A represents a $3+1$ configuration while Set B represents a $2+2$ configuration.

as a sum of amplitudes

$$\Psi = \sum_{p=1}^{12} \left[\psi_A(\boldsymbol{x}_{1p}, \boldsymbol{x}_{2p}, \boldsymbol{x}_{3p}) + \psi_B(\boldsymbol{y}_{1p}, \boldsymbol{y}_{2p}, \boldsymbol{y}_{3p}) \right], \tag{2.3}$$

where p represents an even permutation of the particles. ψ_A and ψ_B can each be further decomposed into radial, angular, and spin/isospin parts, of which all but the radial parts are well known. Either basis ψ_A or ψ_B is complete if enough (J, J_z, T, T_z) channels are included. However, expansions in both configurations are often used, allowing for quicker convergence.

In the FY method, these amplitudes are inserted into the Schrödinger equation and then converted into a series of equations for each amplitude in the sum in Equation 2.3. Using symmetry arguments, the number of equations can be reduced to two coupled integro-differential equations. These are then solved using an expansion method and a tremendous amount of computer power. A more technical description is given by Nogga *et al.* [Nog02], and references therein. Incorporating long-range interactions such as the Coulomb force (which becomes important in scattering states with charged particles) is very problematic for the Faddeev-Yakubovsky method, and therefore this method has only been used for calculations of bound states [Nog02] and for scattering

states with a neutron in the incoming channel. However, some progress incorporating the Coulomb interaction in the FY method has been made. For instance, Filikhin and Yakolev [Fil00] have performed calculations in a "cluster-reduction method" of proton-^{3}He elastic scattering, making predictions of the scattering lengths, as shown in Table 1.2 in Chapter 1. A good summary of Faddeev techniques in few-nucleon physics is in [Car98] and a much more pedagogical description in [Glö83].

The correlated hyperspherical harmonic (CCH) method has been developed by the Pisa Group and does not suffer from the problems of the FY method when the Coulomb interaction is included. It becomes ideal for calculating scattering states with charged particles. The calculations shown in Chapter 6 were performed using this method [Viv02, Viv03]. Each of the amplitudes in Equation 2.3 again is expanded into angular momentum and isospin channels (labeled α),

$$\psi_A(\boldsymbol{x}_{1p}, \boldsymbol{x}_{2p}, \boldsymbol{x}_{3p}) = \sum_\alpha F_{\alpha p} \Phi_{A\alpha}(x_{1p}, x_{2p}, x_{3p}) \mathcal{Y}^A_{\alpha p} \tag{2.4}$$

$$\psi_B(\boldsymbol{y}_{1p}, \boldsymbol{y}_{2p}, \boldsymbol{y}_{3p}) = \sum_\alpha F_{\alpha p} \Phi_{B\alpha}(y_{1p}, y_{2p}, y_{3p}) \mathcal{Y}^B_{\alpha p}. \tag{2.5}$$

The $\mathcal{Y}$'s contain all the spin, isospin, and angular dependence of the wavefunction, and the radial spatial part remains in the Φ's. The F functions are the correlation functions which take into account the strong state-dependent correlations induced by the NN interaction. They improve the behavior of the wavefunctions at small inter-nucleon separations [Kie94]. The explicit form of the expansion is given in [Viv95, Car98].

Using hyperspherical coordinates, the hyperradius is defined as

$$\rho = \sqrt{(x_{1p})^2 + (x_{2p})^2 + (x_{3p})^2} = \sqrt{(y_{1p})^2 + (y_{2p})^2 + (y_{3p})^2} \tag{2.6}$$

and the hyperangles are defined as

$$\cos\phi_{3p} = x_{3p}/\rho = y_{3p}/\rho, \tag{2.7}$$

$$\cos\phi^A_{2p} = x_{2p}/(\rho \sin\phi_{3p}), \tag{2.8}$$

$$\cos\phi^B_{2p} = y_{2p}/(\rho \sin\phi_{3p}). \tag{2.9}$$

The spatial parts of the two amplitudes can be expanded in terms of the hyperspherical

harmonics (HH)

$$\Phi_{A\alpha}(x_{1p}, x_{2p}, x_{3p}) = \sum_{n,m} \frac{u^{\alpha}_{nm}(\rho)}{\rho^4} x_{1p}^{l_{1\alpha}} x_{2p}^{l_{2\alpha}} x_{3p}^{l_{3\alpha}} Y^{\alpha}_{nm}(\phi^A_{2p}, \phi_{3p}), \tag{2.10}$$

$$\Phi_{B\alpha}(y_{1p}, y_{2p}, y_{3p}) = \sum_{n,m} \frac{w^{\alpha}_{nm}(\rho)}{\rho^4} y_{1p}^{l_{1\alpha}} y_{2p}^{l_{2\alpha}} y_{3p}^{l_{3\alpha}} Y^{\alpha}_{nm}(\phi^B_{2p}, \phi_{3p}), \tag{2.11}$$

with

$$Y^{\alpha}_{nm}(\beta, \gamma) = N^{\alpha}_{nm} (\sin\gamma)^m P_n^{K_{2\alpha}, l_{3\alpha}+\frac{1}{2}}(\cos 2\gamma) P_m^{l_{1\alpha}+\frac{1}{2}, l_{2\alpha}+\frac{1}{2}}(\cos 2\beta); \tag{2.12}$$

The P's are the Jacobi polynomials, N^{α}_{nm} are normalization factors, n and m are integers that range from zero to infinity, and $K_{2\alpha} = l_{1\alpha} + l_{2\alpha} + 2(m+n)$.

Solving these equations involves determining the form of the hyper-radial functions $u^{\alpha}_{nm}(\rho)$ and $w^{\alpha}_{nm}(\rho)$, which is done using the Raleigh-Ritz variational principle. This procedure is described in detail in [Viv95]. When applied to scattering states, a similar expansion is done with the addition of an asymptotic part of the scattering wavefunction [Viv01]. This asymptotic part is solved using the complex form of the Kohn variational principle [Kie97, Kie94]. For a further description of this method, see [Viv01] and references therein.

Other methods currently being employed in the literature are the Alt-Grassberger-Sandhas (AGS) equations [Alt70], which are related to the Faddeev family of techniques and the Resonating-Group Model (RGM) which is also a variational technique using a Gaussian expansion. Pedagogical descriptions of both can be found in [Fer87].

Chapter 3

Gas Jet Target

Much of the time and labor spent in this research endeavor was involved in refurbishing, installing, and improving the TUNL Gas-jet Target. This chapter discusses why such a target is useful, how it works, and its operational parameters.

3.1 Targetry in Nuclear Physics Experiments

The choice of target in an accelerator-based nuclear physics experiment is, of course, a dependent on what is intended to be measured. Different targets are useful for different kinds of experiments.

For the series of measurements made for this work, the ideal target would have several properties, directly related to obtaining high quality angular distribution data. This ideal target would be one that (obviously) has sufficient amount of the desired isotope so to give a reasonable count rate with the available beam current. It should be safe to manufacture and use. It would also have minimal contamination from other elements that may interfere with peaks of interest. The target should not degrade over time (or at least degrade very slowly) while being bombarded with the beam. The reaction kinematics should be well determined. Our ideal target would cause minimal energy broadening of the incident beam while traversing the target. Similarly, the exiting products from the reaction should experience a minimum of energy and angle

straggling. These effects are often particularly important at low incident beam energies where they hinder the determination of the exact reaction energy and yield. With an ideal target, minimal broadening of peaks in the outgoing particle energy spectra would take place.

If such a target existed, angular distribution measurements would be, as they say, "a piece of cake." Of course, such an ideal target does not exist in the laboratory, so such culinary aphorisms are not appropriate. Approximations to this ideal target can be made with different trade-offs.

3.1.1 Solid Targets

For low energy elastic scattering experiments solid targets must be in the form of thin foils, allowing most of the beam to pass through the target without interacting. Thicker solid targets induce too much energy loss, or even cause the incident beam to stop completely. This would be acceptable for certain gamma-ray measurements, but is untenable for angular distribution measurements of elastic scattering with charged particle beams.

The solid targets our research group has developed are amorphous hydrogenated carbon foils, with carbon to hydrogen ratios of roughly 2 to 1. They are made using the plasma assisted chemical vapor deposition (PACVD) technique developed by Black [Bla95]. These targets have been found to be quite durable, and incident beams experience relatively small energy losses. The targets were used for extensive measurements of cross sections and analyzing powers of proton-deuteron scattering at $E_{\mathrm{c.m.}} = 432$ and 667 keV [Bru01, Woo02]. They are also being used at lower energies for investigations of the ^{2}H(d,p)^{3}H and ^{2}H(d,n)^{3}He reactions for deuteron energies $E_d = 150 - 680$ keV [Leo02].

However, despite these good qualities, background effects from the carbon present in these targets can often become a problem. As an example, a hydrogenated carbon target was bombarded with a ^{3}He beam at 6.73 MeV. A sample spectrum is shown in Figure 3.1. The reactions ^{12}C(^{3}He,p)^{14}N, ^{12}C(^{3}He,d)^{13}N, and ^{12}C(^{3}He,α)^{11}C produce

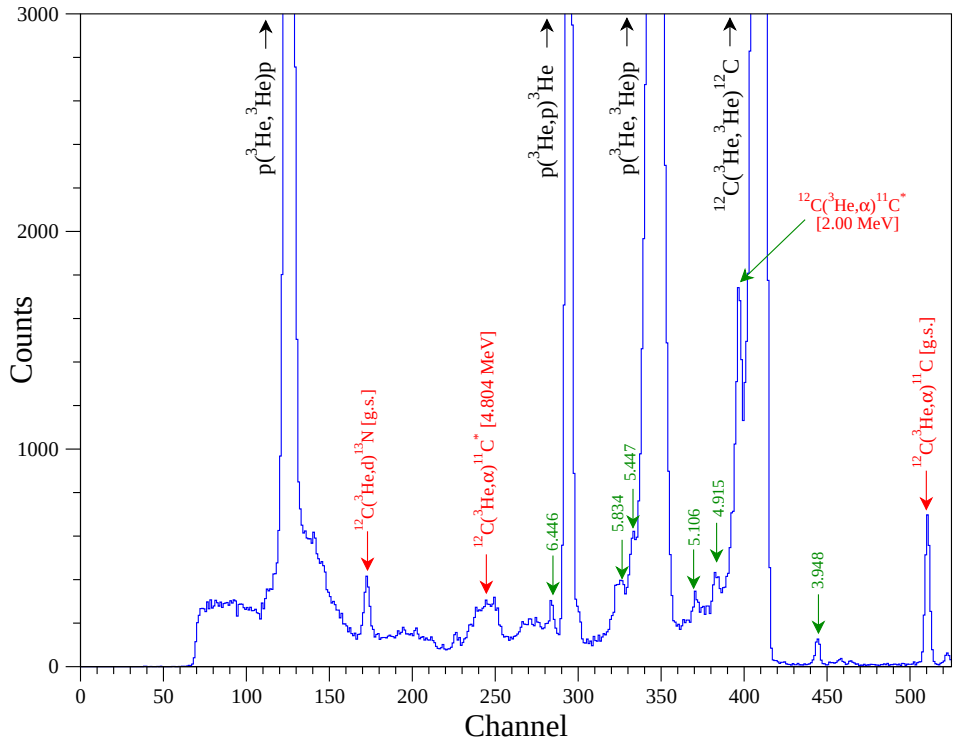

Figure 3.1: Zoomed typical spectrum of scattered particles from a 6.73 MeV ^{3}He beam on a solid hydrogenated carbon target. The detector was at 13°. Several of the prominent contaminant peaks from (^{3}He,p), (^{3}He,α), and (^{3}He,d) reactions on ^{12}C present in the target are marked. Those marked with small green arrows are some of the many ^{12}C(^{3}He,p)^{14}N* reactions. The number above the arrow indicates the excitation energy (in MeV) of the residual ^{14}N nucleus.

many of the background peaks seen. Especially because many channels are open in the ^{12}C(^{3}He,p)^{14}N reaction (corresponding to excitations in ^{14}N), the background under the peaks of interest become difficult to determine.

3.1.2 Gas Cell Targets

When the target of interest naturally occurs as a gas at room temperature, a static gas cell is often used as a target. Essentially a balloon, a volume of gas is kept isolated from the vacuum system by thin-foil walls. These foils are often made of nickel or Havar alloy[3]. Inert gases, such as helium, that are not easily incorporated

[3]Havar is an alloy of Co (42.5%), Cr (20%), Ni (13%), with the remainder being Fe, W, Mo, and Mn. Obtained from Goodfellow Corporation, `http://www.goodfellow.com/`.

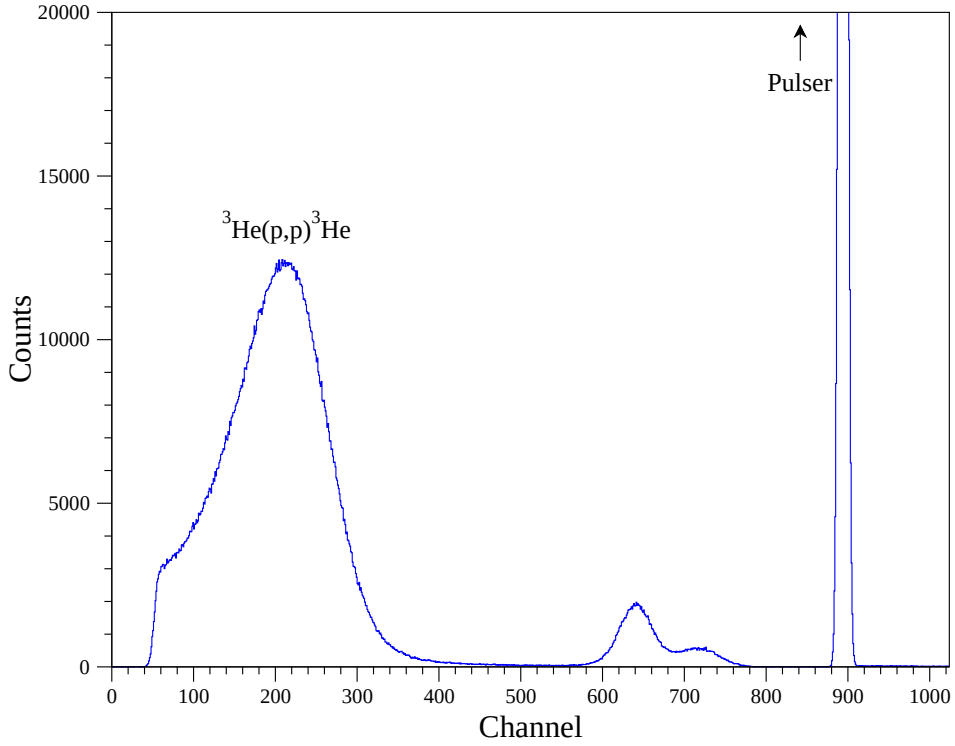

Figure 3.2: Typical spectrum of scattered particles from a 1.6 MeV proton beam (nominal energy at center of cell) on a ^{3}He-filled gas cell. The cell's walls are 2.54 μm thick Havar foil. The detector is at 90°. The two peaks at channels $600-800$ are from air contamination. The very broad peak shape is due to energy and angle straggling of the incident beam and exiting particles. Usable spectra were not obtainable for angles much greater than 90° because of the substantial energy losses.

into solid targets (except at extremely high pressures and low temperatures) can also be easily used as a target gas with a gas cell. Gas cells allow the use of a pure sample of target material (i.e. pure hydrogen gas, rather than a hydrocarbon, or the solid hydrogenated carbon foils in Section 3.1.1).

However, gas cells have their own problems. The incident beam heats the finite volume of target gas, causing the gas density, and therefore the target thickness, to fluctuate depending on the beam intensity. If performing $\sigma(\theta)$ measurements, this becomes a problem, though it is less of a factor in analyzing power measurements. Also, energy losses can be substantial, especially at low bombarding energies and in measurements at backward angles. The foils keeping the target gas inside the cell are often of a high-Z material, which have a large stopping-powers [Zie85]. At low energies,

particles scattered at backward angle do not have enough energy to make it out of the cell – a problem if a complete angular distribution is desired. An example scattered particle energy spectrum at $\theta_{\rm lab} = 90^\circ$ from a 1.6 MeV proton beam incident on a gas-cell filled with 1 atm of ^{3}He is shown in figure 3.2. Significant peak broadening comes from angular straggling of both the entering beam and scattered particles especially at this energy and angle. At very low energies, gas cells become essentially useless for angular distribution measurements of elastic scattering. In the case of proton-^{3}He elastic scattering, detecting particles at $\theta_{\rm lab} > 90^\circ$ becomes very difficult at proton energies below 1.5 MeV.

3.2 The Gas Jet Target

If we could combine the stability and good kinematic properties of solid thin-foil targets with the target purity offered by gas cells, we would have a very good approximation of our ideal target. A supersonic gas-jet target comes pretty close to attaining this ideal combination. In such a target, high pressure gas streams out of an appropriately shaped nozzle into the scattering chamber vacuum system producing a supersonic jet. The thermodynamic properties of the supersonic jet cause an area of high density to be formed below the nozzle with a target thickness that is comparable to that of a solid target. This region is used as the target. The gas is then pumped away by stages of differential pumping to maintain the high vacuum needed in accelerator systems.

The geometry of the scattering region is well defined since the area of high pressure is generally smaller than a typical gas cell. Because there are no cell windows, energy loss and straggling effects are greatly reduced. Target purity is also greatly improved over solid targets, since, for example, pure hydrogen gas can be used and the resulting backgrounds are carbon-free. The constant flow eliminates problems with beam related heating [Bec82].

All of these good qualities come at a technological price, of course. Such a target requires massive amounts of pumping to maintain the low pressures needed to have

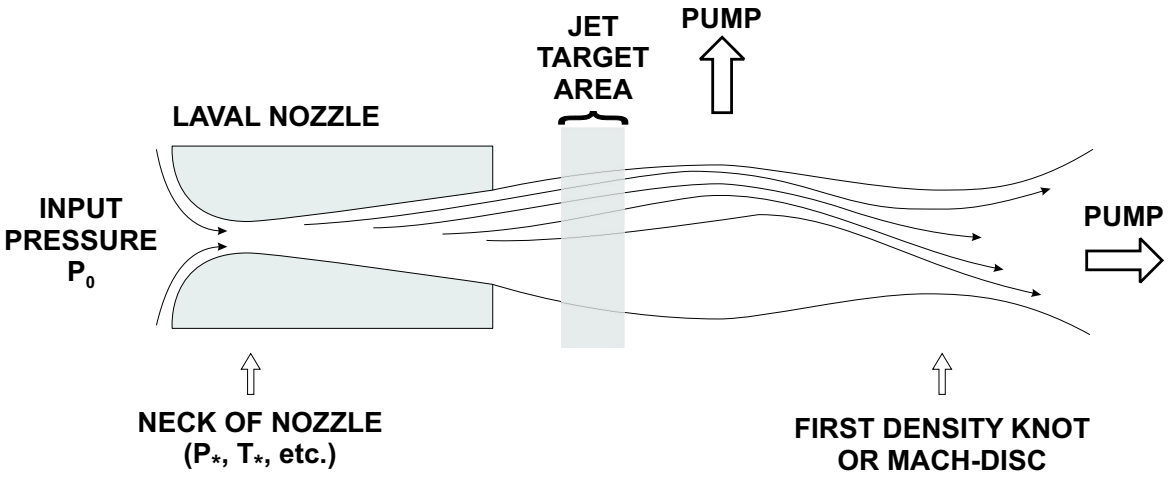

Figure 3.3: Schematic presentation of high pressure gas streaming out of the the gas-jet target Laval nozzle into a region of much lower pressure. The region chosen as the target zone is indicated. This figure is adapted from [Bec82].

the system mated to the accelerator system. Gas consumption is also a problem – gas jet targets are ravenous gas consumers.

3.2.1 Theory of the Gas Jet

As was stated above, the operational principle of the gas-jet target is the supersonic expansion of high pressure gas streaming out of an "appropriately shaped" nozzle into a region of significantly lower pressure. "Appropriately shaped" in this case means a converging-diverging, or Laval[4] nozzle, shown in Fig. 3.3.

A simple one-dimensional model can help illustrate the principle of the gas-jet target [Tho72, Bec82, Sha85]. We assume that an incompressible ideal gas undergoes isentropic, adiabatic expansion from rest in a reservoir with temperature T_0, pressure P_0, density ρ_0 and enthalpy h_0. For a "perfect" ideal gas [Tho72] the ratio of the specific heats γ is a constant,

$$\gamma = \frac{c_v}{c_p} = \text{constant}. \tag{3.1}$$

[4]Named for Swedish inventor Carl Gustav Patrik de Laval (1845-1913), who first developed the converging-diverging nozzle for use in driving a steam turbine for use in a centrifugal cream separator (1883) [Tho72]

The "perfect" condition also implies both c_v and c_p are also constants. From the adiabatic condition, the ratio of specific heats determines the speed of sound in the gas

$$c(T) = \sqrt{\gamma RT}, \tag{3.2}$$

where T is the temperature, and $R \equiv c_p - c_v$ is the universal gas constant.

For inviscid flow, when viscosity and any heat transfer in the gas can be neglected, the Bernoulli equation becomes

$$h + \frac{v^2}{2} = \text{constant}, \tag{3.3}$$

where h is the specific enthalpy of the gas, and v is the flow velocity. Integrating the definition

$$c_p \equiv \left(\frac{\partial h}{\partial T}\right)_P, \tag{3.4}$$

for a "perfect" gas, we obtain

$$h(T) = c_p T + \text{constant}. \tag{3.5}$$

The Bernoulli equation becomes,

$$c_p T + \frac{v^2}{2} = c_p T_0. \tag{3.6}$$

Using the useful identity $c_p = \gamma R/(\gamma - 1)$, and Equation 3.2 above, we get

$$c^2 + \frac{\gamma - 1}{2} v^2 = c_0^2. \tag{3.7}$$

If we divide both sides by c^2, we get

$$\frac{T_0}{T} = 1 + \frac{\gamma - 1}{2} M^2, \tag{3.8}$$

where $M \equiv v/c$ is the Mach number. This equation relates the temperature of the gas at a given velocity (or Mach number) at a point downstream of the nozzle to the temperature in the reservoir. This ratio of temperatures can be related to other thermodynamic variables through the adiabatic condition

$$\frac{T_0}{T} = \left(\frac{c_0}{c}\right)^2 = \left(\frac{P_0}{P}\right)^{(\gamma-1)/\gamma} = \left(\frac{\rho_0}{\rho}\right)^{\gamma-1}. \tag{3.9}$$

Table 3.1: Critical thermodynamic ratios for supersonic flow for gases with different γ's. Taken from [Tho72].

	$\gamma = c_v/c_p$		
Ratio	$9/7 = 1.286$	$7/5 = 1.400$	$5/3 = 1.667$
$\frac{T_*}{T_0}$	0.8750	0.8333	0.7500
$\frac{P_*}{P_0}$	0.5483	0.5283	0.4871
$\frac{\rho_*}{\rho_0}$	0.6267	0.6339	0.6495

When the flow speed v reaches the speed of sound c, $M = 1$. We use asterisks to denote this "critical" velocity when the flow velocity $v_* \equiv c$. Inserting $M = 1$ into Equation 3.8 and using the adiabatic conditions in Equation 3.9, we can determine the "critical ratios" which determine when the flow becomes supersonic,

$$\frac{T_*}{T_0} = \frac{2}{\gamma+1} \qquad \frac{P_*}{P_0} = \left(\frac{2}{\gamma+1}\right)^{\gamma/(\gamma-1)} \qquad \frac{\rho_*}{\rho_0} = \left(\frac{2}{\gamma+1}\right)^{1/(\gamma-1)} \tag{3.10}$$

Thus, when the ratio P/P_0 becomes smaller than the critical ratio, the gas flow through the Laval nozzle with be supersonic. Table 3.1 lists numeric values for these critical ratios for gases of several ratios of specific heats. Only when the jet becomes supersonic does this "self-focusing" effect shown in in Figure 3.3 occur. An example density plot of the jet expanding out of a typical Laval nozzle, as calculated by a much more complicated numerical model, is shown in Figure 3.2.1. Modeling of the jet region beyond the very simple model above is beyond the scope of this work.

3.2.2 History

The gas-jet target in use at TUNL was originally designed and built by researchers at the University of Erlangen-Nürenberg in Erlangen, Germany in the mid 1970's [Bit79b, Bit79c]. It was primarily used for measuring proton-proton analyzing powers at low energies at Erlangen [Bit79a] and then later at ETH-Zurich and the Paul Scherrer Institute (PSI) in Switzerland [Bit87]. It has also been used for polarized $(\vec{\mathrm{d}}, \mathrm{p})$ and $(\vec{\mathrm{d}}, \mathrm{d})$ reactions on ^{14}N, with the intent of deducing J^π values and spectroscopic

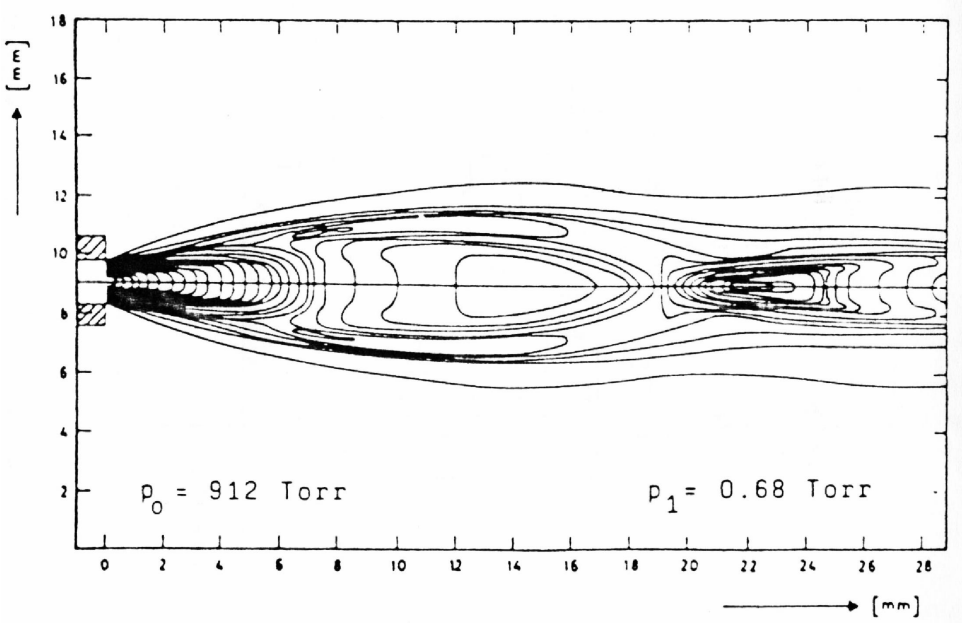

Figure 3.4: An example jet-density profile from [Wei89] for a given expansion ratio P_0/P_1.

factors for low lying states in ^{15}N [Kre80b]. At the time, it produced targets with some of the highest densities reported for such a device.

The target consists of a scattering chamber as well as the necessary apparatus to pump away the target gas. Thicknesses reportedly achieved with this system are 15 μg/cm^2 for hydrogen, 0.5 mg/cm^2 for nitrogen, and 1.4 mg/cm^2 for argon [Bit79b, Bit79c]. While in operation, the input gas (after forming the target) is differentially pumped by three pumping stages consisting of combinations of roots and auxiliary pumps. The system is also pumped by a 6000-l/s oil diffusion pump, which keeps the beam line pressure at 10^{-4} to 10^{-6} mbar. The system has been designed to be transported relatively easily despite its large weight (around 7 tons) since it can be broken down into 4 pieces. This facilitated the target's use at various laboratories across Europe. A schematic diagram of the target is shown in Figure 3.5.

3.2.3 The Target at TUNL

The target, after being moved around Europe, was not used much during the latter half of the 1980's. In 1996 TUNL acquired it. As was stated above, much of the time

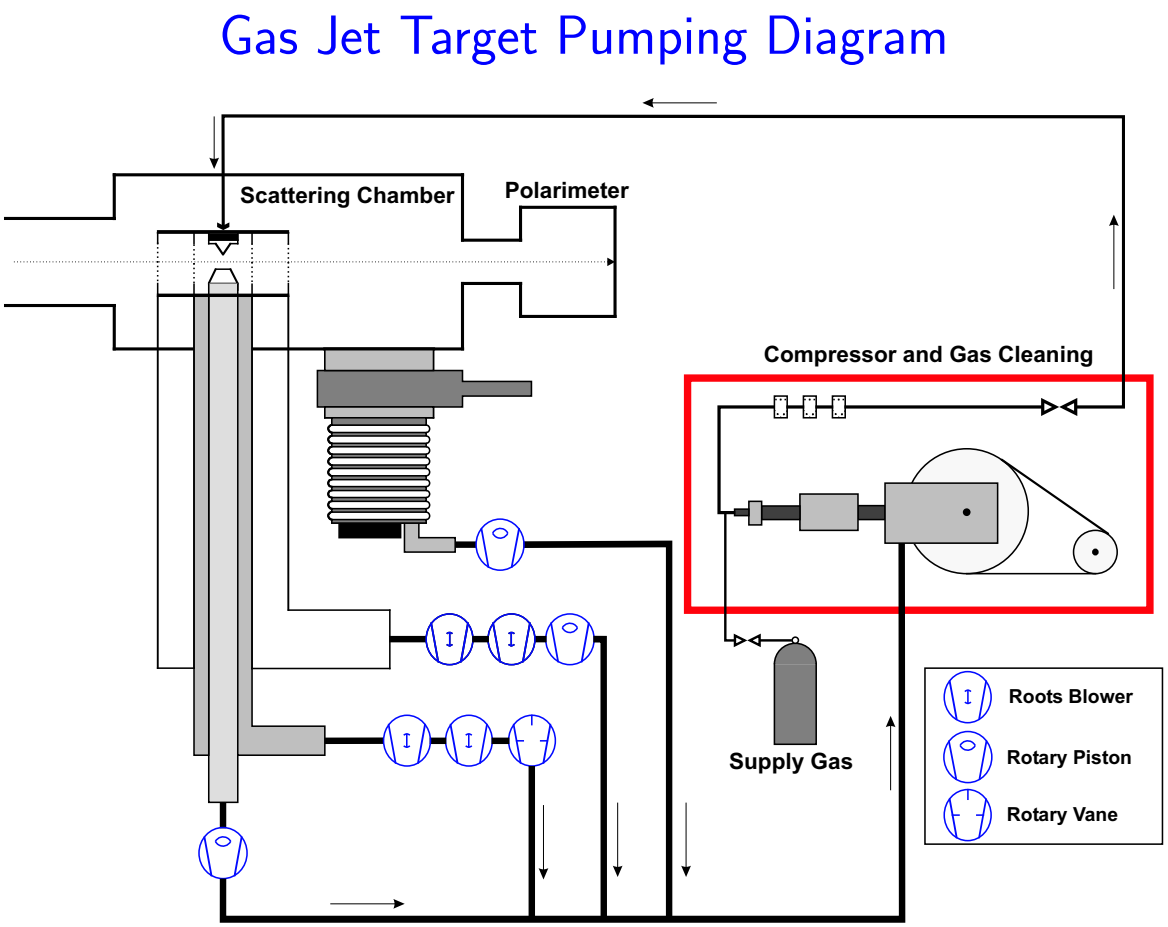

Figure 3.5: A schematic diagram of the gas jet layout. High pressure gas enters the vacuum chamber through an appropriately shaped nozzle. The majority of the jet is captured by the "catcher" directly underneath the nozzle. The rest of the target gas is pumped away by the differential pumping stages shown – combinations of roots blowers and rotary piston/vane pumps. The residual gas is pumped away by the very large diffusion pump. The re-compression/gas-cleaning system shown is currently under development.

spent on this research endeavor has gone into its refurbishment and upgrade.

The target arrived from Germany in June 1997 [Fis97b]. Because it is "portable," the possibility exists for the target to be moved to the Low-Energy Beam Facility [Gei98], but it was determined that experiments with the tandem accelerator would be performed first. Thus, all four "segments" of the target were moved to TUNL's Target Room One. Once there, after repairing some minor shipping damage, testing began on the rotary-piston pumps and roots blowers. The three rotary piston pumps were reconditioned to remove the decades-old oil inside in the hopes of improving their pumping speeds.

A system to exhaust the target gas out of the room was installed, which tapped into the existing tritium handling system in the laboratory. This allows for the exhaust gas from the pumping stages to be removed from the target room quickly. This is particularly important when running highly flammable hydrogen as the target gas.

The 44-degree beam-line leading from the 20-70 bending magnet was reconditioned with a new 600 l/s turbo-pump and new beam-scanner. After increasing the height of the system to match the laboratory's standard beam-line height, the target was eventually installed on this beam-line [Fis98]. The chamber was aligned and connected to the beam line and leak-chased.

The system originally ran with 380V power in Germany. Conversion to a U.S. standard 208V proved problematic because the wire sizes used in the pump control panel were too small, so a step-down transformer (to be used with an existing 480V main) was installed.

After the installation of 380V power into the room, the full pumping system was assembled, and pumping and leak tests on the individual stages began. With the proper power and exhaust system in place, tests of the whole target with nitrogen as the input gas were performed. The electrical current drawn by the complete set of 8 pumps was a reasonable 20A per phase. With an nitrogen input pressure of only 1500 mbar, however, the vacua in the various stages were significantly worse than those reported at a much higher input pressure by the group at Erlangen [Bit79b, Bit79c]. The target did not seem to be pumping away the target gas very efficiently [Fis99].

The roots blowers in stages 2 and 3 were discovered to be contaminated with oil. This was, after talking to a representative at Leybold, an indication that the o-ring gasket seals for the motor shaft on either end of the roots blowers had decayed and needed to be replaced. One of the roots blowers was sent away to be refurbished. The other two were determined to be beyond repair because of contamination and (mainly) age. They were replaced by new Leybold WS-1000 roots blowers, which were installed in place of the older pumps. The pumping efficiency of the system improved greatly with the new and refurbished pumps [Fis00]. With a typical input pressure of about 2 atm, the combined pumping has reduced the pressure to $\approx 8 \times 10^{-5}$ Torr at the beam entrance to the chamber.

Once the pumping system was operational, several tests needed to be performed to assess the suitability of the gas-jet target for measuring angular distributions of the differential cross section for proton-^{3}He elastic scattering, and other reactions in the future.

3.2.4 Clean Spectra and Target Profiling

As one of the first tests of the operational gas-jet target, a 3 MeV proton beam was tuned down the 44° leg to observe the elastic scattering of protons off a nitrogen gas jet [Fis99]. Clean spectra resulted, as shown in Figure 3.6.

For any sort of high-precision nuclear-physics measurement, information about the diameter, shape, homogeneity, and absolute thickness of the jet target zone is necessary. Many different methods of measuring the density profile of the gas jet have been used in the past, including: measuring the energy-loss of charged particles (usually from an α-source or beam from an accelerator) through the target [Bec82]; optical methods such as Schlieren photography [Bit79b, Bit79c]; laser-induced resonance fluorescence; and Raleigh scattering [Kre80a]; and an electron beam as an attenuation probe, a fluorescence probe, or as a large angle scattering probe [Tie79].

To make similar measurements of the TUNL gas-jet target, an accelerator-beam method was developed. A movable 1 mm diameter aperture was placed between the

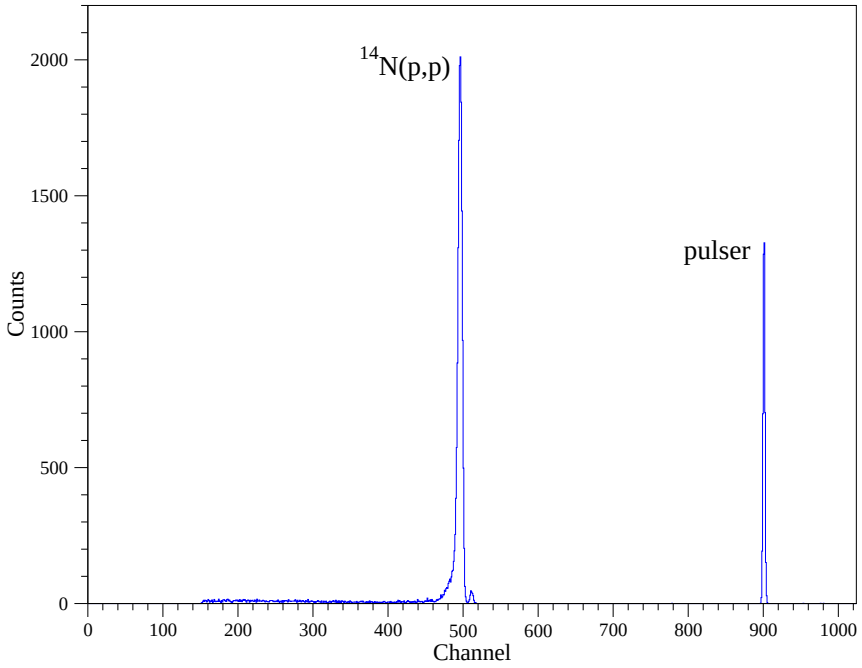

Figure 3.6: Elastic scattering spectrum from 3 MeV protons on a nitrogen gas jet at $\theta_{\text{lab}} = 20°$. The proton peak is on the left, and the peak on the right is a pulser.

entrance of the chamber and the target center, as shown in Figure 3.7. A 3-MeV proton beam from the tandem accelerator was tuned down the 44° beam-line to the gas-jet target. By moving the aperture across the incident beam, a density profile of the gas-jet was obtained from the elastic scattering yields in the detectors mounted in the chamber. A schematic of this apparatus is shown in Figure 3.7 The jet boundary is observed to be sharp, with a FWHM of about 1.5 mm, as shown in Figure 3.8(b).

The clean spectra that resulted from these experiments (see Figure 3.8(a)) and the tight geometry of the gas-jet gives credence that accurate angular distributions of cross-sections can be measured.

3.2.5 Target Thicknesses and Proton-Proton Scattering

For feasible $\sigma(\theta)$ measurements, a target of sufficient thickness is needed to keep counting times reasonable. Since the input pressure of the jet is selectable via a

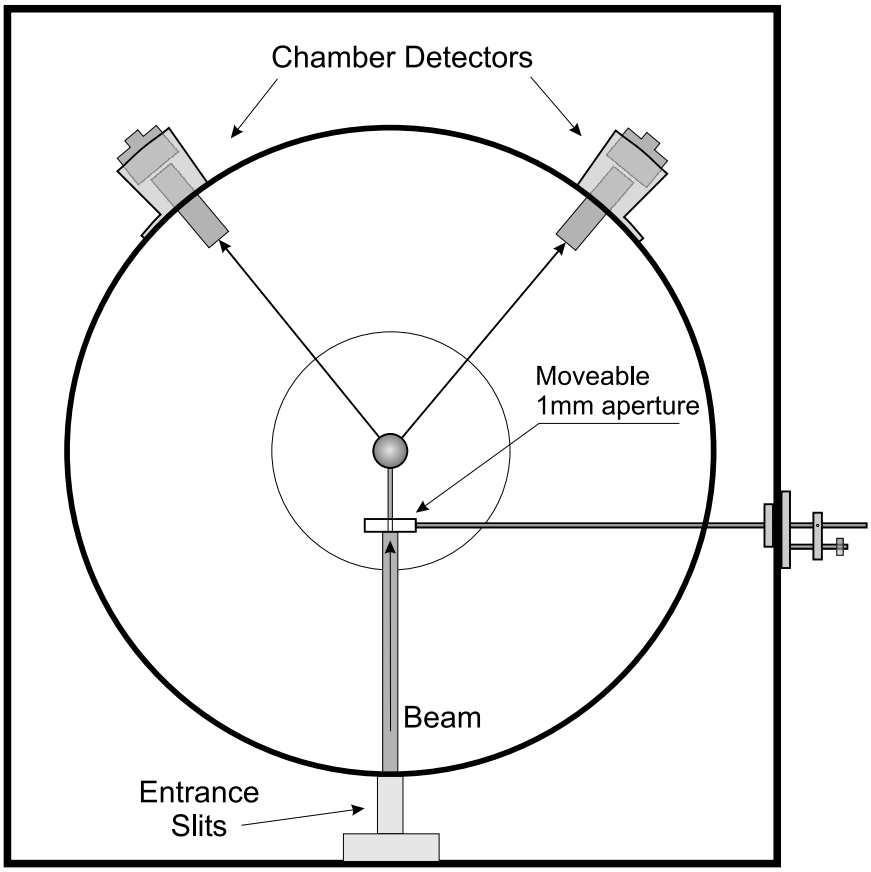

Figure 3.7: The gas-jet profiling apparatus. A wide beam enters the chamber and is intercepted by a 1mm diameter aperture which collimates the beam. The aperture can be adjusted from outside the scattering chamber. As the aperture is moved across the beam, it intercepts different parts of the jet which give different scattering yields in the chamber detectors depending on the jet's thickness.

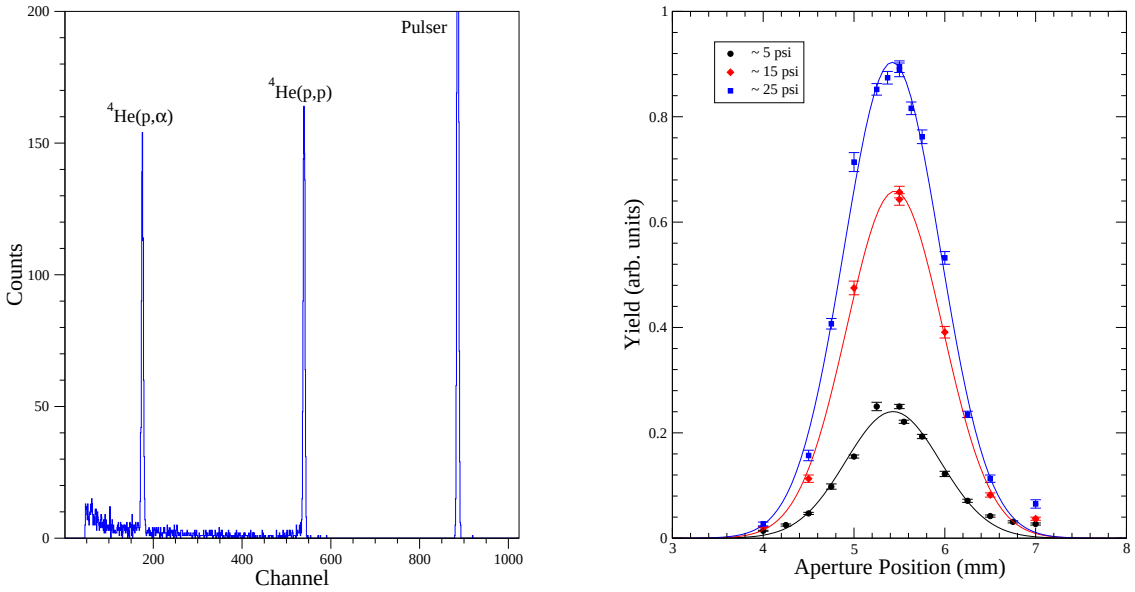

(a) Spectrum

(b) Gas-jet profiles

Figure 3.8: **(a)** Typical spectrum from elastic scattering of 3 MeV protons off a ^{4}He gas jet at $\theta_{lab} = 50°$. **(b)** The resulting gas-jet density profile at various input pressures.

pressure regulator and with a mass flow controller (MFC)[5], the target thickness of the gas jet target is variable. The mass-flow controller allows for a very controlled jet. It can maintain the flow into the nozzle to within 2 liters per minute at STP (SLM), with a reproducibility of 0.2%, allowing for consistent target thicknesses across different runs. Initial measurements using a 3-MeV proton beam scattering off ^{4}He target gas, using cross sections determined from an R-matrix analysis of previously measured ^{4}He(p,p)^{4}He data [Dod77], we obtain a thickness of $\approx 5.0 \times 10^{17}$ atoms/cm^2 with an input pressure of $\approx$ 2 bar. This target thickness was confirmed using the same input pressure conditions when measuring proton-proton scattering at E_{p}= 2.25 MeV. This proton target thickness is about a factor of two greater than that obtained using solid hydrogenated carbon targets [Bla00]. The substantial additional benefit in this case is the near total lack of carbon-related background. Throughout the measurements

[5]MKS Instruments Type 1559A, full scale 200 SLM, with Type 247 multichannel readout

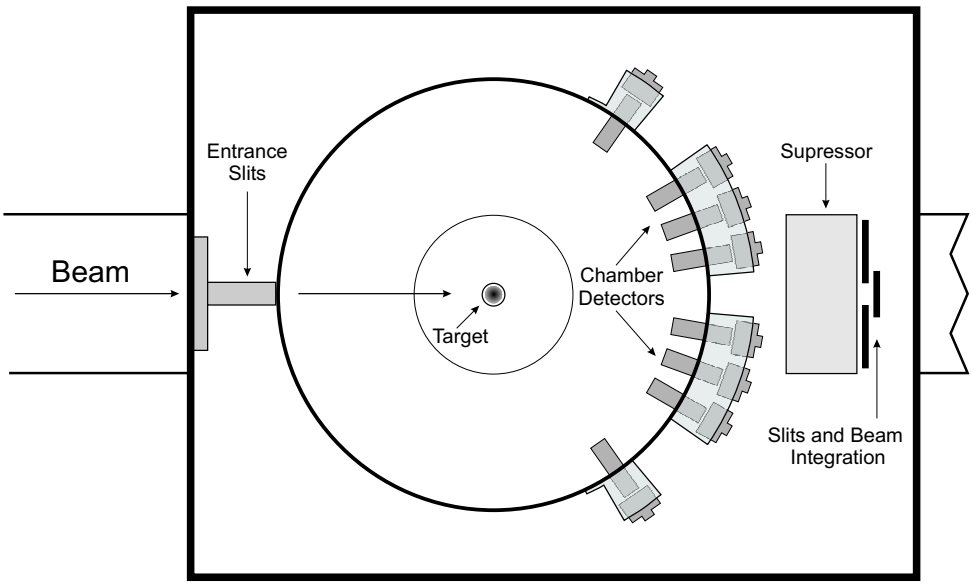

Figure 3.9: Gas-jet chamber setup used for the proton-proton scattering tests and beam current integration test. The beam integration plate and suppressor are shown.

using the gas-jet in this work, target thicknesses on the order of $\approx 5 \times 10^{17}$ atoms/cm^2 were obtained. This facilitated very reasonable counting times for the cross-sections measured.

The 2 bar input pressure is quite modest; tests with input pressures around 10 bar have been performed, with a small increase in the chamber pressure, but within the tolerable range for adjacent accelerator systems. This indicates that target thicknesses approaching 10^{19} atoms/cm^2 are possible. However, target thickness measurements were not made with these input pressures since the accelerator was not available at the time.

A system for mounting detectors about the scattering region was designed, built, and installed for performing angular distribution measurements. Up to four pairs of detectors can be mounted symmetrically about the scattering region at angles ranging from 7.5 to 75 degrees. It also allows for monitor detectors to be used at either more forward or more backward angles. The zero-angle of this apparatus has been checked with ^{40}Ar(p,p)^{40}Ar Rutherford scattering, which shows a very small $\approx 0.3^\circ$ offset. A schematic of the detector holders inside the gas-jet scattering chamber is shown in Figure 3.9. For further discussion of the zero-angle checks, see Section 4.4.3.

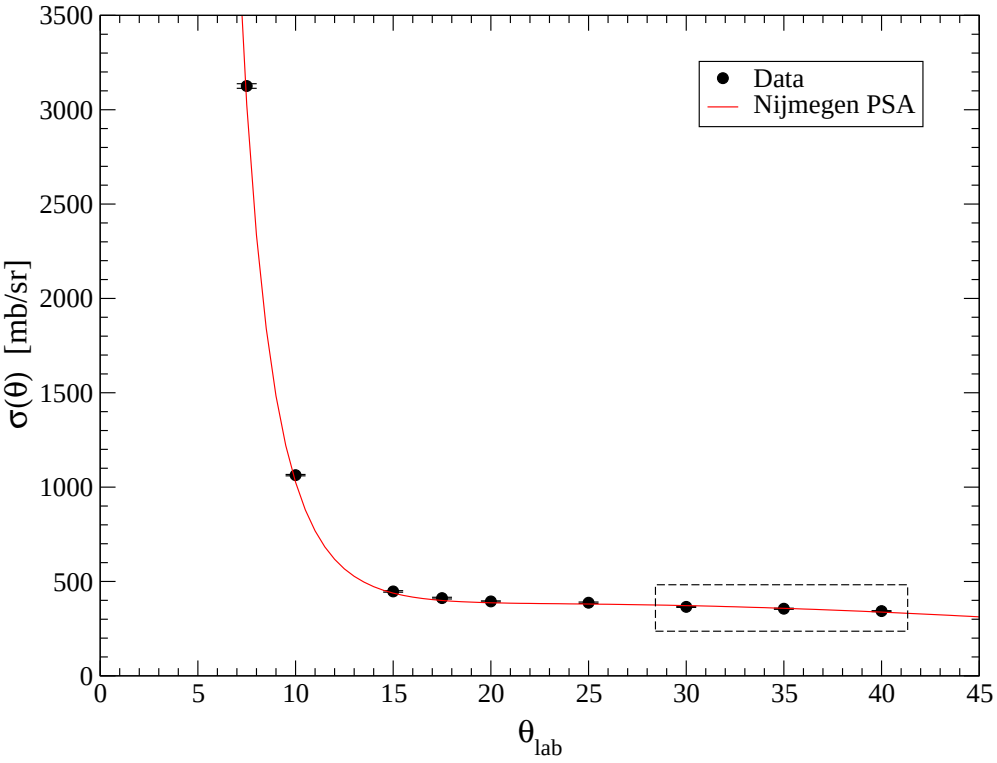

Figure 3.10: The relative angular distribution of the cross-section of proton-proton scattering measured at $E_{\mathrm{p}} = 2.25$ MeV. The data were normalized by scaling the entire distribution such that the 3 points inside the dashed box matched the Nijmegen PSA prediction.

To test the feasibility of measuring differential cross sections using the gas-jet target, we measured the relative differential cross section angular distribution of proton-proton scattering at $E_p = 2.25$ MeV and compared it to the phase-shift analysis (PSA) prediction of the Nijmegen group [Sto93]. Using the three most backward points to normalize the measured relative distribution of proton-proton scattering to the PSA prediction, very good agreement has been obtained between the measured and calculated yields at more forward angles, as can be seen in Figure 3.10. These results indicate that other angular distributions can be obtained reliably.

3.2.6 Beam Integration and Target Reproducibility

When measuring absolute cross-sections, one needs accurate measure of the number of beam particles traversing the target. This is often performed using a beam-current integrator, where the charge of the incident beam is summed electronically. However, if some of the beam picks up electrons while passing through the jet, this method is no longer accurate.

To check whether or not this was happening with certain beams, a method for measuring this potential systematic error was developed. A beam was tuned into the gas-jet target chamber onto the gas-jet, and then integrated by the metal plate in the rear of the chamber, as shown in Figure 3.9. At roughly 30 s intervals, the gas jet was turned off, allowing the beam to be integrated. With the jet off an accurate measure of the "true" beam current was obtained. The jet was then turned back on for ≈ 30 s, to determine the measured beam current while the jet was on. Because of potential beam fluctuations from other sources (i.e. tandem or ion-source instabilities) this procedure was computer controlled and repeated about 50 times for each beam/target combination measured. The results are shown in Figure 3.12. As can be seen, on average, there is more integrated charge when the gas-jet is off than on. Taking these on-off data pairwise, an overall On/Off ratio can be calculated, as shown. Table 3.2 summarizes the results of these measurements for the beams used in this work. As can be seen, the charge-exchange effect decreases with increasing energy, as is expected.

Table 3.2: Beam-current integration correction factors, as determined by the gas-on/gas-off procedure described in Section 3.2.6. As can be seen, the charge-exchange effect decreases with increasing beam energy. These factors were applied, as needed, in the analysis.

Energy [MeV]	Beam Type	Factor
2.223	Proton	1.019 ± 0.011
2.968	$^3He^{++}$	1.060 ± 0.010
4.756	$^3He^{++}$	1.028 ± 0.003
6.685	$^3He^{++}$	1.025 ± 0.011
9.305	$^3He^{++}$	1.004 ± 0.005
12.061	$^3He^{++}$	1.007 ± 0.010

These "BCI Correction Factors" are plotted as a function of $^3He^{++}$ energy in Figure 3.11.

During periods when the gas-jet was on, the scattered particles were detected with a pair of detectors in the chamber. Integrated beam-current yields are plotted at the bottom of Figure 3.12. This check ensured that the target thickness of the gas-jet was reproducible from run to run. As can be seen, the stability of the gas jet is quite good. The statistical fluctuation from run to run is well within the statistical uncertainties. The jet thickness is reproducible to within 2%.

3.2.7 Future Work: Recirculation and Gas-Cleaning

Even at the modest input pressure of 2 bar, the target consumes gas rapidly. In its current setup, the exhaust gas from the pumping system is vented outside the laboratory building. During a typical run, a standard 2200 psi pressurized gas cylinder depletes in about 8 hours. This is acceptable when running with standard industrial-grade hydrogen or similarly cheap gases; it does become problematic when using much more expensive gases or when running with much higher target thicknesses.

In such cases, a system to capture the exhaust gas from the pumping system, remove impurities from the exhaust, and then re-compress the gas for injection into

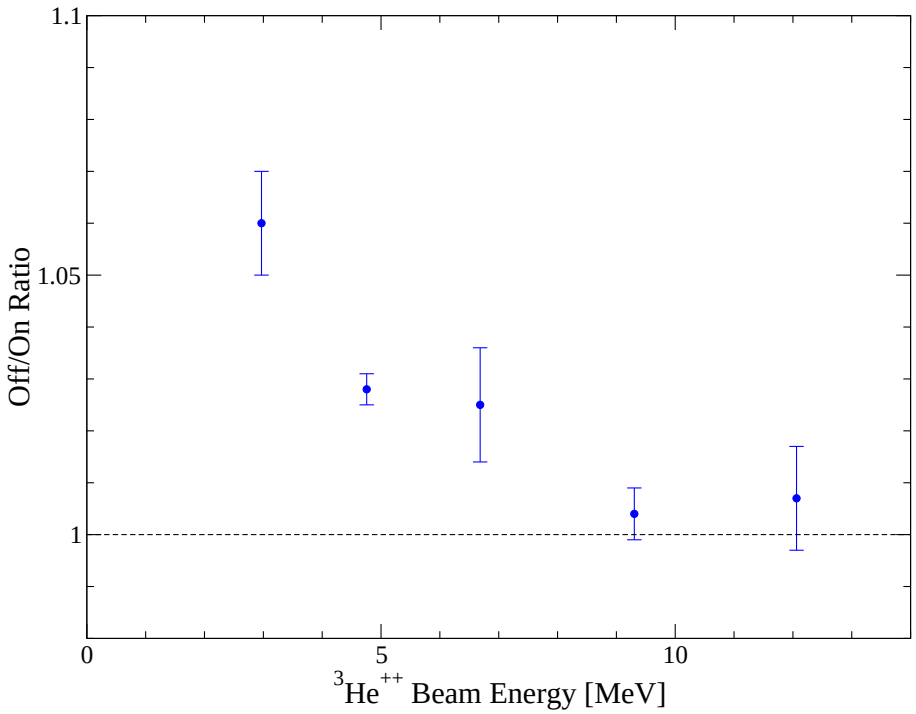

Figure 3.11: Plot of beam-current integration correction factors as function of $^3He^{++}$ beam energy.

the target becomes desirable. Such a system did exist when the target was used in Europe, including a massive custom-made compressor. However, it was decided that this system was out of date and composed of parts not easily replaced. Therefore, a new system has been designed. The components for this system have been purchased, and assembly is in progress, with a design goal of reclaiming at least $\approx 95\%$ of the exhaust target gas and cleaning it to a purity approaching 99% [Gup02].

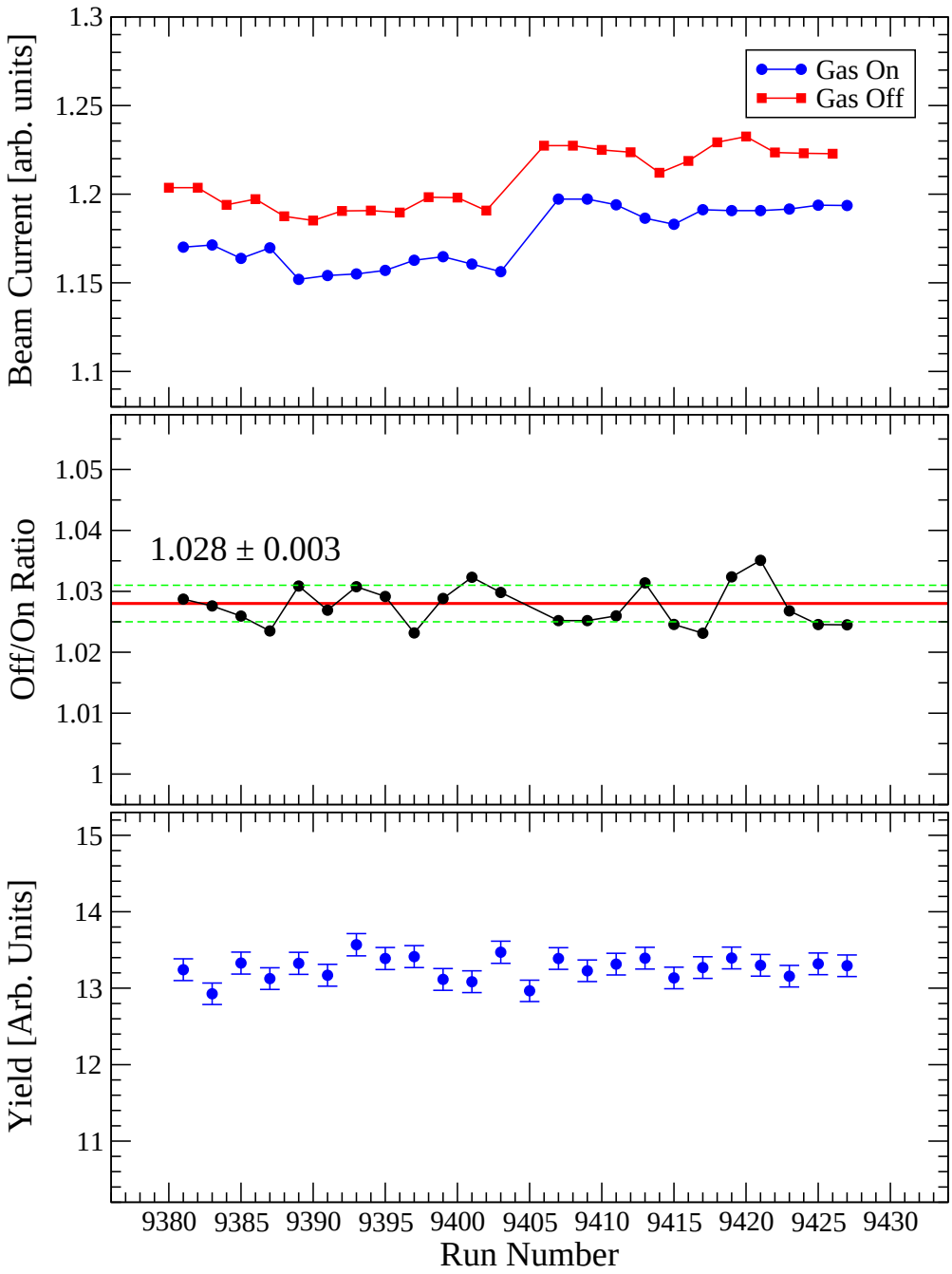

Figure 3.12: Results from beam-current integration and stability tests performed with a 4.756 MeV $^3He^{++}$ beam on a hydrogen gas-jet. The upper plot shows the integrated charge as a function of run number ($\propto$ time) for runs where the gas-jet was on and off. As can be seen there is, on average, more integrated charge when the gas-jet is off than on, as shown in the middle plot. The bottom plot shows the integrated beam-current normalized-yields from p-^{3}He elastic scattering at 25° in each of the gas-on runs. The jet shows very good stability; the statistical fluctuations are all within the counting statistics of each run.

Chapter 4

Experiments

Angular distributions of the cross section and proton analyzing power were measured at five energies below $E_p = 5$ MeV for this work. In this chapter, a brief review of the general formalism connecting the fundamental quantum mechanics to observables in the laboratory is presented, followed by more specific experimental details.

4.1 General Formalism

The scattered wave function of two spin-$\frac{1}{2}$ particles is written as a vector

$$\Psi^{(n)} = e^{i(\boldsymbol{k}_i \cdot \boldsymbol{r})}\chi^{(n)} + f^{(n)}\frac{e^{ikr}}{r}, \tag{4.1}$$

where the form factor $f^{(n)}$ is defined by

$$f^{(n)} = M\chi^{(n)}. \tag{4.2}$$

$\chi^{(n)}$ is a four-component vector representing the initial spin states n of the two incoming particles, and M is a 4×4 matrix that operates on that initial spin state. Since this is elastic scattering, $|\boldsymbol{k}_i| = |\boldsymbol{k}_f| = k$ and $\boldsymbol{r}$ is the distance vector between the two incoming particles ($r = |\boldsymbol{r}|$).

Using the unit vectors defined as

$$\hat{l} = \frac{\boldsymbol{k}_i + \boldsymbol{k}_f}{|\boldsymbol{k}_i + \boldsymbol{k}_f|}, \quad \hat{m} = \frac{\boldsymbol{k}_i - \boldsymbol{k}_f}{|\boldsymbol{k}_i - \boldsymbol{k}_f|}, \text{ and } \quad \hat{n} = \frac{\boldsymbol{k}_i \times \boldsymbol{k}_f}{|\boldsymbol{k}_i \times \boldsymbol{k}_f|}, \tag{4.3}$$

La France and Winternitz have parameterized the M matrix as [Fra80]

$$M(\boldsymbol{k}_f, \boldsymbol{k}_i) = \frac{1}{2}\Big\{(a+b) + (a-b)(\boldsymbol{\sigma}_1 \cdot \hat{n})(\boldsymbol{\sigma}_2 \cdot \hat{n}) + (c+d)(\boldsymbol{\sigma}_1 \cdot \hat{m})(\boldsymbol{\sigma}_2 \cdot \hat{m}) + (c-d)(\boldsymbol{\sigma}_1 \cdot \hat{l})(\boldsymbol{\sigma}_2 \cdot \hat{l}) + e(\boldsymbol{\sigma}_1 + \boldsymbol{\sigma}_2) \cdot \hat{n} + f(\boldsymbol{\sigma}_1 - \boldsymbol{\sigma}_2) \cdot \hat{n}\Big\}, \quad (4.4)$$

where $\boldsymbol{\sigma}_1$ and $\boldsymbol{\sigma}_2$ are Pauli spin-operators that act on the spin wave functions of the proton and ^{3}He nucleus, respectively, and a, b, c, d, e and f are complex functions of energy and angle. These six amplitudes contain all the nuclear physics information that can be gleaned from a scattering experiment.

This M-matrix can be used to calculate the cross-section and analyzing power observables

$$\sigma_0 = \frac{1}{4}\,\mathrm{Tr}[MM^\dagger] = \frac{1}{2}\left(|a|^2 + |b|^2 + |c|^2 + |d|^2 + |e|^2 + |f|^2\right) \quad (4.5)$$

$$\sigma_0 A_{y0} = \frac{1}{4}\,\mathrm{Tr}[M\sigma_{1_y}\mathbb{1}M^\dagger] = \mathrm{Re}\left(a^* e + b^* f\right), \quad (4.6)$$

where $\mathbb{1}$ is the unit matrix. Equations 4.5 and 4.6 can serve as theoretical definitions of the differential cross section $\frac{d\sigma}{d\Omega}(\theta) \equiv \sigma(\theta) \equiv \sigma_0$, and the proton analyzing power $A_y \equiv A_{y0}$. In Sections 4.4.1 and 4.5.1, these observables will be defined in terms of measurable quantities in the laboratory. Measurements of $\sigma(\theta)$ and A_y were made of for this work. Other polarization observables (such as the ^{3}He analyzing power A_{0y}, and the spin-correlation coefficients A_{yy}, A_{xz}, etc.) can be defined in similar ways [Fra80, All93b].

The measured angular distributions were fit using a single-energy phase-shift analysis, which is another parameterization of this M-matrix, effectively finding the best values for a, b, c, d, e and f.

4.2 Detectors and Data-Acquisition Hardware

Silicon charged particle detectors were used for both the A_y and $\sigma(\theta)$ measurements. Older evaporated-gold surface-barrier detectors were used, as well as newer ion-implanted detectors. These detectors have an effective efficiency for detecting

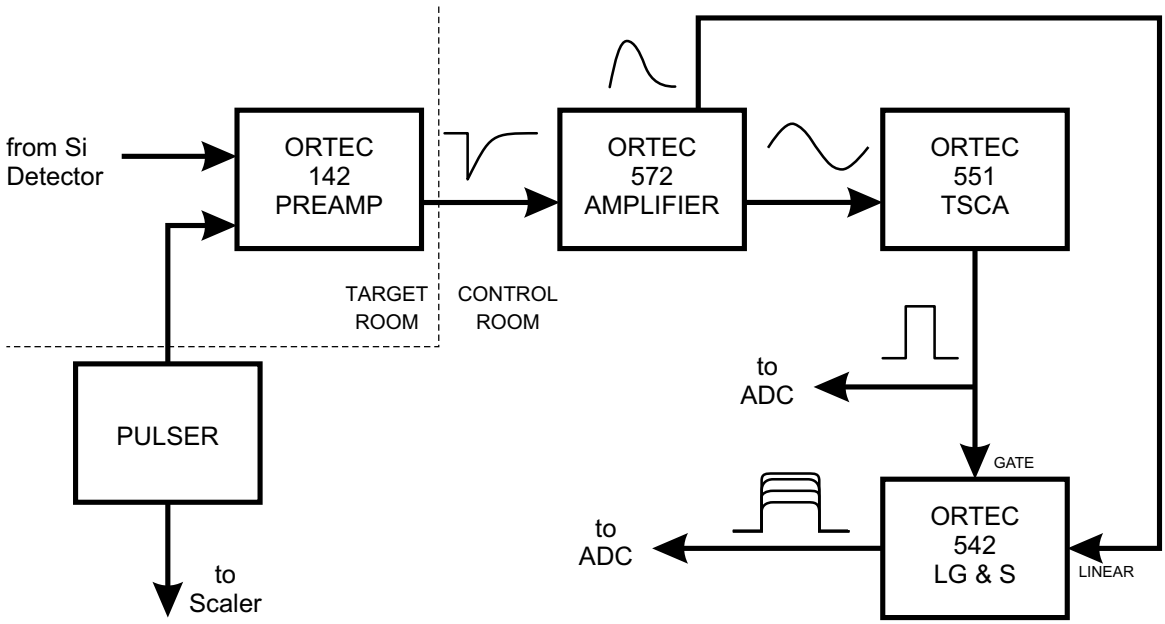

Figure 4.1: Standard electronics setup for both A_y and $\sigma(\theta)$ measurements. For the A_y measurements, histograms were accumulated in separate data areas depending on the spin-state of the polarized beam.

charged particles at these energies of $100.0 \pm 0.1\%$. This uncertainty arises from inelastic scattering from the ^{28}Si in the detector [Zab80]. This effect is small enough to be negligible at these energies. Thus, the intrinsic detector efficiency ϵ is assumed to be unity.

The standard electronics setup for a detector is shown in Figure 4.1. This is the setup used for both A_y and $\sigma(\theta)$ measurements. The signal from each detector was collected by a preamplifier located at the scattering chamber. The preamplifier output was sent to the remainder of the electronics in the control room, where it was amplified and shaped by the amplifier. The unipolar output of the amplifier was sent directly to a Linear Gate & Stretcher (LG&S) where it was shaped (as shown) for processing by the ADC as an energy signal. The bipolar signal from the amplifier was sent to a Timing Single-Channel Analyzer (TSCA) to create a TTL logic gate. This TTL signal triggers the LG&S and the incoming energy signal at the ADC. By raising the lower-level discriminator on the TSCA, low energy detector noise can be removed from the spectrum.

Six Northern NS621 CAMAC ADCs were used for this work. They were 50 or 100 MHz Wilkinson-type peak-sensing ADCs. Since eight detectors were typically used in this work, two pair of the detectors were routed into single ADCs. A Micro-programmed Branch Driver (MBD) was used to poll the ADCs when they received an event and then pass the data onto the microVAX computer running the TUNL-developed XSYS acquisition software [Set95]. This software sorted the incoming event data into histograms for analysis.

The output from a pulse generator was sent to the test input of the preamplifier; its signals were added at the preamp to the data-stream and were treated by the rest of the electronics like normal detector signals. The number of generated pulses were counted with a scaler to be compared with the number appearing in the final spectrum. This provided a measurement of the overall electronic dead-time of the system.

4.3 Bending Magnet Calibration

An accurate measure of the beam energy is needed for all of the experiments performed for this work. The beams used were accelerated by the 10-MV FN tandem accelerator at TUNL and bent by a dipole magnet into either the 62-cm scattering chamber on the 52° beamline, or the gas-jet target on the 44° beamline. The dipole magnet and the slit-control feedback system of the tandem accelerator kept the beam on target at the desired energy.

The magnetic field of the dipole magnet was measured using an NMR magnetometer, which needed to be calibrated for each beamline. In each case the calibration was performed by increasing the magnetic field and measuring the yield of a resonance or threshold reaction. The 52° beamline had been previously calibrated [Fis97a], and the 44° beamline was calibrated for this work. A detailed discussion of both these calibrations is included in Appendix B.

Theoretically, once the 52° beamline was calibrated, the 44° beamline should have been as well, since the two calibrations are related by a purely geometric factor. How-

Table 4.1: Beam energies (in MeV) used in this work. The left half of the table lists the energies at which the A_y measurements were made in the 52° beamline, and the right hand side lists the energies at which the $\sigma(\theta)$ measurements were made in the 44° beamline. These two sets of energies do not match up exactly because of the differences in magnet calibrations for the two beamlines.

A_y Energies			$\sigma(\theta)$ Energies		
E_{cm}	**p Energy**	^{3}He Energy	E_{cm}	p Energy	**^{3}He Energy**
0.75	1.00	2.99	0.74	0.99	2.97
1.20	1.60	4.79	1.19	1.59	4.76
1.69	2.25	6.73	1.67	2.24	6.69
2.35	3.13	9.36	2.33	3.11	9.31
3.03	4.05	12.11	3.02	4.02	12.06

ever, as is shown in Appendix B, this was not the case. Since the magnet calibration for the 44° beamline was performed after several of the relative $\sigma(\theta)$ distributions described in Section 4.4.2 were made, the energies of the A_y measurements do not exactly match those of the $\sigma(\theta)$ measurements, as shown in Table 4.1.

4.4 The Differential Cross Section $\sigma(\theta)$

4.4.1 Formalism and Definitions

The number of particles N scattered from a beam of energy E into a detector placed at an angle θ relative to the incident beam is given by

$$N(E,\theta) = n_b\ t\ \epsilon\ \Delta\Omega\ \frac{d\sigma}{d\Omega}(E,\theta), \tag{4.7}$$

where n_b is the number of incident beam particles, t is the areal density of target centers, ϵ is the efficiency of the detector used, $\Delta\Omega$ is the solid-angle subtended by the detector, and $\frac{d\sigma}{d\Omega}(E,\theta)$ is the differential cross-section for the scattering, which is often abbreviated to $\sigma(\theta)$. To determine $\sigma(\theta)$, of course, all the other parameters in equation 4.7 must be measured precisely.

To obtain the *shape* of the angular distribution we can perform a relative measurement, where we determine the yield of particles at a certain angle, normalized to some fixed detector at θ_{mon}, which has (potentially) a different solid angle $\Delta\Omega_{mon}$. So at a fixed energy, the yield at a certain angle is

$$Y(\theta) = \frac{N(\theta)}{N(\theta_{mon})} = \frac{\cancel{n_b t}\ \epsilon\ \Delta\Omega\ \sigma(\theta)}{\cancel{n_b t}\ \epsilon_{mon}\ \Delta\Omega_{mon}\ \sigma(\theta_{mon})}. \tag{4.8}$$

As can be seen, n_b, and t cancel out, and $\epsilon = \epsilon_{mon} = 1$ as discussed in Section 4.2. What is most important is that $Y(\theta) \propto \sigma(\theta)$. This is called a relative angular distribution.

Measuring the absolute normalization of this relative $\sigma(\theta)$ distribution involves very precise knowledge of n_b, t, and $\Delta\Omega$, each of which has their own experimental difficulties. Methods for determining the absolute normalization will be discussed in Sections 4.4.4 and 4.4.5.

4.4.2 Relative Angular Distribution

Measurements of relative angular distributions of $\sigma(\theta)$ were made at 5 energies using the gas jet target. Since ^{3}He is a very expensive gas[6], the measurements were performed in "inverse kinematics" using a ^{3}He beam incident on a hydrogen gas-jet. The energies at which measurements were made along with equivalent proton and ^{3}He energies are given in Table 4.1. A kinematics plot of scattered particle energy as a function of laboratory angle is shown in Figure 4.2. Because of the kinematics of the heavier ^{3}He beam scattering off the hydrogen target, ^{3}He particles can only be detected forward of $\approx 19°$. Detecting both particles gives a complete angular distribution in the center of mass.

For each energy in Table 4.1, a beam of $^3He^{++}$ ions was accelerated with the FN tandem accelerator and then deflected onto the hydrogen gas-jet target. The elastically scattered protons and ^{3}He nuclei were detected by three pairs of silicon

[6]$1000 for a 10L (STP) bottle. Given the gas-consumption of the gas jet target, it was calculated that for a 2 day run, the ^{3}He cost would run into the several million dollar range.

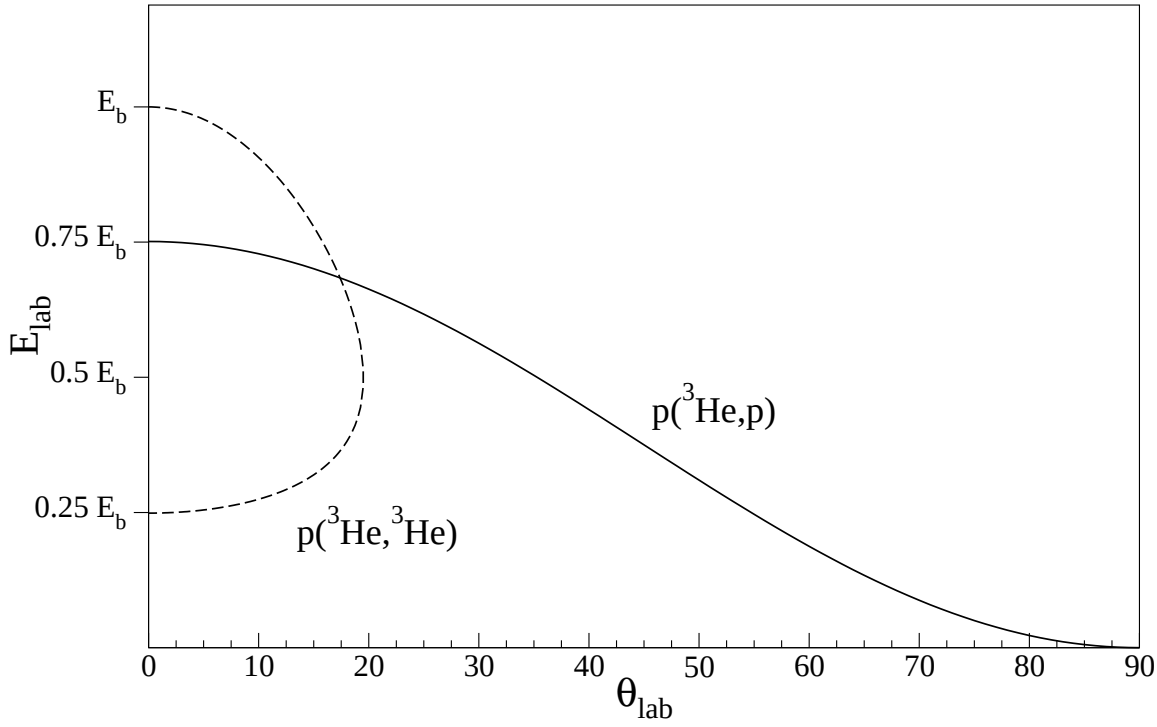

Figure 4.2: Kinematics plot for ^{3}He beam on hydrogen target. The vertical axis is the lab energy the scale of which is set by the beam energy shown. ^{3}He particles cannot be detected at angles backward of $\approx 19°$.

Table 4.2: $\sigma(\theta)$ relative distribution angle settings, in degrees, used in acquiring the data.

Monitors at 55°			Monitors at 15°		
R1/L1	R2/L2	R3/L3	R1/L1	R2/L2	R3/L3
7.5	17.5	27.5	25	35	45
10	20	30	40	50	60
15	25	35	45	55	65
25	35	45	50	60	70
			55	65	75

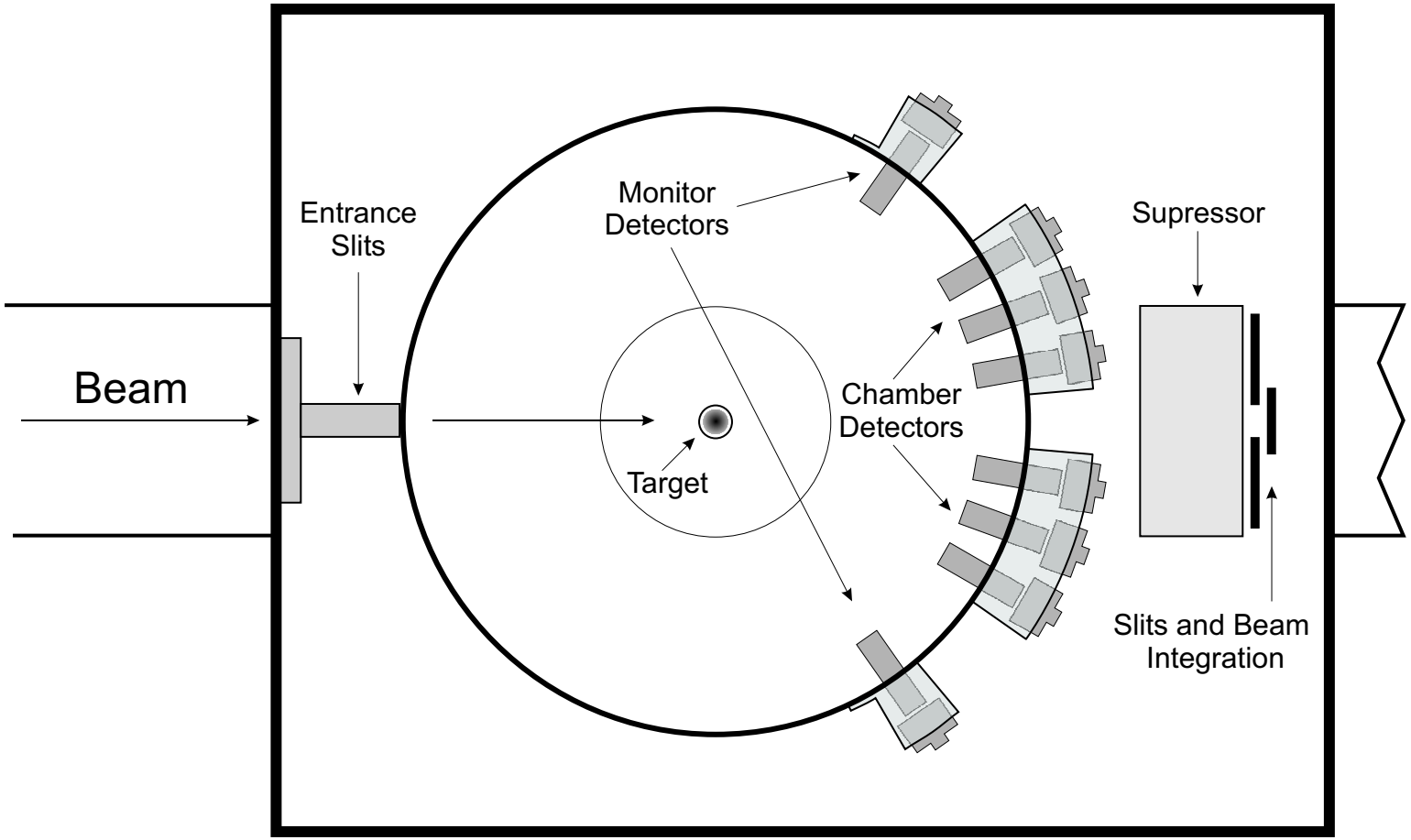

Figure 4.3: Chamber setup for $\sigma(\theta)$ measurements. The chamber detectors are arranged symmetrically about the beam direction. For the relative $\sigma(\theta)$ measurements, the yields in the chamber detectors were normalized to the counts in the fixed monitor detectors shown. The beam position was monitored using a set of slits behind the target, and the beam current was integrated by summing the slits and back plate behind them.

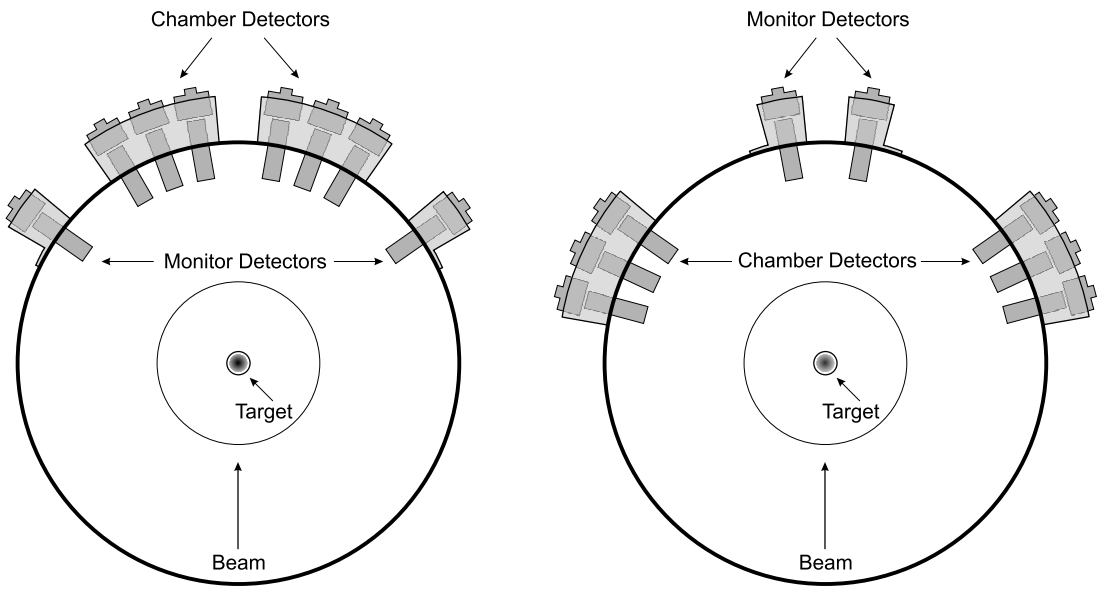

(a) Forward Angle Setup

(b) Backward Angle Setup

Figure 4.4: Chamber setups for forward and backward angle relative $\sigma(\theta)$ measurements.

detectors placed symmetrically about the beam direction. A diagram of the chamber setup is shown in Figure 4.3. The counts in each detector were normalized to the yield of scattered particles in a pair of monitor detectors also placed symmetrically about the scattering region. The angular range covered with the movable chamber detectors was 7.5° to 75°. A typical spectrum is shown in Figure 4.5. The beam position relative to the jet-target was monitored by a set of Up-Down-Left-Right slits behind the target region. Also the beam passing through the very small slit opening was integrated by another plate which is electrically isolated from the slits. For each measurement the beam current was maximized on this rear plate, thus making sure that the scattering geometry remained the same from run to run. The currents from the slits and integration plate were summed and used to measure the total beam current, and therefore n_b.

Since the monitor detectors are in the same plane as the chamber detectors, two monitor position setups were employed. When measuring forward angles, the monitor detectors were located at 55°. When measuring backward angles, the monitor detectors

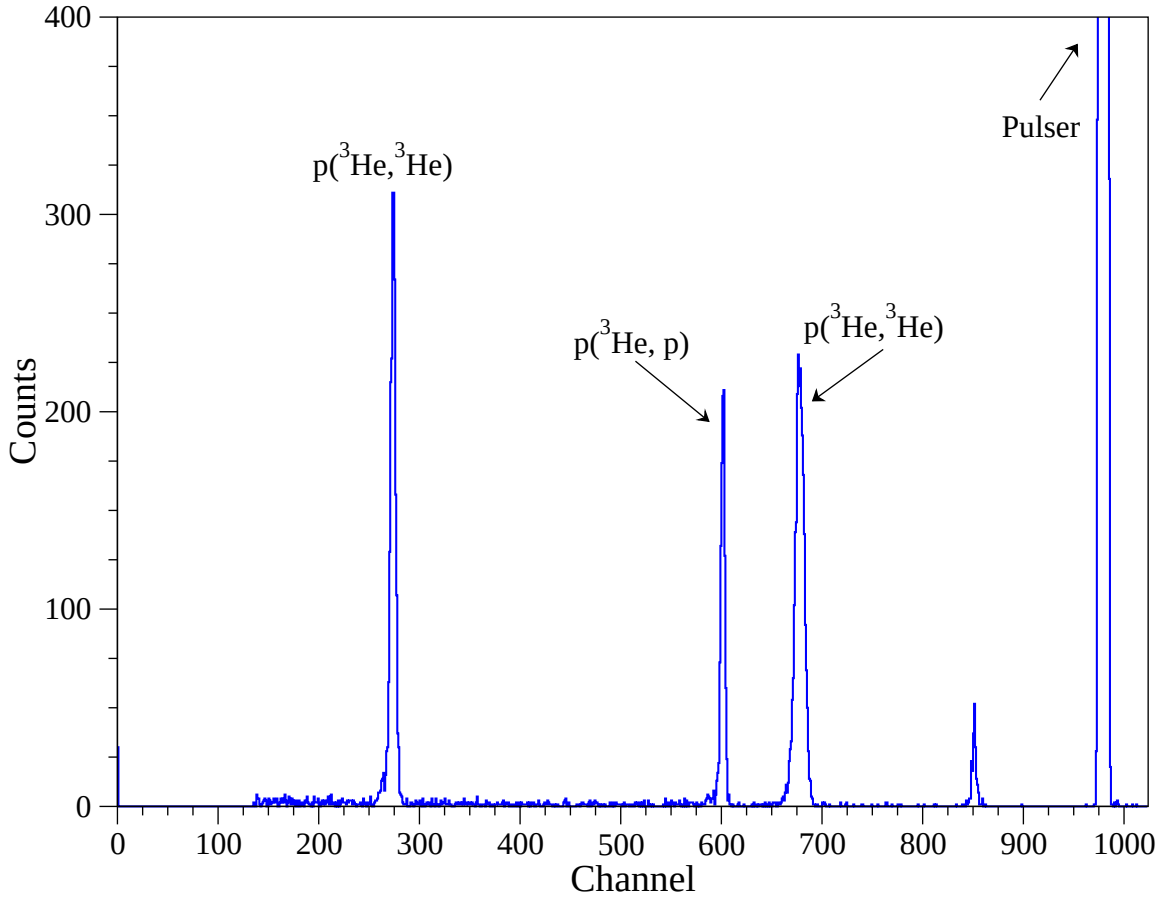

Figure 4.5: Typical spectrum of ^{3}He beam on a proton target. This spectrum was measured at $\theta = 15°$ at a ^{3}He beam energy of 6.73 MeV. The peak at channel 850 is caused by heavier gas contaminants.

were located at 15°. Table 4.2 lists the laboratory angle settings where measurements were made at each energy, and the two monitor detector setups are shown in Figure 4.4. When it was time to change from the forward monitor setup to the backward monitor setup, the chamber detectors were kept in place (at 25°/35°/45°, as listed in Table 4.2) to act as a cross-normalization of the backward-angle data to the forward-angle data. The detector and collimator parameters for the relative $\sigma(\theta)$ measurements are listed in Table 4.3.

Table 4.3: Detector thicknesses (T) and collimator setups for relative $\sigma(\theta)$ measurements. All lengths are in mm unless stated. All detectors were 16.6 cm from the target center, and each detector was fitted with a 5.1 cm snout. H is the horizontal collimator dimension and V is the vertical collimator dimension. The "Forward Angles" column shows the detector setups for forward angle measurements (with the monitors at 55°) and the "Backward Angles" column shows the setup for backward angle measurements (with the monitors at 15°.)

^{3}He		Forward Angles			Backward Angles		
Energy	Detector	Front	Rear	T	Front	Rear	T
(MeV)		H × V	H × V	(μm)	H × V	H × V	(μm)
2.97	R1-3, L1-3	2.4 × 9.5	0.8 × 9.5	300	2.4 × 9.5	0.8 × 9.5	300
	RM, LM	6.4 × 9.5	6.4 × 9.5	300	2.4 × 9.5	0.8 × 9.5	300
4.76	R1-3	2.4 × 9.5	0.8 × 9.5	300	3.2 × 9.5	1.6 × 9.5	300
	L1	2.4 × 9.5	0.8 × 9.5	500	3.2 × 9.5	1.6 × 9.5	500
	L2, L3	2.4 × 9.5	0.8 × 9.5	300	3.2 × 9.5	1.6 × 9.5	300
	RM, LM	6.4 × 9.5	6.4 × 9.5	300	2.4 × 9.5	0.8 × 9.5	300
6.69	R1	2.4 × 9.5	0.8 × 9.5	500	2.4 × 9.5	0.8 × 9.5	500
	R2, R3	2.4 × 9.5	0.8 × 9.5	300	2.4 × 9.5	0.8 × 9.5	300
	L1-L3	2.4 × 9.5	0.8 × 9.5	300	2.4 × 9.5	0.8 × 9.5	300
	RM, LM	6.4 × 9.5	6.4 × 9.5	300	2.4 × 9.5	0.8 × 9.5	300
9.31	R1, L1	2.4 × 9.5	0.8 × 9.5	1000	3.2 × 9.5	1.6 × 9.5	300
	R2, L2	2.4 × 9.5	0.8 × 9.5	500	3.2 × 9.5	1.6 × 9.5	500
	R3, L3	2.4 × 9.5	0.8 × 9.5	300	3.2 × 9.5	1.6 × 9.5	300
	RM, LM	6.4 × 9.5	3.2 × 9.5	300	2.4 × 9.5	0.8 × 9.5	1000
12.06	R1, L1	2.4 × 9.5	0.8 × 9.5	1000	2.4 × 9.5	0.8 × 9.5	1000
	R2	2.4 × 9.5	0.8 × 9.5	2000	2.4 × 9.5	0.8 × 9.5	2000
	L2	2.4 × 9.5	0.8 × 9.5	1000	2.4 × 9.5	0.8 × 9.5	1000
	R3, L3	2.4 × 9.5	0.8 × 9.5	500	2.4 × 9.5	0.8 × 9.5	500
	RM, LM	6.4 × 9.5	6.4 × 9.5	1000	2.4 × 9.5	0.8 × 9.5	1000

Table 4.4: Zero-angle offsets

Date	Zero-angle Offset
March 2001	-0.382 ± 0.005
August 2001	-0.319 ± 0.004
June 2002	-0.354 ± 0.006

4.4.3 Zero-crossing

To determine the zero-angle offset of the detector holder ring, each holder measured the yield of protons from ^{40}Ar(p,p)^{40}Ar Rutherford scattering at $E_p = 2.25$ MeV, from θ = -35° to 35°. The counts in each detector were normalized to monitors at 55°. The yield versus lab angle for each detector was fit to the Rutherford scattering formula, with the zero-offset as a fitting parameter. This check was performed several times throughout the data taking, especially after the target chamber was periodically re-aligned. The values of the offset from the fits are given in Table 4.4. The zero-offsets did not change much from measurement to measurement.

The zero-angle offset was also determined by the relative positions of peaks in spectra from a ^{3}He beam scattering from a hydrogen target. For spectra measured at angles forward of 19°, there are three peaks. The kinematics of the scattering are constrained such that the ratio of peak separations uniquely determines the scattering angle. The sensitivity to this method is greatest near the intersection of the proton and ^{3}He branches, as shown in Figure 4.2. This method has been used to determine the angle offsets at 17.5°. They agree with the offsets determined from ^{40}Ar(p,p)^{40}Ar Rutherford scattering.

Since the offset for both the right detectors and left detectors are the same, the use of symmetric pairs of detectors allow the effect of the angular offset to cancel to first order in $\sigma(\theta)$. Only at very forward angles where $\sigma(\theta)$ changes quickly with angle does the difference in counting rates for left and right detectors become an issue.

4.4.4 Absolute Normalization – Mixed Jet

The absolute normalizations of the relative $\sigma(\theta)$ distributions have been measured in two different ways. Both involve methods of either measuring the target thickness and detector solid angles indirectly, or in a way where they cancel out.

In the first method, we normalize our proton-^{3}He elastic scattering to ^{3}He–^{40}Ar Rutherford scattering. Bombarding a target containing both hydrogen and argon with a ^{3}He beam, we can calculate the ratio of the proton–^{3}He yield to the ^{3}He-^{40}Ar yield in the same detector,

$$\underbrace{\left[\frac{N_{\mathrm{pHe}}}{N_{\mathrm{ArHe}}}\right]}_{R_c} = \underbrace{\left[\frac{t_{\mathrm{p}}}{t_{\mathrm{Ar}}}\right]}_{R_t} \frac{\cancel{n_b\,\epsilon\,\Delta\Omega}}{\cancel{n_b\,\epsilon\,\Delta\Omega}} \frac{\sigma_{\mathrm{pHe}}}{\sigma_{\mathrm{ArHe}}}. \tag{4.9}$$

This gives us a convenient ratio between the known ^{3}He–^{40}Ar Rutherford scattering cross section and the proton-^{3}He cross section:

$$\sigma_{\mathrm{pHe}} = \frac{R_c}{R_t}\,\sigma_{\mathrm{ArHe}}. \tag{4.10}$$

If we know the ratio of target atom species R_t, the ratio of proton-^{3}He counts to ^{3}He-^{40}Ar counts R_c at the same angle can give us an absolute determination of $\sigma(\theta)$ at that angle.

Using a similar argument, R_t can be measured using a proton beam, at an energy and angle where proton-^{40}Ar elastic scattering is Rutherford, and because the proton-proton cross-section can be obtained from the high-accuracy phase-shift analysis of the Nijmegen group [Ren99]. R_t can be shown to be:

$$R_t = \frac{t_{\mathrm{p}}}{t_{\mathrm{Ar}}} = \frac{N_{\mathrm{pp}}}{N_{\mathrm{pAr}}} \cdot \frac{\sigma_{\mathrm{pAr}}}{\sigma_{\mathrm{pp}}}. \tag{4.11}$$

This mixed-jet method depends on ^{3}He-^{40}Ar elastic scattering being described by the Rutherford formula. Using the DWBA code DWUCK4 [Dwu] and optical model parameters from [Bre75], it was determined that ^{3}He-^{40}Ar elastic scattering is within 5% of Rutherford out to $\theta = 40^\circ$ for the three lowest ^{3}He energies in Table 4.1. The ratio-to-Rutherford as calculated by DWUCK4 is plotted in Figure 4.6.

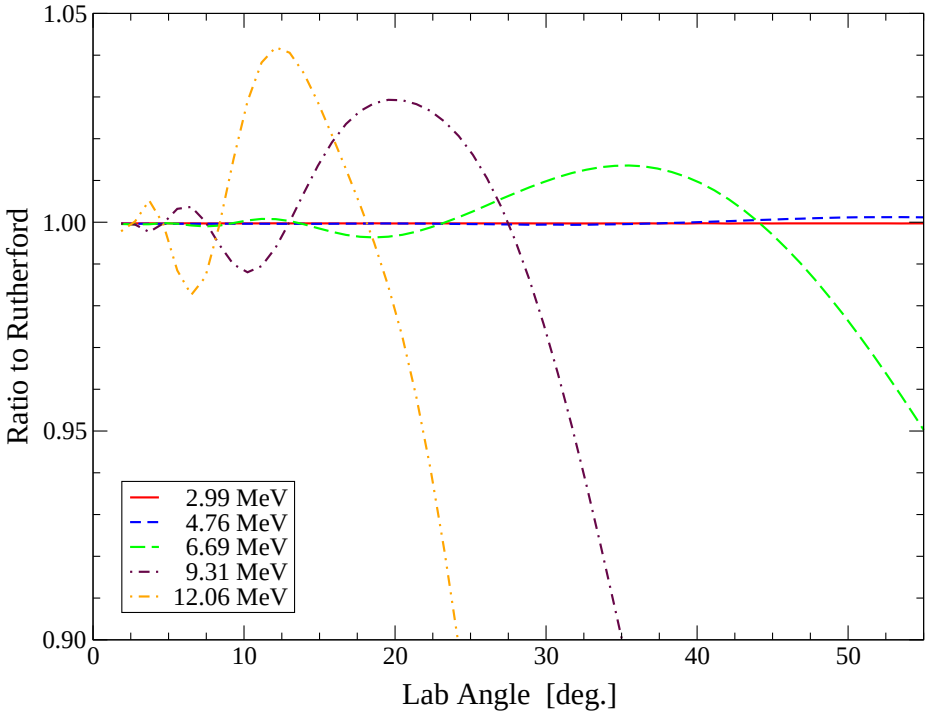

Figure 4.6: Ratio-to-Rutherford of ^{3}He-^{40}Ar elastic scattering as calculated by DWUCK4 for several different ^{3}He energies.

One of the features of this mixed-jet measurement is the total elimination of any error related to the measurement of n_b; no corrections to account for charge-exchange (as discussed in Section 3.2.6) of the beam traversing the jet are needed.

For measurements of the absolute normalization using this method, a small amount ($\sim$ 3%) of Argon was mixed with the hydrogen gas in the target jet. The gas was mixed by National Specialty Gases and the Ar/H_2 ratio was certified to be determined to an accuracy of 2% by gas chromatography. The gas mixture ratio was also verified using a proton beam at 2.24 MeV, as discussed above.

A beam of $^3He^{++}$ ions was accelerated to the desired energy and then deflected onto the gas-jet target. The elastically scattered protons and ^{3}He nuclei were detected by three pairs of silicon detectors placed symmetrically about the beam direction at 10°, 20°, and 30°, or 15°, 25°, and 35° as in Figure 4.4(a). An example spectrum is shown in Figure 4.7. Several measurements were made at each energy to ensure reproducibility.

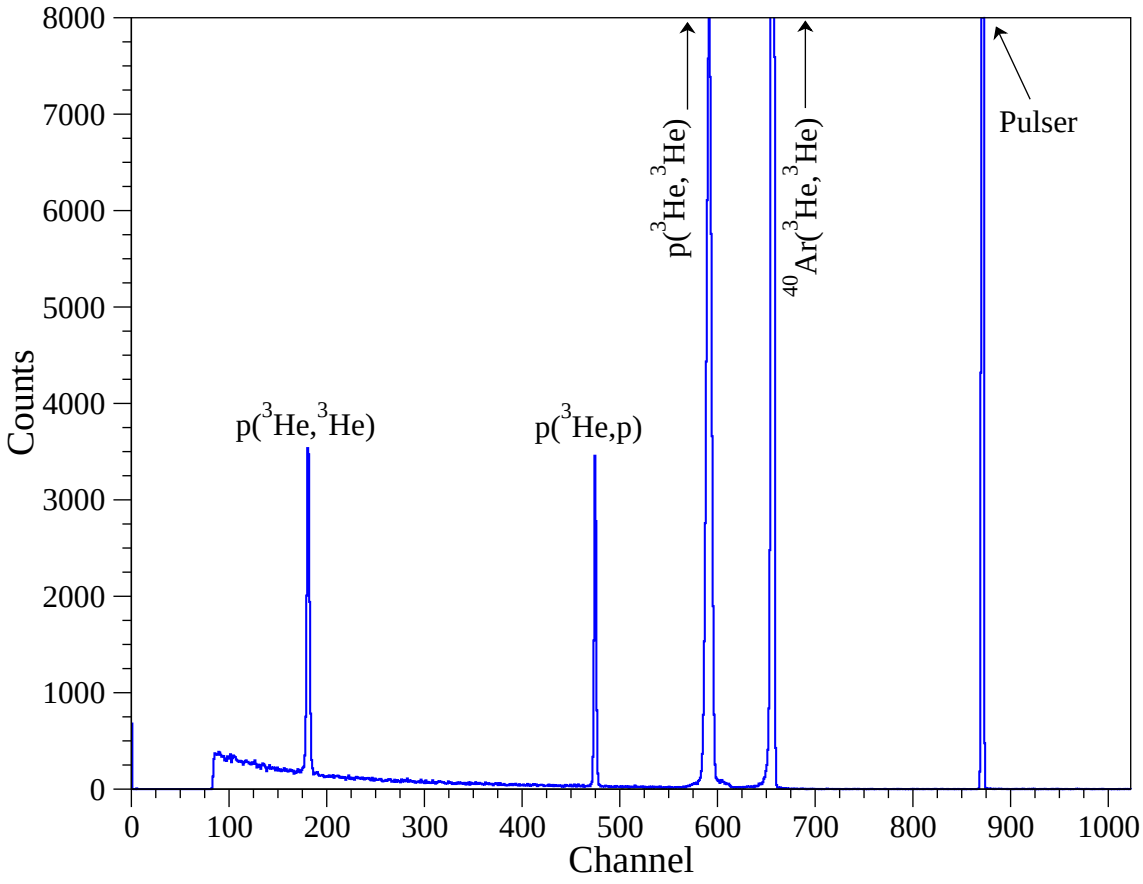

Figure 4.7: Typical spectrum of ^{3}He beam on a H_2 + Ar target. This spectrum was measured at $\theta = 10°$ at a ^{3}He beam energy of 4.79 MeV. Arrows indicate that the peaks of interest extend beyond the upper vertical scale shown.

At energies where ^{3}He-^{40}Ar elastic scattering deviates from the Rutherford scattering formula significantly, another method was used. The normalization at the higher energy was "bootstrapped" from one at a lower energy by determining the product of ^{40}Ar target thickness and detector solid angle at the lower energy, combined with the measured value of R_t,

$$(t_p \Delta\Omega) = \frac{N_{\mathrm{HeAr}}}{\sigma_{\mathrm{HeAr}}\ n_b^{(\mathrm{low})}} \cdot R_t, \tag{4.12}$$

and then using that value of $(t_p \Delta\Omega)$ to determine the absolute cross section at the higher energy,

$$\sigma_{\mathrm{pHe}}(\theta) = \frac{N_{\mathrm{pHe}}}{(t_p \Delta\Omega)\ n_b^{(\mathrm{high})}}. \tag{4.13}$$

This method does depend on accurate measurements of n_b at both energies. Corrections to account for charge-exchange of the beam through the jet (as discussed in Section 3.2.6) do need to be applied at both energies. The accuracy of this method also depends on the jet properties' not changing while changing energies. This procedure was repeated several times, switching between 4.79 MeV, and 9.36 and 12.11 MeV to ensure reproducibility.

4.4.5 Absolute Normalization – Beam Switching

Absolute normalizations have also been performed via a beam-switching method, in which the product $(t_p \Delta\Omega)$ was determined using a proton beam,

$$(t_p \Delta\Omega) = \frac{N_{\mathrm{pp}}}{\sigma_{\mathrm{pp}}\ n_b^{(\mathrm{p})}}. \tag{4.14}$$

Then, using that value of $(t_p \Delta\Omega)$, the absolute cross section at the proper ^{3}He beam energy was determined by

$$\sigma_{\mathrm{pHe}} = \frac{N_{\mathrm{pHe}}}{(t_p \Delta\Omega)\ n_b^{(^3\mathrm{He})}}. \tag{4.15}$$

For the energies indicated in Table 4.1 at which this method was used, a ^{3}He beam was first tuned onto the hydrogen jet target; this was followed by a proton beam with the same magnetic rigidity, as listed in Table 4.5. The source inflection magnet before the tandem accelerator and the accelerator terminal potential were adjusted so that

Table 4.5: Summary of absolute normalization experiments and the methods used.

$^3He^{++}$ Energy (MeV)	H_2 + Ar Mixed Gas	Proton – ^{3}He Beam Switching	Proton Energy (MeV)
2.97	✓[a]	✓	2.22
4.76	✓[a]		
6.67	✓[a]	✓	5.00
9.31	✓[b]	✓	6.96
12.06	✓[b]		

[a] Mixed-jet method.

[b] "Bootstrap" mixed-jet method (see Section 4.4.4.)

both beams passed into the chamber with the same beam tune. For each beam, the final steerer before the chamber was used to maximize the beam through the rear slit. Otherwise, the beam-transport settings were untouched to keep the beam-target geometry the same for each beam.

Detectors were placed in the chamber at 25°, 35°, and 45°, to detect scattered particles from each beam. At these angles, the proton-proton cross section does not change significantly with angle. This procedure was repeated several times to ensure reproducibility. This method depends on accurate measurements of $n_b^{(\mathrm{p})}$ and $n_b^{(^3\mathrm{He})}$ at all energies. Corrections to account for charge-exchange of the beam through the jet were applied.

The analysis of these data is described in Chapter 5, including the final error budgets for each energy.

4.5 The Proton Analyzing Power A_y

4.5.1 Formalism and Definitions

For a spin-$\frac{1}{2}$ proton beam, we can say the beam is "polarized" if there are unequal populations of particles in each of the two magnetic sub-states m_S, where "spin up" is

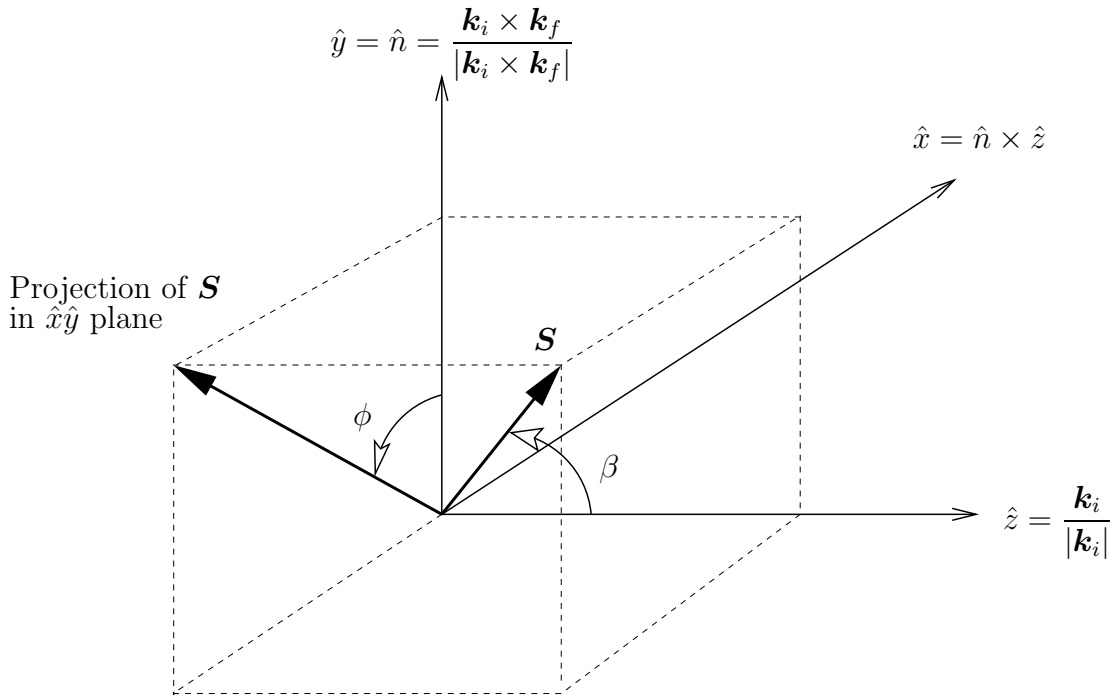

Figure 4.8: Definition of the Madison Convention. (Adapted from Fig. 1 in [Ohl73].)

$m_S = +\frac{1}{2}$ and "spin down" is $m_S = -\frac{1}{2}$. We can define p_Z as a measure of the beam's polarization

$$p_Z = \frac{N_+ - N_-}{N_+ + N_-}, \tag{4.16}$$

where N_+ and N_- are the number of spin-up and spin-down protons in the beam, respectively. An unpolarized beam, therefore, would have $p_Z = 0$.

The Madison Convention [Mad71], which defines the coordinate system describing the scattering, is used to give a consistent definition of analyzing powers and other polarization observables. A diagram depicting the convention is shown in Figure 4.8. The incoming beam momentum $\boldsymbol{k}_i$ is defined to be along the $\hat{z}$ direction. The $\hat{y}$-axis is defined to be normal to the scattering plane such that $\hat{y} = \hat{n} = \frac{\boldsymbol{k}_i \times \boldsymbol{k}_f}{|\boldsymbol{k}_i \times \boldsymbol{k}_f|}$. The $\hat{x}$-axis is then chosen to make a right-handed coordinate system ($\hat{x} = \hat{y} \times \hat{z}$). Since we are interested in elastic scattering, $|k|^2 = |\boldsymbol{k}_i|^2 = |\boldsymbol{k}_f|^2$, and, of course, the scattering angle is defined to be $\theta = \cos^{-1}(\hat{\boldsymbol{k}_i} \cdot \hat{\boldsymbol{k}_f})$.

The orientation of the spin quantization axis $\boldsymbol{S}$ is described by two angles β and ϕ; β is the angle between $\boldsymbol{S}$ and the $\hat{z}$-axis (the incident beam direction), while ϕ is

the angle between the projection of $\boldsymbol{S}$ in the $\hat{x}\hat{y}$-plane and the $\hat{y}$-axis. ϕ is defined to be always positive and increasing, as shown in Figure 4.8.

Using this convention, an expression for the yield of particles detected at a specific scattering angle θ, with the spin-quantization axis determined by (β, ϕ) is [Ohl73]

$$I(\theta, \beta, \phi) = I_0(\theta)\Big\{1 + p_Z A_y \sin\beta \cos\phi\Big\} \tag{4.17}$$

where $I_0(\theta)$ is the yield in the detector at θ if the beam were unpolarized, with $p_Z = 0$, as in Section 4.4.

If we prepare the polarized beam with $p_Z \neq 0$ such that $\beta = 90°$ ($\boldsymbol{S}$ is perpendicular to the scattering plane), Equation 4.17 can be written for two different values for ϕ

$$\begin{aligned} L = \quad I(\theta, 90°, 0°) &= I_o(\theta)\Big\{1 + p_Z A_y(\theta)\Big\} \\ R = I(\theta, 90°, 180°) &= I_o(\theta)\Big\{1 - p_Z A_y(\theta)\Big\}. \end{aligned} \tag{4.18}$$

where a detector on the left side of the incident beam gives $\phi = 0°$, and a detector on the right $\phi = 180°$. So, obviously, if one knows the beam polarization, and the ratio of polarized to unpolarized yields in either the left or right detector, A_y can be determined.

Rather than measure ratios of a polarized state to an unpolarized one, a technique using two different polarized states can be used. The second polarization state (or state 2) is a beam with a large negative p_Z, denoted by $p_Z^{(2)} < 0$ and the third state (or state 3) is a beam with a large positive p_Z, so that $p_Z^{(3)} > 0$. Using this three spin-state convention, we form ratios between the two polarized states, rather than forming ratios between polarized and unpolarized states, avoiding state 1 altogether.

When ratios of state 2 and state 3 yields are made for left and right detectors, equation 4.18 gives

$$\begin{aligned} l \equiv \frac{L^{(2)}}{L^{(3)}} &= \frac{1 + p_Z^{(2)} A_y(\theta)}{1 + p_Z^{(3)} A_y(\theta)} \\ r \equiv \frac{R^{(2)}}{R^{(3)}} &= \frac{1 - p_Z^{(2)} A_y(\theta)}{1 - p_Z^{(3)} A_y(\theta)}, \end{aligned} \tag{4.19}$$

In both cases we can solve for A_y giving

$$\begin{aligned} A_y(\theta) &= \frac{l-1}{p_Z^{(2)} - l p_Z^{(3)}} \\ A_y(\theta) &= -\frac{(r-1)}{p_Z^{(2)} - r p_Z^{(3)}}. \end{aligned} \tag{4.20}$$

With this three-spin state method, an alternative form from $p_Z^{(2)}$ and $p_Z^{(3)}$ to measure the beam's polarization is

$$\begin{aligned} \overline{p}_z &\equiv \frac{p_Z^{(3)} - p_Z^{(2)}}{2} \\ \delta p_Z &\equiv \frac{p_Z^{(2)} + p_Z^{(3)}}{2} \end{aligned} \tag{4.21}$$

allowing us to determine A_y from $\overline{p}_z$ and δp_Z as

$$\begin{aligned} A_y &= \frac{(r-1)(l-1)}{\overline{p}_z(l-r)} \\ A_y &= \frac{rl-1}{\delta p_Z(r-l)}. \end{aligned} \tag{4.22}$$

For the A_y measurements in this project, δp_Z as a beam polarization measure was not used. Since the ABPIS arranges the beam such that $p_Z^{(2)} \approx -p_Z^{(3)}$, δp_Z is close to zero, making a statistically significant measurement difficult. Therefore, $\overline{p}_z$ was used to calculate A_y in this work.

4.5.2 Measurements

For these measurements of A_y, the Atomic Beam Polarized Ion Source (ABPIS) [Cle95] has been configured to produce three spin states. As was mentioned above, laboratory convention defines state 1 as the unpolarized state, state 2 has $p_Z < 0$ and state 3 has $p_Z > 0$. This three-state system, in general, allows for fast switching between the states to help eliminate systematic errors. The eight-step sequence for spin-state switching $+ \circ - \circ - \circ + \circ - \circ + \circ + \circ - \circ$, (where $\circ$ designates state 1, $-$ designates state 2, and $+$ designates state 3) is chosen to minimize both linear and quadratic drifts in the data related to changes in target thickness or gain-shifts in detector electronics [Set95]. In this work, the spin-state of the source was switched every

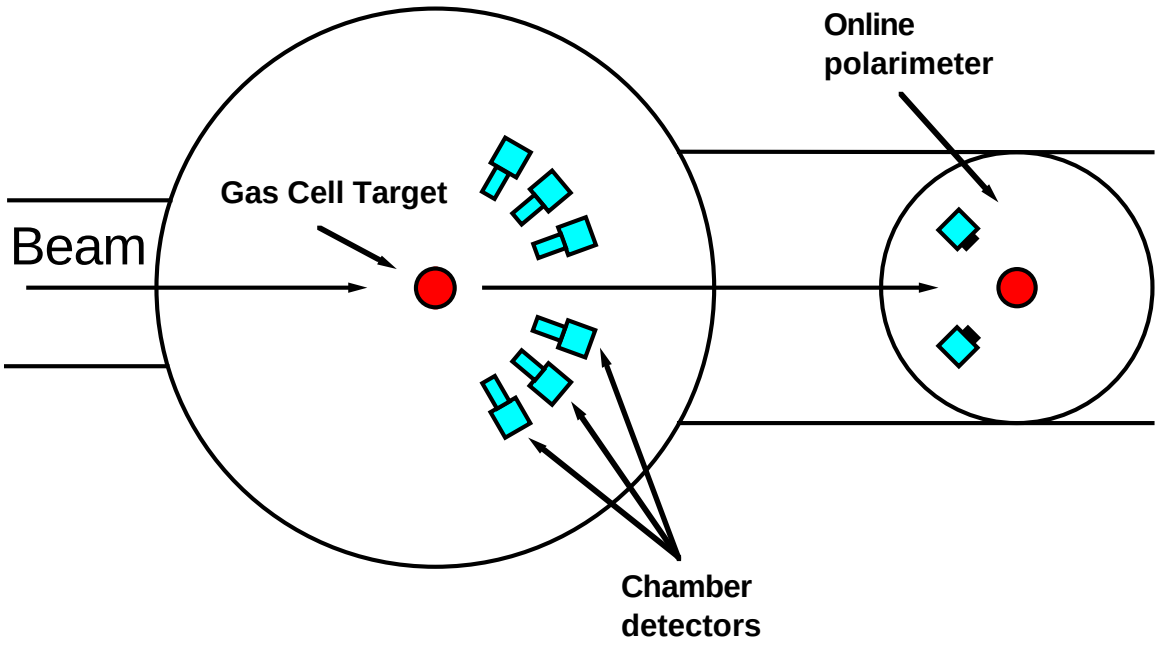

Figure 4.9: Chamber setup for A_y measurements.

300 ms. During measurements, the time spent in state 1 was significantly reduced since that state does not contribute to our measurement of A_y. This "unpolarized state" has a measurable polarization ($\approx 10\%$) because of unequal focusing of the atomic beam in the sextupoles [Men96]. The atoms with electron spin-up are more strongly focused inside a sextupole than those with spin-down [Hab67]. However, during initial tuning of the polarized beam, it becomes useful to increase the time spent in state 1 to the full 0.3 s to compare the values of the polarization measured in the polarimeter at the end of the beamline to those measured at the ABPIS with the spin-filter polarimeter [Men96], which gives polarization values in terms of $p_Z^{(2)}$ and $p_Z^{(3)}$. The electronics used control the spin-state of the ABPIS can be found in [Gei98].

The polarized proton beam from the ABPIS was accelerated to the desired energy with the FN tandem accelerator and tuned onto a gas-cell target inside the 62-cm scattering chamber, as shown in Fig. 4.9. The gas-cell, covered with 2.3-μm Havar foil, was filled with 1 atm of ^{3}He gas, and was mounted on the target-rod which was supported from the top of the chamber. This allowed the cell to be raised out of the way of the incident beam allowing the beam enter the polarimeter directly.

Table 4.6: Results of TRIM energy loss calculations for A_y measurements with a 1 atm ^{3}He gas-cell target. The first column is the incident beam energy, the second column gives the energy of the beam after it passes through the 2.3-μm Havar foil, and the third column is the beam energy at the center of the cell, after losing energy through 12.7 mm of 1 atm ^{3}He gas. All energies are in MeV. A discussion of the error bars is given in the text.

Beam Energy	Havar Energy	Cell Center
1.805	1.633	1.601 ± 0.018
2.440	2.298	2.271 ± 0.014
3.270	3.152	3.130 ± 0.012
4.181	4.080	4.060 ± 0.010

Since there is significant energy loss (especially at these low energies) in the cell foil, the incident beam energy had to be increased so that the beam reached the desired energy at the cell center. The energy losses in the cell foil and ^{3}He gas were modeled by the computer code TRIM[7], which is a Monte-Carlo code which can be used to determine the energy loss of ions passing through matter [Zie85]. Table 4.6 shows the results of these energy loss calculations. The accelerator beam energy was set to the value in the "Beam Energy" column to reach the desired energy at the center of the gas cell, as listed in the 'Cell Center" column. The errors quoted are calculated by adding in quadrature the 5 keV uncertainty in the beam energy from the magnet calibration [Fis97a], and assuming a 10% uncertainty for each of the the energy losses through the Havar foil and the ^{3}He gas.

The elastically scattered protons were detected with three pairs of silicon detectors placed symmetrically about the beam direction. This setup allowed measurements of A_y to be made from $\theta_{\rm lab} = 20^\circ$ to 160°. Measurements at angles smaller than 20° were not possible because of very large backgrounds from "foil-foil" scattering, and direct scattering of the beam from the entrance foil. Measurements at angles greater than 160° were not possible because of the very low energies of the scattered protons; they

[7]TRIM has been subsequently renamed SRIM, for The **S**topping and **R**ange of **I**ons in **M**atter.

experience too much energy loss exiting the Havar foil. In fact, at the lowest energy 1.6 MeV, scattered protons could not be observed at angles greater than 90°.

Measurements of A_y were taken at 5° increments over the allowed angular range. The dimensions of the collimators placed in front of the detectors, along with the distances the detectors were placed from the target-cell center are listed in Table 4.7. All the detectors used in the A_y measurements were 300 μm thick, and each pair was spaced at 15° intervals. The detector electronics are shown in in Fig. 4.1. The magnitude of A_y through these measurements ranged from 0.04 to 0.4; to reach the desired statistical accuracy on A_y, about 1.5×10^6 total counts were needed for each angle setting.

Three spin-state routing signals were sent from the spin-state switching electronics to the ADCs indicating to the data acquisition system the polarization state the of ABPIS. A histogram for each spin state and a summed histogram were accumulated in separate data areas depending on the spin-state of the polarized beam, indicated by these three spin-state routing signals. In this way, ratios of counts in each spin state could easily be calculated. A typical spectrum showing the three spin-state spectra, and the summed spectra superimposed, is shown in in Fig. 4.10.

The polarization of the proton beam was monitored on-line with a polarimeter based on ^{4}He($\vec{\text{p}}$,p)^{4}He elastic scattering [Leo98]. Also periodically during the experimental runs, the beam energy was raised either to 6 MeV or 8 MeV, where the analyzing power for the polarimeter is very close to unity. This was done once every two to three hours. Also, when measuring the beam's polarization at the lowest energies the ^{3}He target was raised out of the way, allowing the beam to pass directly into the polarimeter.

The analysis of these data is described in Chapter 5, including a discussion of the propagation of errors.

Table 4.7: Detector and collimator setups for A_y measurements. All detectors were 300 μm thick. The front and back collimators for each detector were the same dimensions, as listed. The distance from the target center to the detector face, and the length of the detector snout is also listed. The detector pairs were spaced at 15° intervals.

	R1 & L1			R2 & L2			R3 & L3		
Energy (MeV)	Collimation H × V (mm)	Distance (cm)	Snout (cm)	Collimation H × V (mm)	Distance (cm)	Snout (cm)	Collimation H × V (mm)	Distance (cm)	Snout (cm)
1.60	1.6 × 9.5	12	6.4	1.6 × 9.5	12	5.1	2.4 × 9.5	14	5.1
2.25	1.6 × 9.5	10.2	5.1	1.6 × 9.5	12	5.1	2.4 × 9.5	14	5.1
3.13	1.6 × 9.5	10.2	5.1	1.6 × 9.5	12	5.1	2.4 × 9.5	14	5.1
4.05	1.6 × 9.5	10.2	5.1	1.6 × 9.5	12	5.1	2.4 × 9.5	14	5.1

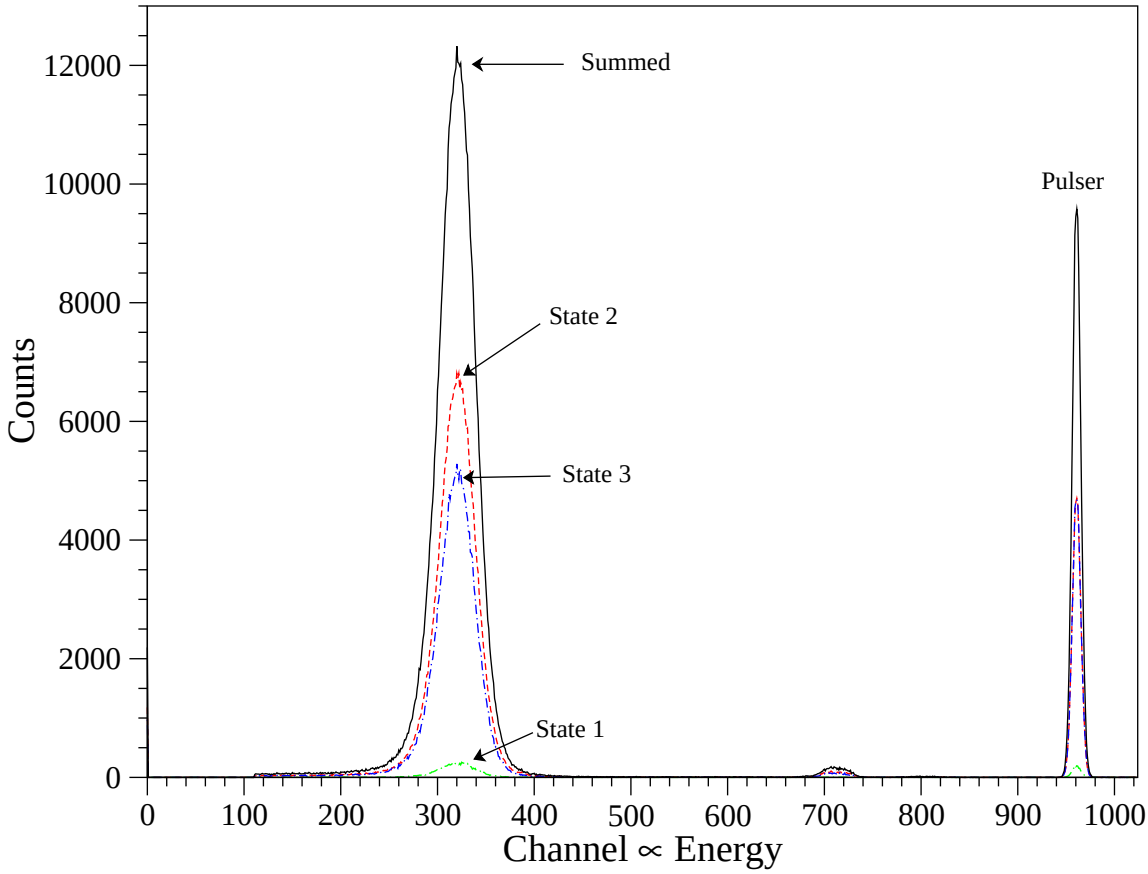

Figure 4.10: Typical spectrum from an A_y measurement. This spectrum was taken at $E_p = 3.13$ MeV with a detector at $\theta = 90°$. The time the source spent in state 1 was greatly reduced, as indicated by the rather small state 1 peak shown. The time the source spent in states 2 and 3 is nearly equal, as indicated by the state 2 and state 3 pulser peaks' being on top of one another. The peak near channel 720 is caused by residual air in the gas cell.

Chapter 5

Data Analysis

Once raw spectra for both the $\sigma(\theta)$ and A_y experiments were collected (as documented in Chapter 4), the data were processed to extract experimental values for the observables. This chapter describes that procedure, and the errors in the final results.

5.1 Peak Extraction

For both the $\sigma(\theta)$ and A_y measurements, the XSYS display and analysis software package were utilized to subtract background under the peaks and then sum the counts in the peaks. Originally written for VAX computers in Fortran, most of the routines have been rewritten in C and ported to a more modern Linux-based system [Can00]. This allowed the use of analysis scripts with more modern UNIX shell commands and the scripting language Perl.

The determination of the error in the measured observables from the uncertainties in the peak areas employed the standard propagation of error formula [Bev92]. If f is a function of n independently measurable quantities i, the error in f is

$$[\Delta f]^2 = \sum_i^n \left(\frac{\partial f}{\partial i} \Delta_i \right)^2 + \sum_i^n \sum_{j>i}^n \rho(j,i) \frac{\partial f}{\partial i} \frac{\partial f}{\partial j} \tag{5.1}$$

where Δ_i is the error in the ith variable, and $\rho(j,i)$ is the correlation coefficient between variables i and j. In this work the correlation coefficients were not calculated and are

assumed to be small. Therefore, the simplified version of Equation 5.1

$$[\Delta f]^2 = \sum_i^n \left(\frac{\partial f}{\partial i} \Delta_i \right)^2 \tag{5.2}$$

was used for error propagation for both $\sigma(\theta)$ and A_y measurements.

After defining the peaks of interest, a gate was set around each peak and its background, if present. The background counts under the peak were determined by fitting the background on either side with a linear or exponential function. With this information, both the total peak counts and background counts were determined. The background counts in the peak gate were subtracted from total counts in the peak gate to give the true peak sum. This information, along with the counts in a separate scaler for beam-current integration, dead-time pulser counts, and the time elapsed, were all extracted from the XSYS data file for each peak of interest. This information was then fed into other analysis codes to calculate values for the observables.

All of the peak areas determined from the XSYS software were corrected for dead-time. The dead-time correction factor is defined as

$$dtc = \frac{n_{pul}}{N_{pul}}, \tag{5.3}$$

where n_{pul} and N_{pul} are the number of pulser signals sent to the test input of the preamp (as counted by a scaler) and the pulser counts stored in the spectrum, respectively. The error in the dead-time correction Δdtc is defined to be

$$\Delta dtc = dtc \frac{\Delta N_{pul}}{N_{pul}} = dtc \frac{\sqrt{|n_{pul} - N_{pul}|}}{N_{pul}}. \tag{5.4}$$

The dead-time corrected peak area N is defined as

$$N = dtc \cdot N_{net}, \tag{5.5}$$

where N_{net} is the number of counts in the peak of interest after subtracting the background, and N_{back} is the number of background counts that were subtracted. The error ΔN of the net peak area is therefore

$$\Delta N = N \cdot \sqrt{\left(\frac{N_{net} + 2N_{back}}{N_{net}} \right)^2 + \left(\frac{|n_{pul} - N_{pul}|}{{N_{pul}}^2} \right)}. \tag{5.6}$$

5.2 The Differential Cross Section

Both the relative and absolute cross section measurements in this work were made with pairs of chamber detectors and monitor detectors arranged symmetrically about the beam direction, as discussed in Section 4.4.2. This helps minimize geometry changes arising from beam position changes.

5.2.1 Relative $\sigma(\theta)$ Measurements

We can define the monitor detector normalized yield $Y(\theta)$, which is proportional to $\sigma(\theta)$, as

$$Y(\theta) = \frac{N(\theta_R) + N(\theta_L)}{N(\theta_{RM}) + N(\theta_{LM})}, \tag{5.7}$$

where $N(\theta_R)$ and $N(\theta_L)$ are the deadtime-corrected counts in the right and left detectors, and $N(\theta_{RM})$ and $N(\theta_{LM})$ are the counts in the right and left fixed monitor detectors.

Using Equations 5.2 through 5.6, the error in the monitor-normalized yield becomes

$$\Delta Y(\theta) = Y(\theta)\left[\frac{\Delta N_R{}^2 + \Delta N_L{}^2}{(N_R + N_L)^2} + \frac{\Delta N_{RM}{}^2 + \Delta N_{LM}{}^2}{(N_{RM} + N_{LM})^2}\right]^{\frac{1}{2}}. \tag{5.8}$$

Corrections were made to the measured counts in each detector to account for differences in detector solid angles, and also to correct for the two monitor detector positions (see Section 4.4.2.) Statistical errors on these corrections were included in the final determinations of the observables.

5.2.2 Accuracy of Proton-Proton Cross Sections

As was discussed in Sections 4.4.4 and 4.4.5, both the beam-switching method and the mixed-gas method (i.e. determination of the $^{40}Ar/H_2$ gas ratio) of measuring the absolute normalization of $\sigma(\theta)$ rely on accurate determinations of the ^{1}H(p,p)^{1}H reaction at several energies between between 2 and 10 MeV. The proton-proton cross sections were calculated with the SAID program at the Center for Nuclear Studies at George Washington University [Sai03]. The accuracy of the SAID calculations, based

Table 5.1: Comparison of ^{1}H(p,p)^{1}H data with calculations of SAID. For each datum, the deviation (in percent) from the PSA value was calculated. The average values are listed below.

Data Set	E_p(MeV)	Deviation (%)
[Kne66]	2.425	0.2
[Kne66]	3.037	0.2
[Ima75]	4.978	0.9
[Ima75]	6.968	1.2
[Ima75]	8.030	1.3

on the Nijmegen nucleon-nucleon database [Sto93], have been checked by comparing SAID calculations to existing data at energies between 2.2 and 10 MeV. The experimental data considered were those of Knecht *et al.* [Kne66] at $E_p = 2.425$ and 3.037 MeV, and Imai *et al.* [Ima75] at $E_p = 4.978$, 6.968, and 8.030 MeV. These data sets have statistical errors on the $0.3 - 0.5\%$ level, and quoted systematic errors of $\approx 0.3\%$. A summary of the comparison of the data sets and SAID calculations is given in Table 5.1.

With these comparisons, a conservative error of 0.5% will be attributed to the ^{1}H(p,p)^{1}H cross sections below $E_p = 8$ MeV as determined by SAID.

At the higher energies, however, where it appears that the SAID PSA starts to deviate more from the existing database, a larger error of 2% will be used. This is only an issue when determining the $\sigma(\theta)$ normalization at a ^{3}He energy of 12.06 MeV via the beam-switching technique.

5.2.3 Absolute $\sigma(\theta)$ Normalization – Mixed Jet

For the mixed jet absolute normalization method (as described in Section 4.4.4), an accurate determination of the $^{40}Ar/H_2$ gas ratio in the target is needed. The gas ratios were determined by the manufacturer[8] by gas chromatography, and certified to

[8]National Specialty Gases, Durham, NC

Table 5.2: $^{40}Ar/H_2$ gas ratios as determined by proton-^{40}Ar Rutherford scattering and proton-proton elastic scattering. The errors listed are statistical. A 0.5% overall systematic error from the calculation of the proton-proton cross sections also is present. The proton beam energies at which the measurements were made for each bottle are also listed.

		$^{40}Ar/H_2$ Gas Ratio (%)	
Bottle	Beam Energy [MeV]	Gas Chromatography	Beam Measurement
1	2.22	3.07 ± 0.06	3.12 ± 0.02
2	3.56	2.78 ± 0.06	2.88 ± 0.04
3	3.56	3.16 ± 0.06	3.10 ± 0.02

the 2% level. However, because the gasses have different ratios of specific heats (γ), they may behave differently in the gas-jet. As a check, the ratio was measured for each bottle of mixed gas via Equation 4.11. The proton-proton cross section was calculated by SAID. The results of these measurements are listed in Table 5.2. As can be seen, there is virtually no difference between the ratio determined by the manufacturer and that measured in the gas-jet, indicating that the difference in behavior in the jet by H_2 and Argon is negligible at these operating parameters.

The 0.4% uncertainty in the beam energy, as described in Appendix B translates into a systematic error in two places in this method. The determination of the $^{40}Ar/H_2$ ratio, as described above, depends on the ^{1}H(p,p)^{1}H cross section. This cross section does not have a strong energy dependence, though at the $\approx$ 0.6% level it is not negligible. The error in the beam energy also translates into a potential error in determining the ^{40}Ar-^{3}He Rutherford cross section used in Equation 4.10.

A summary of the sources of error contributions for the mixed-gas normalizations is listed in Table 5.3.

5.2.4 Absolute $\sigma(\theta)$ Normalization – Beam Switching

The beam switching method, as described in Section 4.4.5, involves calculating the yields for proton-^{3}He elastic scattering and proton-proton elastic scattering at the

Table 5.3: Mixed-jet normalization error budget at $\theta_{lab} = 25^{\circ}$ for several of the absolute normalization measurements performed at the ^{3}He energies shown. The normalizations performed at 2.97, 4.76, and 6.69 MeV were made with the mixed-jet method, while those at 9.31 and 12.06 MeV were performed with the "boostrap" mixed jet method.

		Error (%)				
Source		2.97 MeV	4.76 MeV	6.69 MeV	9.31 MeV	12.06 MeV
Counting Statistics	(stat)	0.3	0.3	0.3	0.3	0.3
$^{40}Ar/H_2$ Ratio	(stat)	0.6	0.6	0.2	1.4	1.4
	(sys)	0.6	0.5	0.5	0.5	0.5
^{40}Ar-^{3}He $\sigma(\theta)$	(sys)	1.2	0.8	0.8	0.8	0.8
Angle Setting	(sys)	1.0	1.0	1.0	1.0	1.0
BCI Correction Factor	(sys)	—	—	—	0.6	1.3

same angle. Equation 4.15 can be rewritten as

$$\sigma_{\mathrm{pHe}} = \frac{Y_{\mathrm{pHe}}}{Y_{\mathrm{pp}}} \cdot \sigma_{\mathrm{pp}}, \tag{5.9}$$

where the Y's are the integrated beam-current normalized yields, as calculated by Equation 5.11. Therefore the error in σ_{pHe} is

$$\Delta\sigma_{\mathrm{pHe}} = \sigma_{\mathrm{pHe}} \cdot \left[\left(\frac{\Delta Y_{\mathrm{pHe}}}{Y_{\mathrm{pHe}}} \right)^2 + \left(\frac{\Delta Y_{\mathrm{pp}}}{Y_{\mathrm{pp}}} \right)^2 \right]^{\frac{1}{2}} \tag{5.10}$$

where the ΔY's are defined by Equation 5.12.

Unlike similar measurements performed using solid targets [Woo00], target degradation is not a problem with the gas-jet target. Target reproducibility, however, is an issue, though with the mass-flow controller the jet thickness has been shown to be stable within 2%, as discussed in Section 3.2.6.

The systematic errors involved in the beam-switching measurements are similar to those in the mixed-gas method. The 0.4% error in the beam energy has some effect on the energy at which the proton-proton cross-section is calculated. Any charge-exchange effects of both beams through the jet needs to be taken into account as well. A summary of the sources of error contributions for the beam-switching normalizations is listed in Table 5.4.

5.3 Analyzing Powers

All of the A_y measurements in this work were made using the two-state method, as described in Section 4.5.1. This section describes the analysis of those data.

5.3.1 Errors in A_y

The analysis of the A_y measurements is often much simpler than that of the $\sigma(\theta)$ measurements, since many of the factors in Equation 4.7 cancel out. For the analyzing power measurements, the peak counts in each spin state i were normalized to the

Table 5.4: Beam-switching normalization error budgets for $\theta = 25°$.

		Error (%)		
Source		2.97 MeV	6.69 MeV	9.31 MeV
Counting Statistics	(stat)	0.4	0.4	0.4
proton-proton $\sigma(E,\theta)$	(sys)	0.5	0.7	1.0
BCI Correction Factor	(sys)	1.3	1.0	0.5
Beam Energy	(sys)	< 0.1	< 0.1	< 0.1
Angle Setting	(sys)	< 0.1	< 0.1	< 0.1
Jet Reproducibility	(sys)	5.0*	0.8	1.0

* statistics limited

integrated beam current in that state. The integrated beam-current normalized yield of counts detected from beam polarization state i is defined as

$$Y^{(i)} = \frac{N_{net}^{(i)}}{n_b^{(i)}} \cdot dtc^{(i)}, \tag{5.11}$$

where $N^{(i)}$ indicates the net counts in the peak of interest, $n_b^{(i)}$ is the number of beam particles in state i that traversed the target, and $dtc^{(i)}$ is the dead-time correction in state i, as defined in Equation 5.3. The error in $Y^{(i)}$ is defined similarly to Equation 5.6,

$$\Delta Y^{(i)} = Y^{(i)} \cdot \sqrt{\left(\frac{N_{net}^{(i)} + 2N_{back}^{(i)}}{N_{net}^{(i)}}\right)^2 + \left(\frac{|n_{pul}^{(i)} - N_{pul}^{(i)}|}{{N_{pul}^{(i)}}^2}\right)}. \tag{5.12}$$

For the A_y measurements, as was discussed in Section 4.5.1, we are interested in the ratio $\mathsf{r} = Y^{(2)}/Y^{(3)}$, where r represents either r or l, the state-2 to state-3 ratio for the right or left detector, as defined in Equation 4.19. The error in r is

$$\Delta\mathsf{r} = \mathsf{r} \cdot \sqrt{\left(\frac{\Delta Y^{(2)}}{Y^{(2)}}\right)^2 + \left(\frac{\Delta Y^{(3)}}{Y^{(3)}}\right)^2}. \tag{5.13}$$

The error in A_y is therefore

$$\Delta A_y = |\overline{p}_z A_y| \left\{ {A_y}^2 \left[\frac{\Delta r}{(r-1)^2}\right]^2 + {A_y}^2 \left[\frac{\Delta l}{(l-1)^2}\right]^2 + \left[\frac{\Delta \overline{p}_z}{{\overline{p}_z}^2}\right]^2 \right\}^{\frac{1}{2}}. \tag{5.14}$$

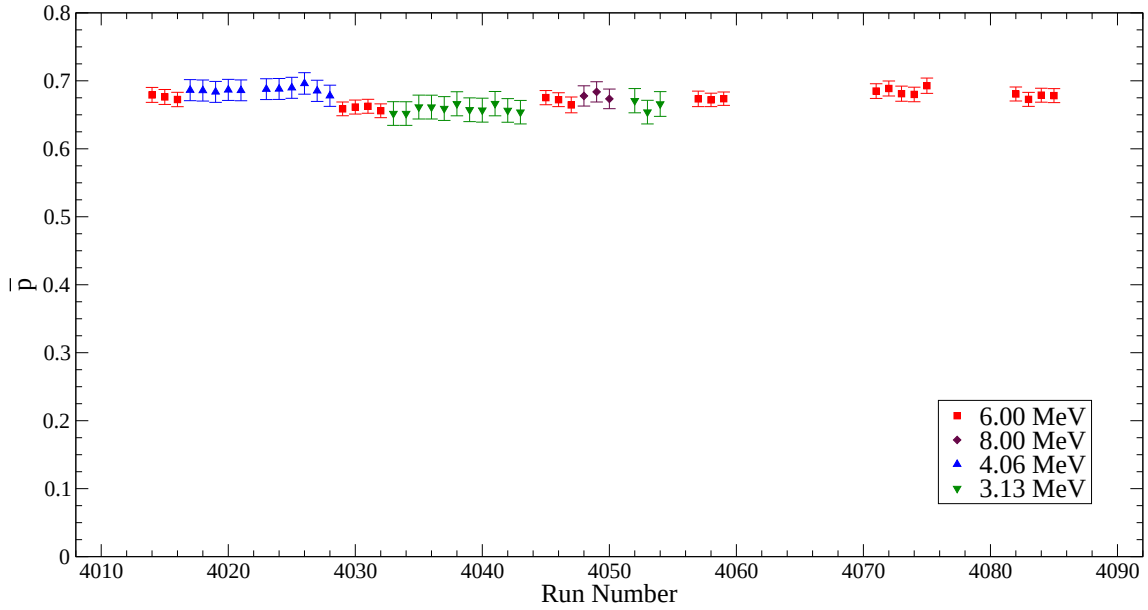

Figure 5.1: Beam polarization measurements during A_y measurements at 4.06, 3.13, and 2.27 MeV. The ^{4}He(p,p)^{4}He polarimeter has been calibrated at all of these energies [Leo98].

5.3.2 Polarimetry

For the polarimeter the known quantity is A_y and the observable is $\overline{p}_z$,

$$\overline{p}_z = \frac{(r-1)(l-1)}{A_y(r-l)}, \tag{5.15}$$

the reverse of the measurement taking place in the chamber. The error in $\overline{p}_z$ is therefore

$$\Delta\overline{p}_z = |A_y\overline{p}_z| \left\{ \overline{p}_z{}^2 \left[\frac{\Delta r}{(r-1)^2}\right]^2 + \overline{p}_z{}^2 \left[\frac{\Delta l}{(l-1)^2}\right]^2 + \left[\frac{\Delta A_y}{A_y{}^2}\right]^2 \right\}^{\frac{1}{2}}, \tag{5.16}$$

where r, l, and A_y refer to polarimeter quantities in this case.

The results of the beam polarimetry measurements used for A_y measurements made at 4.06, 3.13, and 2.27 MeV are shown in Figure 5.1, and at 1.6 MeV in Figure 5.2. During the measurement at 1.60 MeV, significant difficulty was experienced in keeping the ABPIS beam polarization high, as seen in the scatter in $\overline{p}_z$ values in Figure 5.2. The runs indicated by the boxes in Figure 5.2 were considered "good", and the beam energy was then lowered for A_y measurements. The beam polarization was checked frequently, and if there was significant deviation, adjustments were made

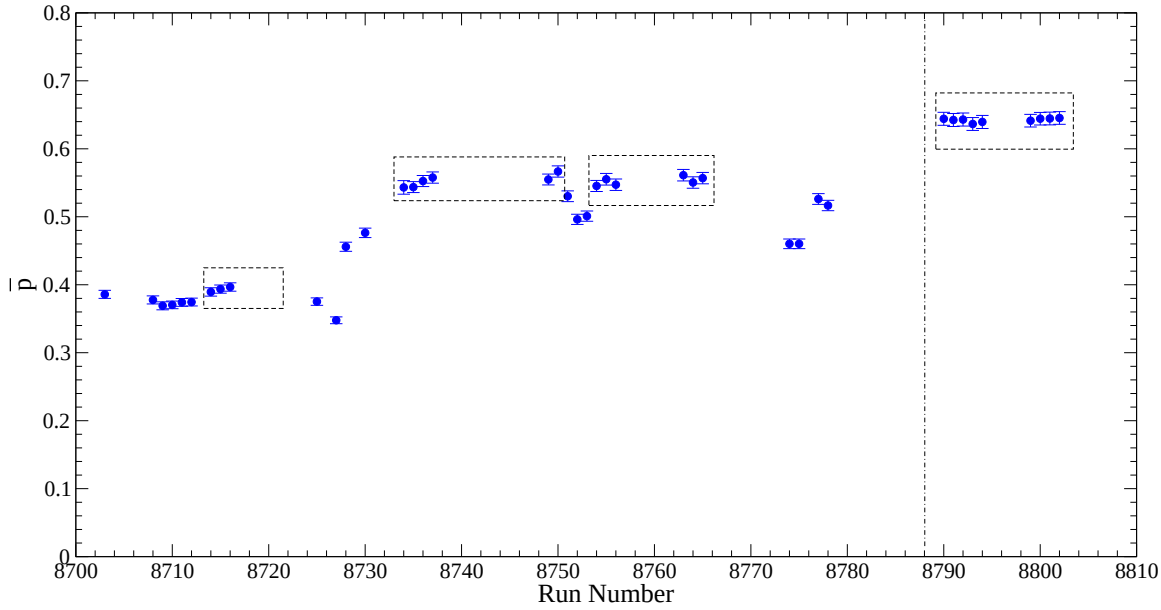

Figure 5.2: Beam polarization measurements during A_y measurements at 1.6 MeV. The measurements were made at $E_p = 6.0$ MeV, where A_y for the ^{4}He(p,p)^{4}He polarimeter is nearly unity. These measurements were made with the chamber gas-cell raised, so the beam went directly into the polarimeter. The runs to the right of the vertical dot-dash line were taken the following day after significant polarized source maintenance.

at the polarized ion source. The runs to the right of the vertical dot-dash line were taken the following day after significant source maintenance.

Chapter 6

Results

With the completion of the cross section and proton analyzing power measurements, comparisons with previous data taken at the same energies, and comparisons with the theoretical predictions of the Pisa Group are possible – from both a more qualitative "visual" inspection to a more quantitative χ^2 analysis. In general, the new data set offers two very good features over data sets previously measured: higher precision and a greater number of points.

The comparison of the data to the theoretical predictions is very much a work-in-progress, however, as the techniques for solving scattering problems in the $4N$ system are constantly evolving. In fact, Viviani of the Pisa Group is currently rewriting the code and new results are forthcoming [Viv03]. The theoretical calculations presented in this Chapter are older and were obtained from both the literature [Viv01] and by the author during a visit to Pisa[9] during the summer of 2002 [Viv02].

6.1 Comparisons with Previous Data

As a check of their accuracy, the new data measured in this work can be compared to previous data measured at the same (or nearly the same) energy.

Previous measurements of the differential cross section at similar energies are at $E_{\rm p} = 1.0$ MeV [Ber80, Fam54], at $E_{\rm p} = 1.6$ and 2.25 MeV [Fam54], and 4.0 MeV

[9]No, I did not go up the Leaning Tower.

[McD64]. Plots of the new data with those of previous work are shown in Figures 6.1 and 6.2.

In general, the agreement is quite good; there is a marked improvement in the size of the error bars, and the new data sets contain many more data points. The precision of the new data is much better than that of Famularo *et al.*, and is comparable to that of Berg *et al.*. In both the 1.60 and 2.25 MeV data sets, the new data do seem to have a slightly deeper minimum at $\theta_{\mathrm{c.m.}} = 80^\circ - 100^\circ$ than the data of Famularo. This could be because of a smaller angular acceptance in the present experimental setup than in the one of [Fam54]. However, this cannot be confirmed since a detailed description of the Famularo experiment does not exist in the literature. In the 4 MeV case, there is good agreement between the current data and those of [McD64], but with slightly smaller error bars. The data of McDonald *et al.* allow a more precise mapping of the interesting feature around $\theta_{\mathrm{c.m.}} = 30^\circ$. No $\sigma(\theta)$ data near $E_{\mathrm{p}} = 3.11$ MeV could be found in the literature with which to compare the new data.

The previous measurements of the proton analyzing power A_y that overlap those made for this work are at $E_{\mathrm{p}} = 1.6$ and 2.25 MeV [Viv01], 3.13 MeV [Det79] and 4.0 MeV [All93a]. Plots of the new data with those of previous work are shown in Figure 6.3. As can be seen, there is significant improvement in the precision in the A_y measurements at 1.6, 2.25, and 3.13 MeV. There is also a noticeable increase in the density of points, and the scatter seen in the [Viv01] data has vanished.

6.2 Comparisons with Theoretical Predictions

As was stated above, the "machinery" for calculating observables from realistic potential models is still new and developing quickly. They are the results of calculations using the Argonne v_{18} (AV18) NN potential alone, and others including the Urbana IX (UR-IX) $3N$ interaction. Newer predictions from the Pisa Group are forthcoming [Viv03], which have quicker convergence than earlier calculations when many P-wave channels had to be included, making the calculations time-consuming. Because of this delay, predictions including the UR-IX interaction at the two highest energies are not

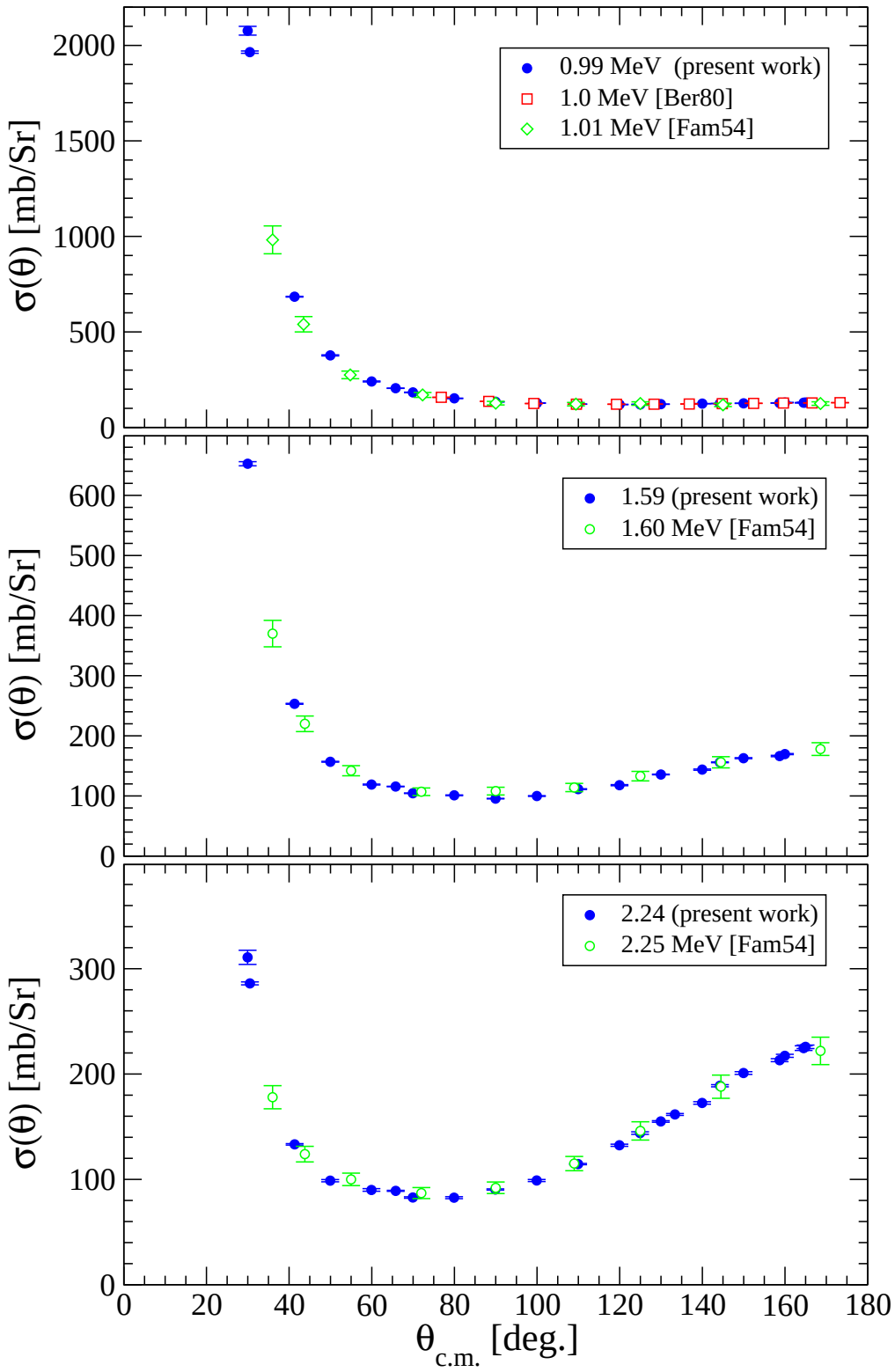

Figure 6.1: New $\sigma(\theta)$ results at E_{p}= 0.99, 1.60, and 2.25 MeV with the data of Famularo *et al.* [Fam54] and Berg *et al.* [Ber80].

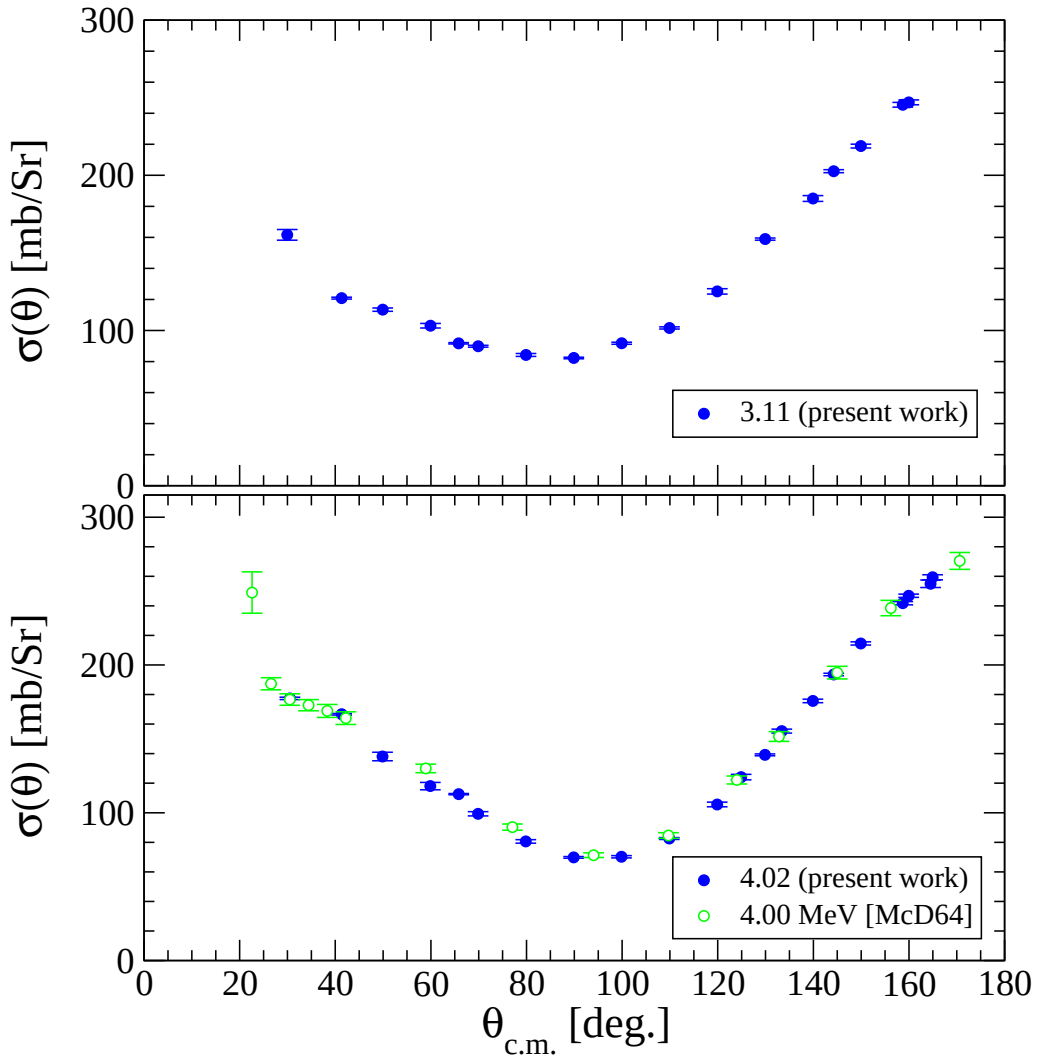

Figure 6.2: New $\sigma(\theta)$ results at E_{p}= 3.11 and 4.02 MeV with the data of McDonald *et al.* [McD64].

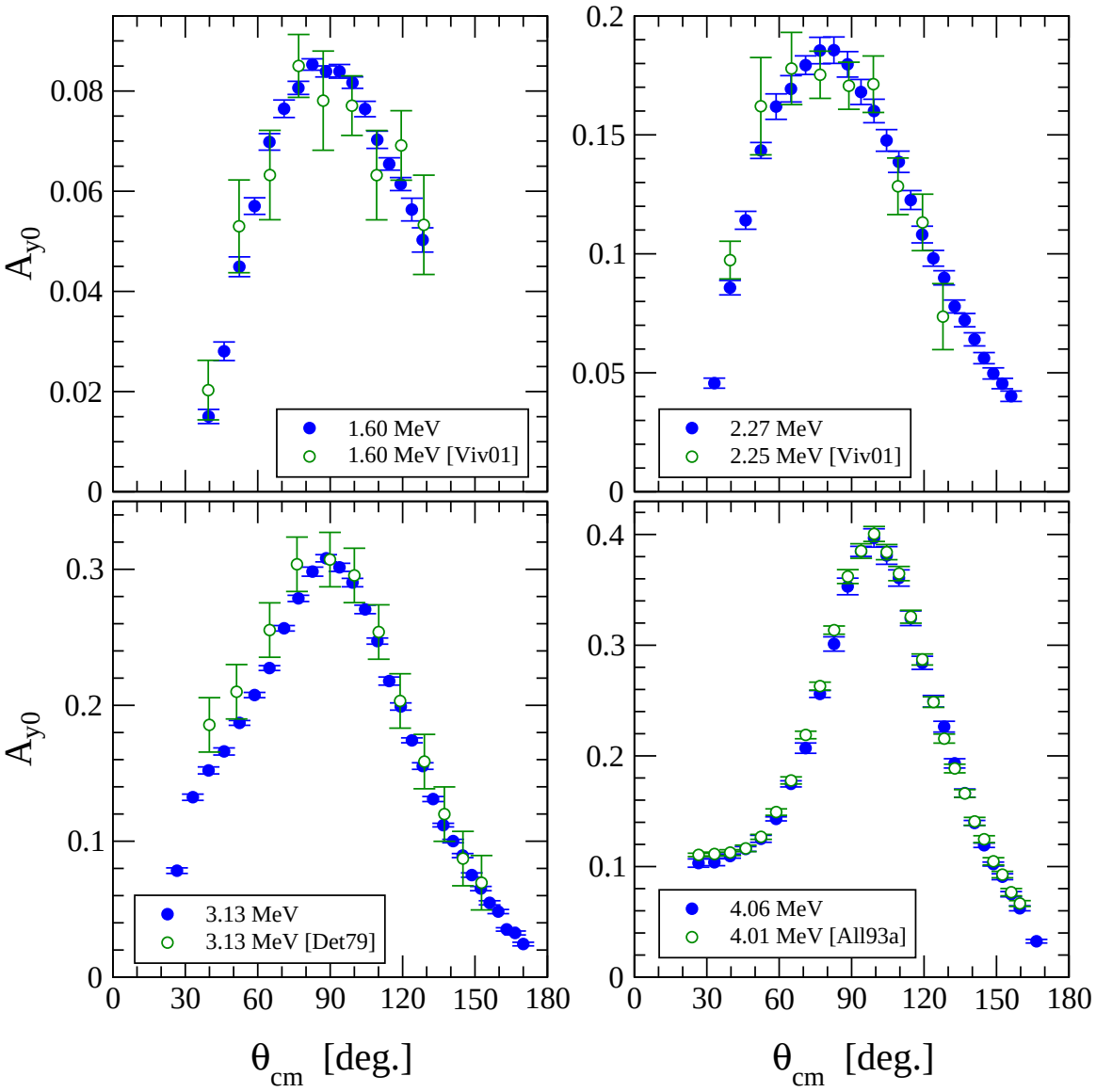

Figure 6.3: New A_y results at E_p= 1.6, 2.27, 3.13, and 4.06 MeV with the data of [Det79], [All93a], and [Viv01].

yet available.

6.2.1 Differential Cross-Section $\sigma(\theta)$

Plots of the current data set along with the Pisa Group predictions are shown in Figures 6.4 and 6.5. As can be seen, the agreement between theory and experiment, while not horrible, is not perfect. In general, the calculations describe the minimum of the cross-section well, and, in the case of the two lowest energies in Figure 6.4, the addition of the UR-IX $3N$ interaction improves the description of this minimum. This is not too surprising, as the three-nucleon interaction correctly binds the ^{3}He, effectively making it smaller and hence decreasing the cross-section.

However, at backward angles there is a discrepancy between the data and the calculations in most of the distributions. Most of the data lie several standard deviations above the theoretical curves at $\theta_{\text{c.m.}} > 140°$. In the 1.6 and 2.25 MeV cases, the addition of the three-nucleon interaction moves the theoretical prediction away from the data.

The data points are tabulated in Appendix C.

6.2.2 Proton Analyzing Power A_y

The results for A_y are shown in Figures 6.6 and 6.7, including the predictions of the Pisa Group. As is quite apparent, the "A_y Puzzle" is present at all 4 energies at which data were taken. The theoretical predictions fail to describe the data rather spectacularly. Interestingly, in the 1.6 and 2.27 MeV calculations, the addition of the UR-IX three-nucleon interaction has nearly zero effect on the A_y predictions. It will be interesting to see if this trend holds for the higher two energies once the calculations become available [Viv03].

The energy dependence of the discrepancy is plotted in Figure 6.8. A 8th-order associated Legendre function was fitted to each of the A_y distributions to determine the peak value of A_y in the angular distribution. That experimental value was then subtracted from the theoretical prediction at the same angle, and then the difference

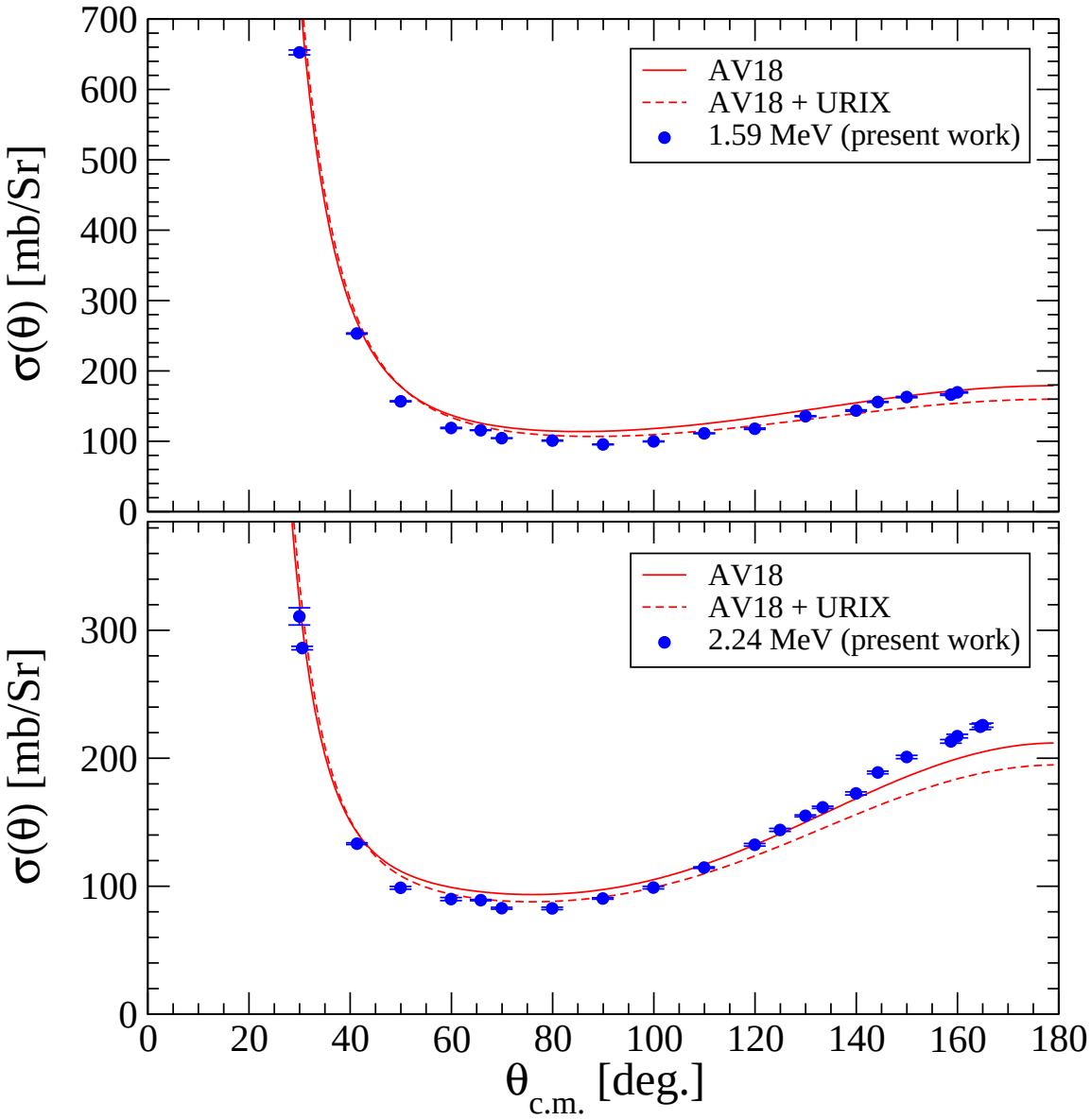

Figure 6.4: New $\sigma(\theta)$ results at E_{p}= 1.59 and 2.24 MeV compared to the theoretical calculations from [Viv01]. The solid lines indicate calculations performed with the AV18 potential alone, while the dashed curves indicate the addition of the URIX three-nucleon interaction.

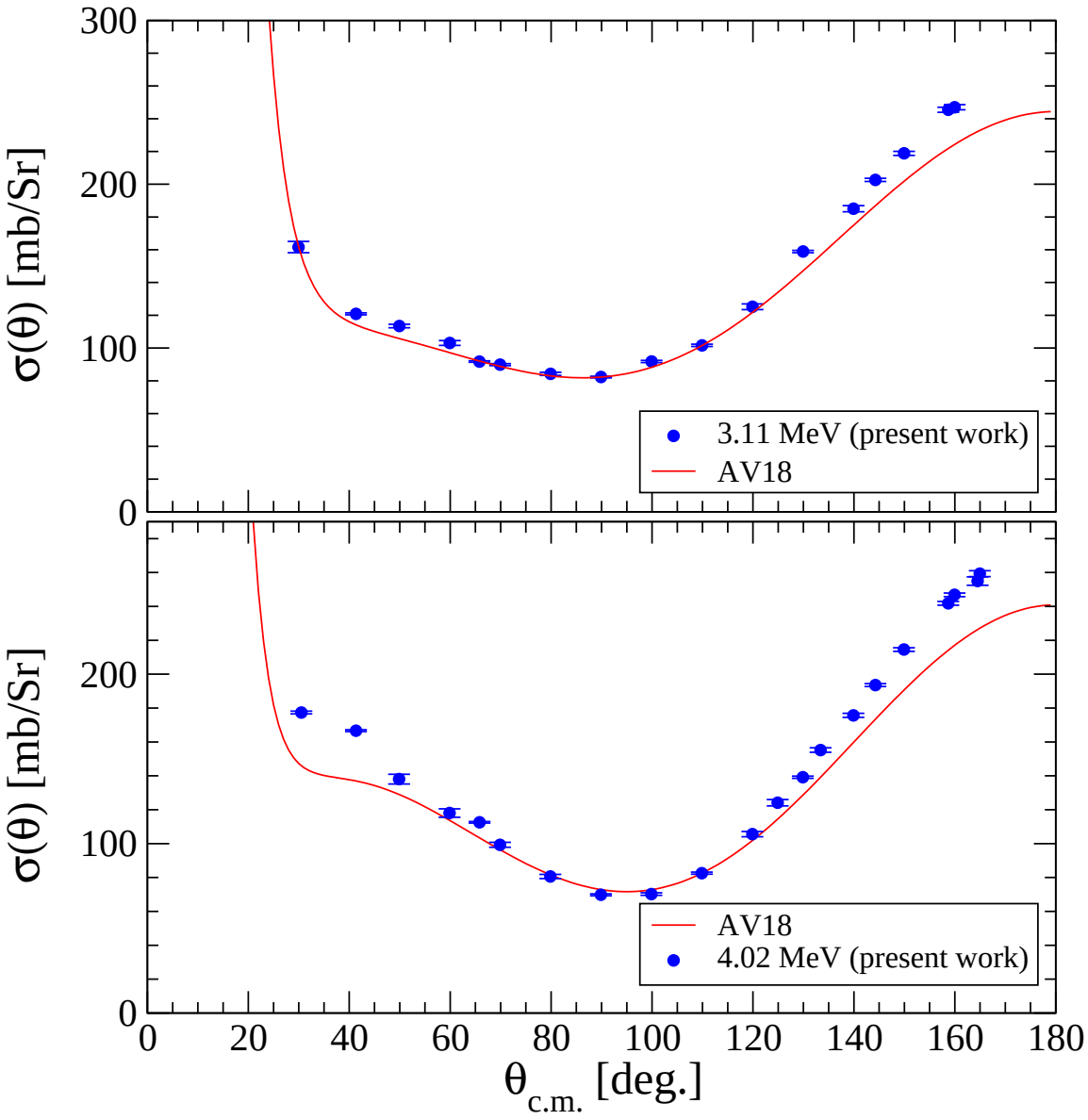

Figure 6.5: New $\sigma(\theta)$ results at $E_{\rm p}$= 3.11 and 4.02 MeV compared to the theoretical calculations of [Viv02]. These calculations include the AV18 NN interaction only.

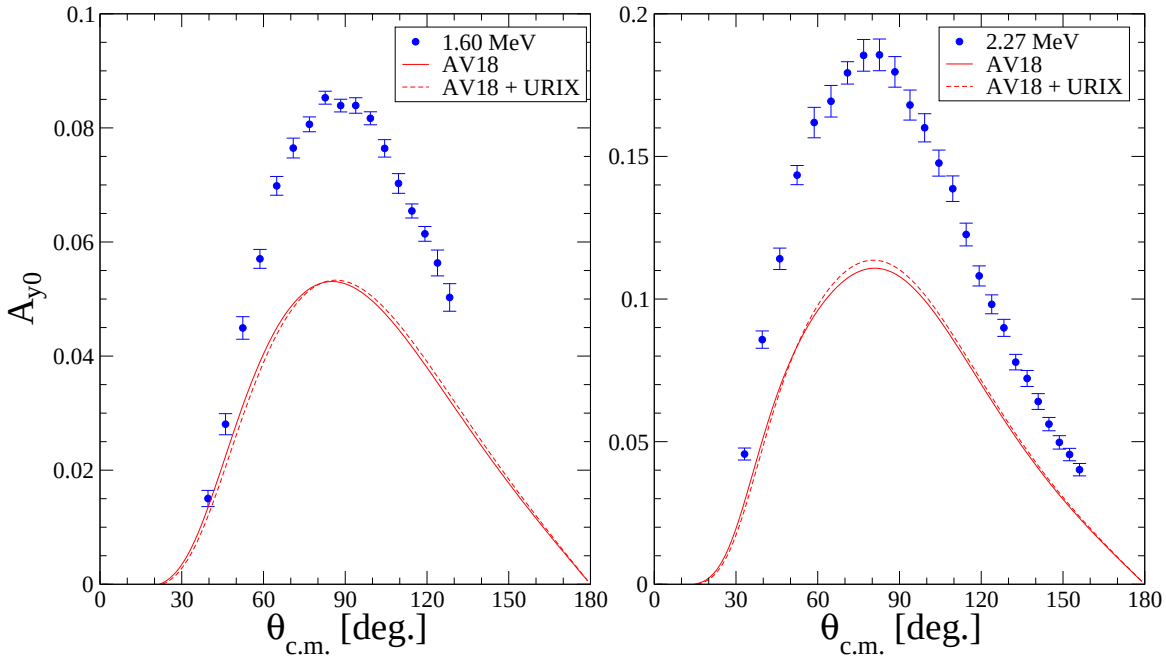

Figure 6.6: New A_y results at E_p= 1.60 and 2.25 MeV as compared to the theoretical calculations from [Viv01]. The solid lines indicate calculations performed with the AV18 potential alone, while the dashed curves indicate the addition of the URIX three-nucleon interaction.

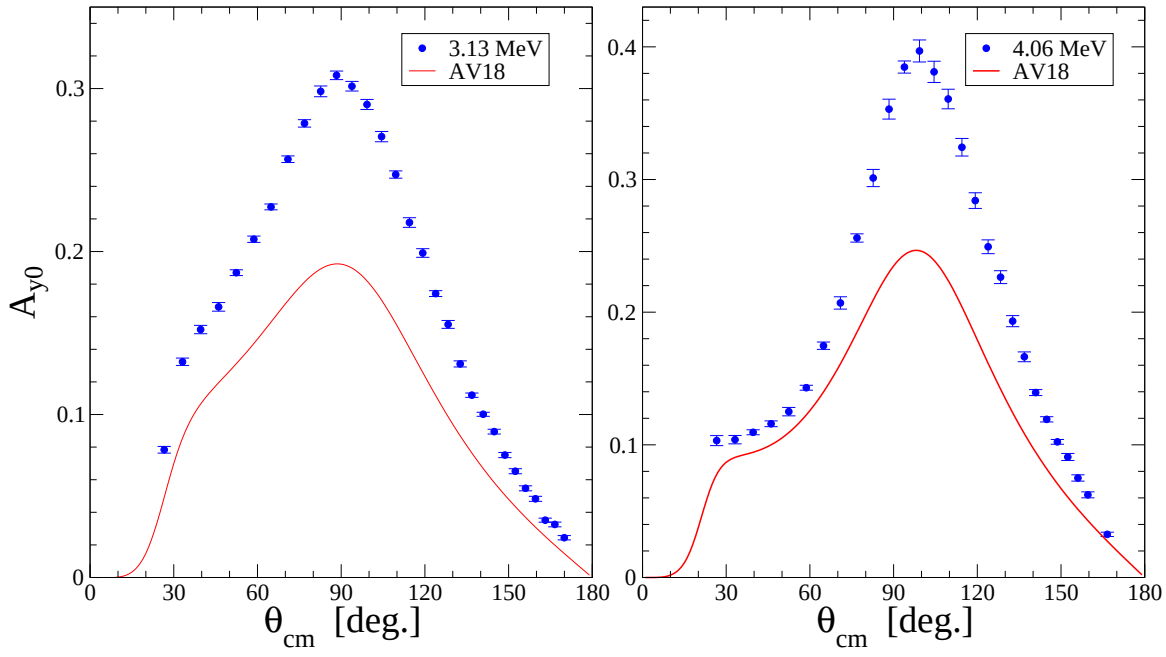

Figure 6.7: New A_y results at E_p= 3.11 and 4.02 MeV compared to the theoretical calculations of [Viv02]. These calculations include the AV18 NN interaction only.

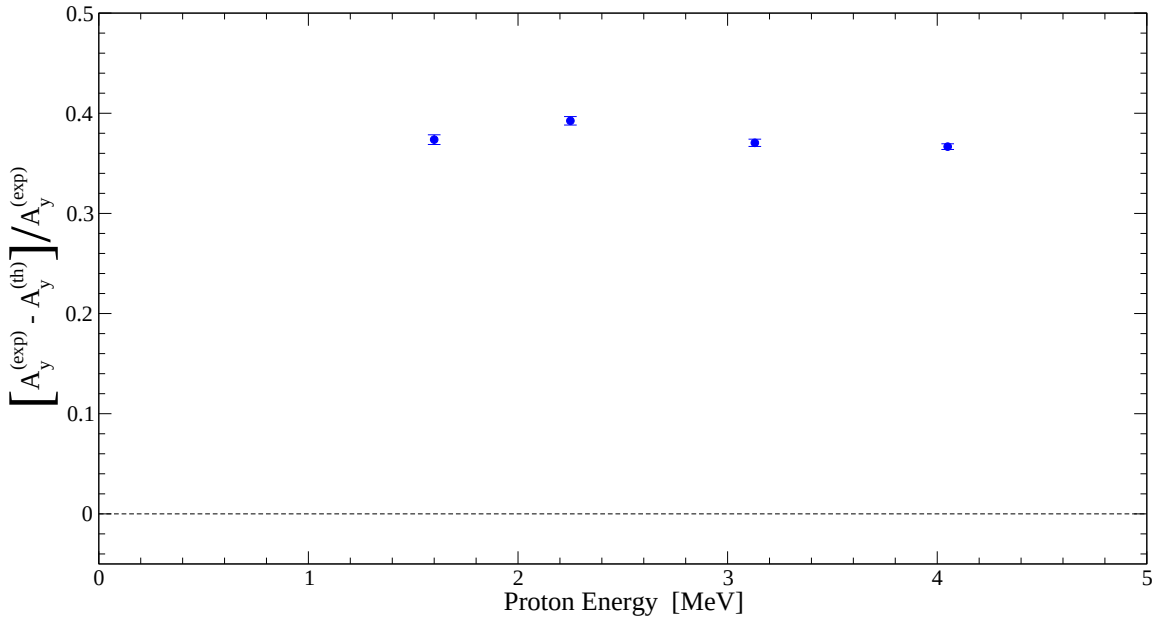

Figure 6.8: Energy dependence of the "A_y Puzzle" in p-^{3}He scattering.

was divided by the experimental value. As can be seen, there is a consistent flat $\approx 40\%$ underprediction of the maximum A_y value by the calculations. Calculations are needed at other energies to see if this trend continues or has a slope, as in the proton-deuteron case (see Figure 1.2.)

6.2.3 χ^2 Analysis

To determine quantitatively how well the theoretical calculations describe the data, the χ^2 was calculated. It is defined as

$$\chi^2 = \sum_i^N \left[\frac{x_i - y_i}{\Delta x_i}\right]^2, \tag{6.1}$$

where x_i is the i^{th} experimental value with an error of Δx_i. The corresponding theoretical value is y_i. The χ^2 measure is then a sum over all N data points. If the difference between the theoretical and measured values is equal to the error for every data point, the χ^2 is equal to N. If we normalize this measure to the number of data points, we get the χ^2 per datum, or

$$\chi^2_N = \frac{\chi^2}{N}. \tag{6.2}$$

Table 6.1: χ^2_N values for each observable at the energies at which calculations are available.

			χ^2 per datum					
	# of Points		AV18 Only			AV18 + URIX		
$E_{\rm p}$[MeV]	$\sigma(\theta)$	A_y	$\sigma(\theta)$	A_y	Total	$\sigma(\theta)$	A_y	Total
1.60	17	18	15.4	308	166	10.4	302	161
2.25	22	26	16.7	133	80	26.0	127	81
3.13	17	31	9.9	760	494			
4.05	20	30	58.5	1150	701			

Having $\chi^2_N = 1$ for a data set means that the theoretical calculation describes the data perfectly, within it's error.

Table 6.1 shows the χ^2_N values for the angular distributions of A_y and $\sigma(\theta)$ at the energies at which calculations exist. As can be seen, in general, the χ^2_N values are well away from 1. Not only do the A_y data show large discrepancies, fairly significant ones exist for the $\sigma(\theta)$ measurements as well. The addition of the three-nucleon force improves the agreement of $\sigma(\theta)$ at 1.60 MeV, but makes things worse at 2.25 MeV. There is nearly no change in χ^2_N for A_y with the addition of the $3N$ interaction.

6.3 Phase-Shift Analysis

A more quantitative measure of the differences between theory and experiment can be found by using a phase-shift analysis (PSA) of the transition matrix M (Equation 4.4), which can be parameterized in terms of a partial-wave expansion, as described in any quantum mechanics textbook, e.g. [Mer98]. The PSA can also give us further physical insight into the dynamics of the scattering which can also help reveal the source of the discrepancies in the theory.

The partial wave expansion of M for p-^{3}He elastic scattering [All93b] is given by

$$M_{ss_zs's'_z} = \frac{i\sqrt{\pi}}{k}\Bigg[i\,C(\theta)\,\delta_{ss'}\,\delta_{s_zs'_z} + \sum_{ll'j}\sqrt{2l+1}\,\langle sls_z0|js_z\rangle \times \langle s'l's'_zs_z - s'_z|js_z\rangle\, i_{|l-l'|}\,U^j_{l's',ls}\,Y_{l'}^{s_z-s'_z}(\theta,0)\Bigg], \tag{6.3}$$

where s, s_z and s', s'_z are the "channel-spin" quantum numbers for the initial and final scattering states, respectively. We use the convention that $\boldsymbol{s_1} + \boldsymbol{s_2} = \boldsymbol{s}$ where $\boldsymbol{s_1}$ and $\boldsymbol{s_2}$ are the proton and ^{3}He spins, respectively. The center-of-mass wave number is given by

$$k = \frac{\mu v}{\hbar}, \tag{6.4}$$

where μ is the reduced mass. The Coulomb scattering amplitude $C(\theta)$ is

$$C(\theta) = \frac{1}{\sqrt{4\pi}}\,\eta\,\csc^2\left(\frac{\theta}{2}\right)\,e^{i\eta\log\csc^2\left(\frac{\theta}{2}\right)}, \tag{6.5}$$

where η is the Coulomb penetrability factor

$$\eta = \frac{Z_1Z_2e^2}{\hbar v}. \tag{6.6}$$

The $Y_l^{s_z}$ are the normalized spherical harmonics. The matrix U contains the phase shift information. It is related to the standard scattering matrix S by

$$U^j_{l's',ls} = e^{i(\alpha_l+\alpha_{l'})}\left(\delta_{l,l'}\delta_{s,s'} - S^j_{l's',ls}\right) = U^j_{ls,l's'}, \tag{6.7}$$

where the α's are the modified Coulomb phase shifts,

$$\alpha_0 = 0, \qquad \alpha_l = \sum_{s=1}^{l}\arctan(\eta/s). \tag{6.8}$$

For mixed angular momentum states, the S matrix is parameterized in the fashion of Blatt and Biedenharn [Bla52] as

$$S = \begin{pmatrix} \cos^2\epsilon\,e^{2i\delta_1} + \sin^2\epsilon\,e^{2i\delta_2} & \frac{1}{2}\sin 2\epsilon\left[e^{2i\delta_1} - e^{2i\delta_2}\right] \\ \frac{1}{2}\sin 2\epsilon\left[e^{2i\delta_1} - e^{2i\delta_2}\right] & \cos^2\epsilon\,e^{2i\delta_2} + \sin^2\epsilon\,e^{2i\delta_1} \end{pmatrix}, \tag{6.9}$$

where δ_1 and δ_2 are the "eigen phase-shifts" and $\epsilon = \epsilon(j^\pi)$ is the mixing parameter for states with the same total angular momentum j and parity π. Relationships between the M-matrix elements in this parameterization and the parameterization of La France and Winternitz (Equation 4.4) can be found in [All93b, Mat00].

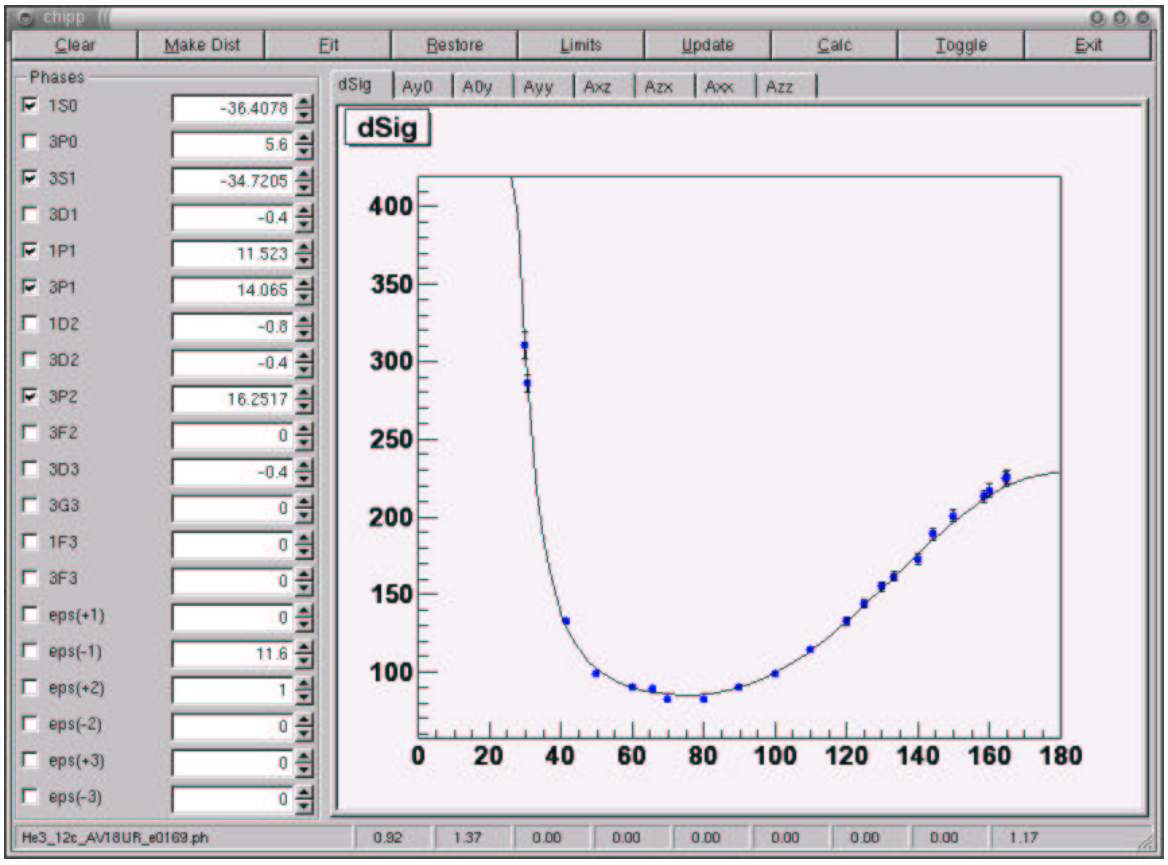

Figure 6.9: Screen-shot of CHIPP

6.3.1 Fitting Method

This standard parameterization allows us to perform a fitting procedure to the data to obtain phase-shifts for comparison with the theoretical predictions. Using a code obtained from the Pisa Group [Viv02] that calculates values of the observables from phase-shift and mixing parameter predictions as a starting point, a code has been written to perform the phase-shift fits to the present data. Written in C++, it is called CHIPP and uses the CERN ROOT Application Framework [Roo03], with the minimization algorithm MINUIT [Jam94]. A screen-shot of the code is shown in Figure 6.9. The code takes an input set of phase-shifts and experimental data and varies the selected free phase-shift parameters to minimize χ^2, as defined in Equation 6.1.

For each energy, the Pisa Group predictions, if available, were used as starting values. A search was then performed to find the best minimum χ^2 with the fewest

number of variable parameters, while keeping the results reasonable. If the resulting fit gave results significantly divergent from the results of [All93b], it was determined to be unphysical. The parameters that were varied were the $^1S_0$, $^3S_1$, $^1P_1$, $^3P_0$, $^3P_1$ and $^3P_2$ phase-shifts, and the $\epsilon(1^-)$ mixing parameter. The remaining parameters, which are quite small, were fixed at their theoretical values. The error bars on the best-fit values were determined by shifting the parameter in question from the best fit value until the total χ^2 increased by 1. This is performed by the MINUIT fitting algorithm.

6.3.2 Results

The results of these fits are shown in Tables 6.2, 6.3, and 6.4. Only 3, 4, or 5 parameters were allowed to be varied at each energy. Attempts to let more parameters vary, while often improving χ^2_N, gave unphysical results. This is an indication that additional observables are needed to fully constrain all the phase-shift parameters.

In general, good fits resulted, even when using as few as 3 free parameters. As can be seen from the tables, the $^3P_2$ phase-shift is particularly well-constrained by the present dataset, resulting in fit uncertainties of $< 1\%$. The S-wave parameters are less well determined by the fit. A plot of the phase-shift predictions of [Viv01] and [Viv02], the energy-dependent phase-shifts of [All93b] and the present results are shown in Figures 6.10 and 6.11. There is significant scatter amongst the current phase-shift analysis results. This is results mainly from the ad-hoc procedure of finding the minimum number of parameters needed to find a good, yet physical, fit to the data. To obtain a consistent fitting scheme, where a single set of phases is varied at each of the energies, more data – particularly of other spin observables – is needed. The current data sets are not large and diverse enough to constrain the phase-shift solutions in a consistent manner.

Table 6.2: PSA results at $E_{\rm p}$= 0.99 MeV. The results of the phase-shift analysis of [Bel85] were used as the starting values for this fit. The A_y data of [Ber80] were included in both fits. A blank entry in the table indicates that the phase-shift was held at its starting value.

Parameter	[Bel85][a]	PSA	PSA[b]
$^1S_0$	-18.1	-16.7 ± 3.8	-17.4 ± 2.5
$^3S_1$	-17.2	-18.3 ± 1.2	-17.9 ± 0.8
$^1P_1$	1.6		
$^3P_0$	1.6		
$^3P_1$	3.7	4.97 ± 0.15	5.14 ± 0.08
$^3P_2$	3.4	3.78 ± 0.04	3.821 ± 0.019
$\epsilon(1^-)$	10.6		
χ^2_N $\sigma(\theta)$	23.2	0.88	1.10
χ^2_N A_y	1.3	0.73	0.71
χ^2_N Total	14.5	0.82	0.98

[a] S-wave phases taken from [All93b].

[b] Fit performed with addition of $\sigma(\theta)$ data of [Ber80].

Table 6.3: Phase-shift analysis results for $E_{\rm p}$= 1.59 and 2.24 MeV. The AV18 and AV18 + UR(IX) predictions are those of [Viv01]. A blank entry in the table indicates that the phase-shift was held at its starting value.

	$E_{\rm p}$= 1.59 MeV			$E_{\rm p}$= 2.24 MeV		
Parameter	AV18	AV18 + UR(IX)	PSA	AV18	AV18 + UR(IX)	PSA
$^1S_0$	-31.3	-31.3	-24.7 ± 0.9	-42.3	-40.1	-36 ± 4
$^3S_1$	-28.8	-27.1		-36.9	-35.0	-34.7 ± 1.5
$^1P_1$	6.5	5.5	4.6 ± 1.0	10.0	8.8	11.5 ± 1.1
$^3P_0$	4.1	3.2		6.8	5.6	
$^3P_1$	8.1	7.4	10.1 ± 1.1	13.8	12.8	14.1 ± 1.2
$^3P_2$	7.8	7.0	8.22 ± 0.16	13.6	12.6	16.25 ± 0.13
$\epsilon(1^-)$	14.7	13.2		12.3	11.6	
χ^2_N $\sigma(\theta)$	15.4	10.4	2.5	16.7	26.0	1.02
χ^2_N A_y	323	317	2.8	211	202	1.93
χ^2_N Total	170	164	2.6	126	124	1.53

Table 6.4: Phase-shift analysis results for $E_{\rm p}$= 3.11 and 4.02 MeV. The 4.02 MeV fit includes the $\sigma(\theta)$ data of [McD64] at 4.0 MeV. The AV18 predictions are that of [Viv02]. A blank entry in the table indicates that the phase-shift was held at its starting value.

	$E_{\rm p}$= 3.11 MeV		$E_{\rm p}$= 4.02 MeV	
Parameter	AV18	PSA	AV18	PSA
$^1S_0$	-51.3	-50.4 ± 2.3	-58.0	
$^3S_1$	-45.3	-43.0 ± 0.6	-53.5	-49.6 ± 0.2
$^1P_1$	13.9		17.2	
$^3P_0$	10.7	9.3 ± 0.3	14.5	16.4 ± 0.3
$^3P_1$	23.1	25.0 ± 0.3	30.2	34.4 ± 0.2
$^3P_2$	22.8	27.31 ± 0.15	30.7	37.40 ± 0.13
$\epsilon(1^-)$	10.0		9.8	13.7 ± 0.4
χ^2_N $\sigma(\theta)$	9.9	1.31	43.2	2.23
χ^2_N A_y	680	1.39	261	1.78
χ^2_N Total	437	1.36	147	1.87

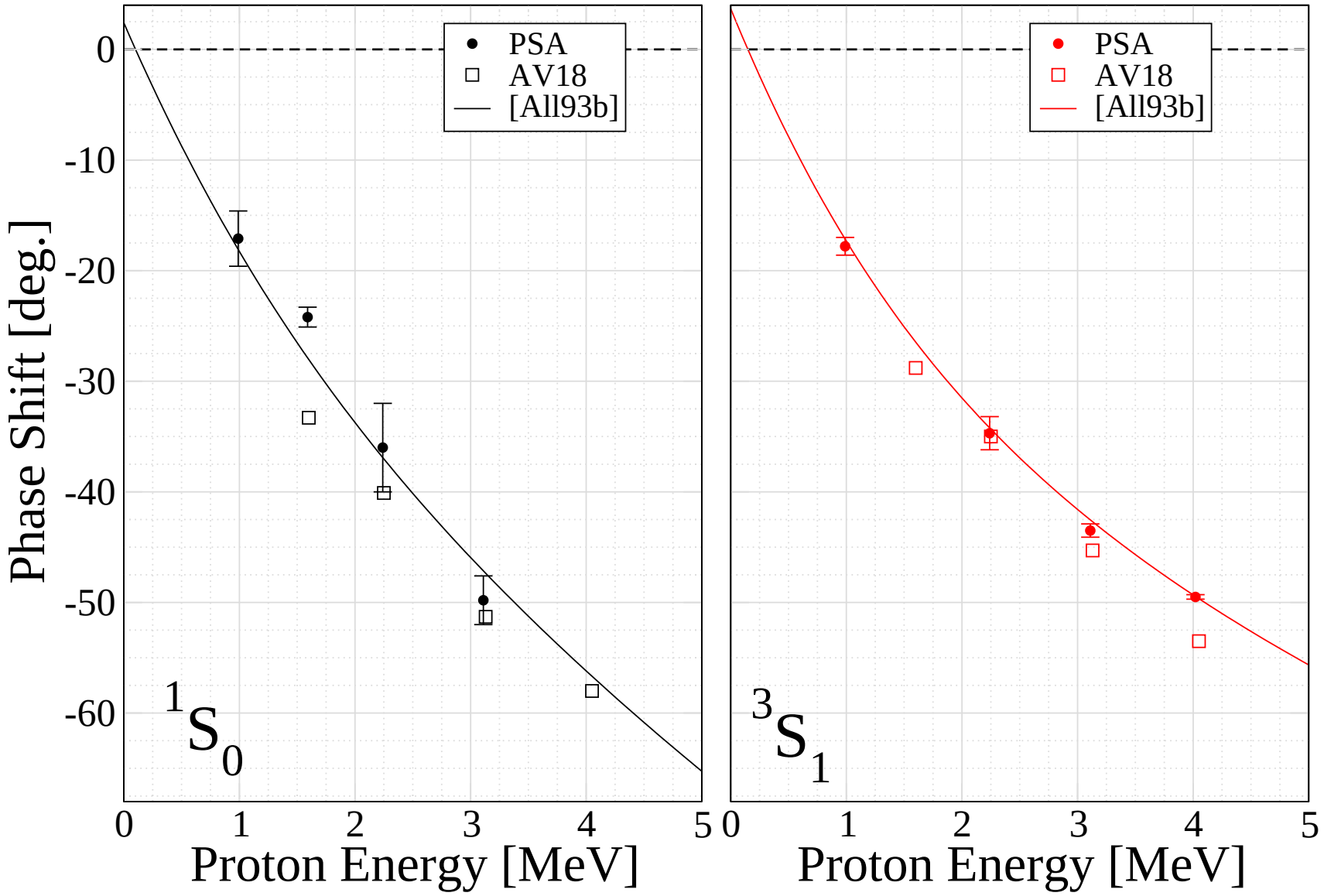

Figure 6.10: Comparison of current phase-shift fits with previous work. Shown as squares are the phase-shift predictions of [Viv01] and [Viv02]. The curves are the phase-shift fits from [All93b] and the dots are the present results.

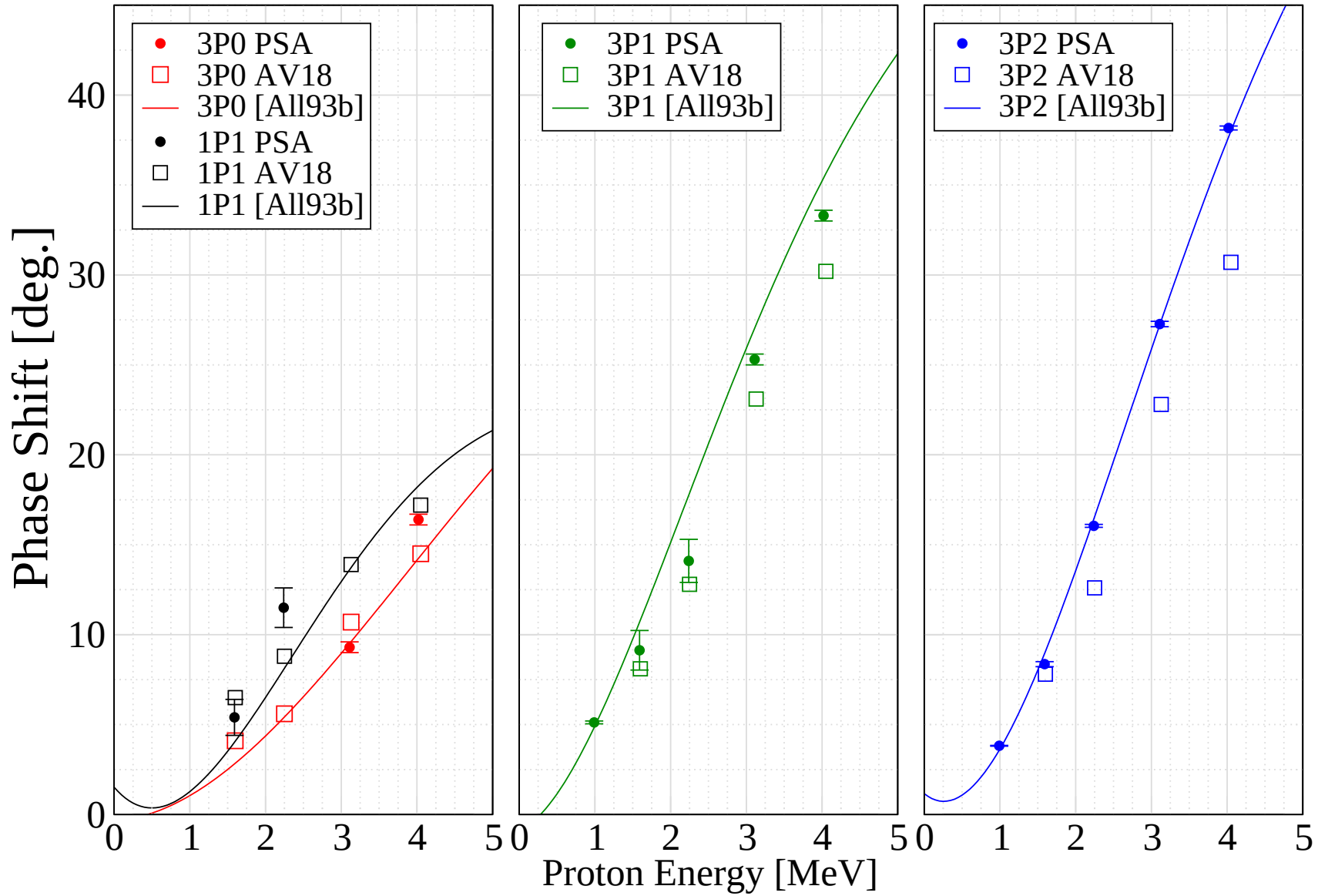

Figure 6.11: Comparison of current phase-shift fits with previous work. Shown as squares are the phase-shift predictions of [Viv01] and [Viv02]. The curves are the phase-shift fits from [All93b] and the dots are the present results.

Chapter 7

Conclusions and Future Work

This chapter summarizes the current work and suggests avenues for future research, including a polarized ^{3}He target and the experiments such a target would allow. A discussion of potential solutions to the "A_y Puzzle" is also presented.

7.1 Summary

High precision measurements of angular distributions of the differential cross section $\sigma(\theta)$ have been performed at $E_{\rm p}$= 0.99, 1.59, 2.24, 3.11, and 4.02 MeV. These data have a statistical uncertainty of approximately 0.4% and a normalization error of 2-3%. To perform these measurements, a high-density supersonic gas-jet target has been refurbished, upgraded, and installed at Triangle Universities Nuclear Laboratory. The target properties and operational parameters were investigated so that accurate, high-precision angular distributions can be obtained. The majority of effort (not to mention sweat and heavy lifting) in this work was in this target development.

Complementary measurements of the proton analyzing power A_y have been made at $E_{\rm p}$= 1.60, 2.27, 3.13, and 4.06 MeV, with statistical errors of 1.5-3% and a systematic multiplicative scaling error of $\approx$ 2% from polarimetry.

These data were compared with previous data taken at the same energies, and with variational calculations performed by the Pisa Group [Viv01, Viv02] using realistic

NN and $3N$ potentials. There is agreement of the current data with previous ones, with a marked increase in both the number of data points, and in the precision of the data. This is seen particularly in the analyzing power measurements at 1.60 and 2.27 MeV. With this increased precision, comparisons to the theoretical predictions gain more meaning. Neither the NN only, nor the $NN+3N$ calculations, predict the cross section data within its error bars. The precision of the previous data [Fam54] did not allow such a distinction to be made since the data agreed with both calculations, except at the most backward angles.

Comparison of the current A_y data with the realistic calculations shows that the A_y Puzzle most definitely exists in the proton-^{3}He system. Indeed, the $\approx 40\%$ discrepancy seen at the peak of the angular distribution is larger than the typical discrepancies seen in the Nd case. For the energies where both NN and $NN + 3N$ calculations exist, the addition of the $3N$ force seems to have no effect on the prediction. This discrepancy, so far, does not seem to have an energy dependence. Calculations at other energies are forthcoming, and should shed light on this [Viv03].

Our phase-shift analysis confirmed what has been seen in other systems, namely the very strong dependence of the "A_y Puzzle" on P-waves. In particular, the $^3P_2$ phase-shift plays a very prominent role in predicting A_y. The $^3P_1$ phase-shift also is important. The phase-shift solutions, however, are model-dependent since many of the (smaller) phase-shifts were held at their theoretical values in order to get a sensible solution. This is necessary because of the lack of other spin observables at these energies.

7.2 Future Work

Investigations into proton-^{3}He elastic scattering and the A_y puzzle in general will continue on both theoretical and experimental fronts. Theoretically, new developments in potentials and new formulations of the three-nucleon force could play a role, while on the experimental front new target technology and measurements at even lower energies will be important.

7.2.1 Theory

The A_y puzzle is, of course, not solved from the results of this work, though features of the puzzle seen in other systems are definitely present. The strong dependence of the predictions on P waves has been known for quite some time, and is quite evident in the present analysis. There have been suggestions that deficiencies in the low-energy ${}^3P_j$ phases in NN database – the database to which all realistic potential models are fit – could fix the A_y puzzle globally [Tor98], though not without potentially changing the two-body observables [Hüb98]. This suggestion that the NN phases could be wrong has motivated a new effort to measure analyzing powers for p-p [Gup02] and n-p [Tor02] elastic scattering at very low energies, where there are few data. The proton-proton experiment will use the very high target thicknesses obtainable with the gas-jet target, which are needed to measure such small analyzing powers.

The three-nucleon force, however, seems a more likely venue to find the "smoking gun" that solves this mystery. New forms of $3N$-forces have been developed that could potentially bring the calculations into agreement with the data, such as the $\boldsymbol{L}\cdot\boldsymbol{S}$ force of [Kie99]. These solutions are phenomenological and ad-hoc however.

What gives many theorists hope is the recent rapid development of an effective field theory (EFT) approach to constructing the nucleon-nucleon potential. This method, it is felt, has a more solid basis in QCD, respects the chiral symmetries in that theory, and prescribes a very strict method of power-counting to determine which interactions are most important. A discussion of the methods used in constructing such an chiral EFT potential is beyond the scope of this work. A good review can be found in [Bed02].

A recent result using this method which employed a potential calculated out to "next-to-leading-order" (NLO) claimed to have solved the Nd A_y puzzle [Epe01]. However, a much more detailed examination of the phase shift predictions of the NLO potential [Ent02], and taking the calculation out to NNLO (next-to-next-to-leading-order) found that the A_y puzzle reappears [Epe02]. Despite these setbacks, it is expected that once the calculations reach order 4, that three-nucleon forces will

be found that have not been considered before [Ent02]. Once such potentials are constructed, calculations of proton-^{3}He elastic scattering can be performed to see if the puzzle has disappeared in this system as well in the Nd case.

7.2.2 Experiment

Future proton-^{3}He elastic scattering experiments need to address both the A_y puzzle and the poor determination of the scattering lengths. As was discussed in Section 1.2.4, the zero-energy scattering parameters are not well defined. While the inclusion of the data from the present work will help the situation, the current energy-dependent phase-shift fits give vastly different solutions for the scattering lengths depending on whether the very low energy (0.3 - 1.0 MeV) cross-section data of Berg *et al.* [Ber80] are included. The present work overlapped with the Berg data at 1.0 MeV, with which the new $\sigma(\theta)$ measurements seem to agree well. This is comforting since the Berg data were obtained using a different method. Measurements below 1 MeV should be performed to confirm the accuracy of the database in this region, which has the most effect on the scattering length extrapolations to zero energy. Experiments using the gas-jet target at these lower energies are feasible, when using inverse kinematics. An accurate determination of the p-^{3}He scattering lengths — one including the high precision data taken for this work — is also necessary for comparisons with results of the proposed measurement of the n-^{3}He scattering lengths at NIST [Bla03].

Similarly, to further constrain the phase-shift fits for both scattering length determinations, and to discover the origin of the A_y puzzle in proton-^{3}He scattering, measurements below 4 MeV of other spin observables are needed. As was seen in [All93b], these higher-order spin observables strongly constrain the phase-shift fits, allowing for a unique solution. There are currently no spin-correlation coefficient measurements below $E_{\rm p} = 5.54$ MeV, and no ^{3}He analyzing power A_{0y} measurements below 4 MeV. From a simple sensitivity study, these observables – particularly A_{0y} – are strongly dependent on P-wave strengths. Shown in Figure 7.1 are the A_{y0} data at 4.06 MeV from this work and the A_{0y} data at 4.01 MeV from [All93a]. The A_{y0} data,

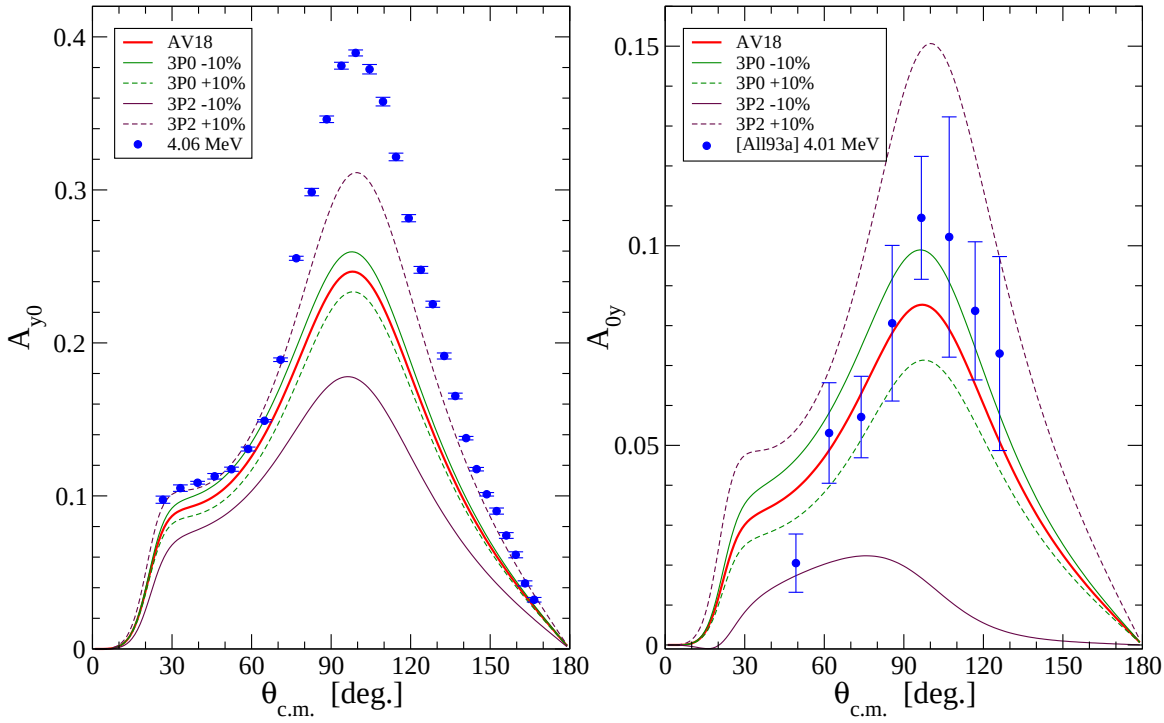

Figure 7.1: Sensitivity study of A_{y0} and A_{0y} to certain P-waves at $E_{\rm p}$= 4 MeV. On the left is the present A_{y0} data at 4.06 MeV, showing the $\approx$ 40% discrepancy from the AV18 prediction. On the right is the A_{0y} data at 4.01 MeV from [All93a] with the same AV18 calculation [Viv02]. The predictions from varying $^3P_0$ and $^3P_2$ each by $\pm$10% are shown.

as is well known, are under-predicted by $\approx$ 40% by the AV18 prediction. However, A_{0y} data agree with the same AV18 prediction, though the error bars are rather large to make a definitive statement. The $^3P_0$ and $^3P_2$ phases were each independently varied by $\pm$10% from the AV18 + UR(IX) prediction. The A_{0y} calculation shows much larger changes (relative to the size of the observable) than in the A_{y0} case. This shows that A_{0y} is particularly sensitive to these P-waves. New measurements of A_{0y} below 4 MeV will provide a strict constraint on phase-shift solutions.

Measurements of A_{0y} and the spin-correlation coefficients A_{yy}, A_{zz}, A_{xz}, etc. require a polarized ^{3}He target. Design, development, construction, and testing of such a target is currently underway [Cle02], with the design goal of having a target cell with $\approx$ 0.5 atm of 50% polarized ^{3}He available for low-energy scattering experiments. These data should also constrain the results of the scattering length determinations.

Appendix A

The TUNL Gas Jet Target Operations Manual

The TUNL Gas Jet Target is a complicated apparatus. This appendix is an attempt at writing down some semblance of an operating procedure, since the folks at Erlangen never did such a thing (as far as I can tell.) In its current state, the information here is in no way exhaustive nor likely to be the optimal way of doing things, but should let one get the target running in some state resembling a gas jet.

I wish you good luck, and may the Fates smile upon you while operating the target.

A.1 Chamber Setup

The detector mounting ring was developed so we can run 3 detectors, equally spaced at 10° on each side of the target. Additionally the monitor detector holders can be installed. The chamber detector holder setup is shown in Figure 4.3.

1. After the detectors are in, put the two concentric rings into the chamber in the correct orientation. Make sure the set-pins fit into the proper slots. While the ring does not have an apparent orientation, we do like to install it such that the hole for the jet profiling rod is on the right (where it needs to be if we need to profile the target.)

2. Place the lid/nozzle assembly onto the two rings. Again, make sure the set-pins are in the proper slots and that everything is centered.

3. Attach the gas-inlet hose to the VCO connector on the nozzle lid. Remember to use opposing wrenches so not to snap off the inlet connector.

4. Install the two cross-braces. These are the long bars with knobs that press the nozzle lid into the two rings. There should be one bar on either side of the center of the lid. Tighten the knobs so that everything is secure.

5. Make sure the cable that goes to the nozzle height-measuring-resistor is attached to one of the feed-throughs on the side of the chamber, and that the chamber entrance snout slit wires are also connected.

6. Before lowering the lid, make sure that the adjustment teeth are lined up with their matching slots on the nozzle lid. Lower the chamber lid slowly to make sure that the teeth and the slots mate properly.

If everything is closed up, you should be able to begin pumping the chamber out and start up the jet.

A.2 Startup Procedure

Starting up the gas jet involves turning on the various pumping stages and watching the chamber vacua. With the fancy Balzers MaxiGauge system, we can monitor the vacua easily. This gauge is located on the turbopump stand before the chamber. It reads the Stage 1, 2, and 3 vacua, along with the chamber and beamline vacua.

There are also a few other meters for monitoring vacua. The black thermocouple (TC) gauge is located atop the power distribution box on the front of the chamber frame. There is also a Penning gauge controller located on the floor near the diffusion pump. A listing of the gauges and their readout locations are listed in Table A.2.

1. Make sure the stage two and two butterfly valves and the diff-pump gate valve is closed. Also make sure that the electromechanical shutoff-valve on the gas input line is closed (its switch should read "off"). The chamber beamline valve and the upstream hand valve should also both be closed.

Table A.1: Vacuum gauge readout locations.

Gauge Location	**Readout Location**
Diff pump foreline	black TC position 1
Diff pump below baffle	black TC position 2
Diff pump below baffle	Penning controller on floor near pump.

2. Turn on the main power. The knife switch (the left one) on the wall may have to be first turned on. The "ignition" key for the power distribution panel is located in the "vacuum grease" drawer in the 52° cabinet. Turn the key and press the big green button. You are now ready to begin turning on the pumps.

3. Turn on the backing to the diffusion pump. The foreline vacuum can be read on station 1 of the black TC gauge.

4. Once the foreline pressure gets below 15 mTorr, turn on the diffusion pump. It takes $\approx$ 30 minutes for the diffusion pump to heat up.

   While the diffusion pump heats up, you can begin pumping out the main chamber. **It is ideal to turn on the different pumping stages slowly to avoid tripping circuit breakers, or worse, blowing fuses.**

5. Turn on stage one. Slowly open its butterfly valve. The stage one vacuum can be read on the MaxiGauge.

6. Currently there is a butterfly-valve between the stage two pumps and the chamber. However, there is no pressure gauge at that point. When the stage one pressure gets down to about 2-5 Torr, turn on stage two. Wait a few seconds and then slowly open the butterfly-valve to the chamber. The pressure in the chamber should begin to come down much more quickly.

7. Once the three phase current meters (on the front of the power-distribution panel) reaches $\leq$ 20 A, turn on stage 3. The MaxiGauge controller should now

read around 10^{-3} Torr for stages 2, 3 and the chamber. Stage 1 will probably only be around 10^{-2} Torr.

8. If all three stage pressures look acceptable, open the gate valve to the diffusion pump. The chamber vacuum should immediately decrease to $\sim 5 - 7 \times 10^{-5}$ Torr.

9. You can now begin to make the gas-jet. Set the pressure regulator on the gas bottle to a reasonable level (around 50 psi.)

10. Make sure the switch on the mass-flow controller (MFC) is set to OFF, and that MFC is zeroed. A reasonable initial set-point on the MFC when running with hydrogen is about 80.

11. Open the regulator access valve to allow gas to flow up to the MFC.

12. Flip the switch on the electromechanical valve. This allows the pumps to evacuate fully the gas line from the MFC to the nozzle.

13. To start the jet, flip the MFC switch to ON. All pressures will, of course, get worse. Make sure that the chamber pressure is low enough to prevent the electrical breakdown of the detectors.

14. If everything looks good, open the chamber beamline valve. Watch the beamline vacuum on the MaxiGauge. It will probably read low 10^{-5} - high 10^{-6}.

15. If the beamline vacuum is acceptable, open the beamline hand valve. The jet is now ready for beam.

A.3 Nozzle and Catcher Adjustments

- Both the nozzle and catcher heights can be adjusted by motors external to the chamber. Currently the system is quite primitive. The motors are operated by generic power supplies and the positions are read by multi-meters set to

measure resistance. They are usually remotely controlled using a power supply in the control room.

- The nozzle adjustment sometimes gets bound up for yet unknown reasons. If you can't get the nozzle height to move you most likely have to open up and wiggle the nozzle height adjuster manually.

- The current standard way of finding the optimal nozzle and catcher positions is to move them to positions well out of the path of the beam. Then with a beam tuned into the chamber, but with no jet running, slowly move each toward the beam position while watching the detector signals on an oscilloscope. When it is obvious that the nozzle or catcher is intercepting the beam, back the position off slightly, until the intensity decreases. Do this for both the nozzle and catcher.

A.4 Shutdown Procedure

1. Close the chamber beamline valve.

2. Turn off the gas jet by first turning the MFC to OFF, and then closing the electromechanical valve.

3. Turn off the suppressor supply.

4. De-bias any detectors.

5. Close the diffusion pump gate valve.

6. Turn off stage 3, then stage 2 (and close the butterfly valve), and finally stage 1. Make sure the butterfly valves are closed on both stage 1 and 2.

7. The chamber will leak up somewhat (mainly due to the slow closing time of the SECUVAC valve on Pump 1) but you'll still have to vent with the valve located on the back side of the polarimeter slot.

8. Open up. If you are shutting down for an extended period of time, turn off the diffusion pump, but leave the fore-pump running for at least an hour to allow the diffusion pump to cool.

9. Turn off the "ignition key". Put it in the "vacuum grease" drawer in the 52° chamber cabinet.

10. Turn off the knife switch, just to be safe.

A.5 Things to Worry About

- It is very easy to bump the emergency stop button with a ladder or your knee when working in the chamber. This will turn off the diffusion pump and its backing pump. This is not a good thing.

- Make sure that the beamline vacuum is good enough for it to be opened up to the tandem. There are no "fast-acting" valves in the 44° beamline at this time.

- The gas-jet is a gas-hog. Please monitor your gas consumption so we can figure out how to fix this.

- **Most of all, just be careful.**

Appendix B

Bending Magnet Calibration

Since the data taken for this work were measured in two different scattering chambers, as described in Chapter 4, an accurate calibration of the bending magnet was needed for both beamlines. The magnetic field B necessary to bend a beam of particles with charge q, mass m, and kinetic energy E through a given angle is given by

$$B = \frac{\sqrt{E^2 + 2Emc^2}}{Cq} \tag{B.1}$$

where C is the radius of curvature of the beam multiplied by constants so that the beam energy, magnetic field, and the mass of the projectile are expressed in convenient units. A more involved derivation of this formula can be found in [Fis97a], [Wil82], or any electrodynamics textbook.

B.1 Experimental Method

The method used to calibrate the bending magnet was the same used for the calibration of the 90-90 high resolution system at TUNL. It is described in [Wil82] and [Wil83]. The reactions used for the magnet calibration are listed in Table B.1. A good review of available reactions that are often used for accelerator calibrations can be found in [Mar66].

A proton beam from the DENIS II source was sent through the tandem accelerator and then momentum analyzed by the 20-70 magnet into either the 44° or 52° beam-lines. Each of the targets was, in turn, mounted on the end-cap of the beam-line. Starting with a beam energy about 10 keV below the threshold (by an earlier calibration), the beam energy was incremented in roughly 1 keV steps over the reaction

Table B.1: Reaction energies used for the 52° and 44° beamline calibrations.

Reaction	Target	Energy [keV]	Reference
^{27}Al(p,γ)^{28}Si	Solid Al	991.86 ± 0.03	[End90]
^{7}Li(p,n)^{7}Be	Evaporated LiF on Ta	1880.41 ± 0.08	[Bar81]
^{13}C(p,n)^{13}N	^{13}C foil target from H. Weller	3234.7 ± 0.7	[Mar66]
^{19}F(p,n)^{19}Ne	Evaporated CaF_2 on Ta	4234.3 ± 0.80	[Mar66]
^{27}Al(p,n)^{27}Si	Solid Al	5803.3 ± 0.26	[Nay77]

threshold. A BF_3 "long counter," as used in [Wil83], was placed at 0° to detect the neutrons. The energy excitation functions were continued well above the threshold energy. The beam current was integrated for normalization. For ^{27}Al(p,γ)^{28}Si, a high purity germanium detector was used as the beam energy was stepped over the E_{p}= 992 keV resonance.

B.2 The Analysis

The (p, n) threshold reactions were analyzed using the thick-target relation for s-wave neutrons emerging just above threshold energy, where the neutron yield varies as the $\frac{3}{2}$ power of E_{n}, the outgoing neutron energy [Mar66]. The region below the threshold was fit with a linear least-squares to obtain the background neutron yield. This calculated background was subtracted from the original yield to obtain the true counts. The true counts were then raised to the $\frac{3}{2}$ power, which can be fit by a linear least-squares to obtain the zero intercept of the line and hence the threshold energy [Wil82].

The data and results of this fitting procedure for the measurements made for the 52° beamline are shown in Figures B.1(a) and B.1(b). Similar fits were performed for the 44° calibration.

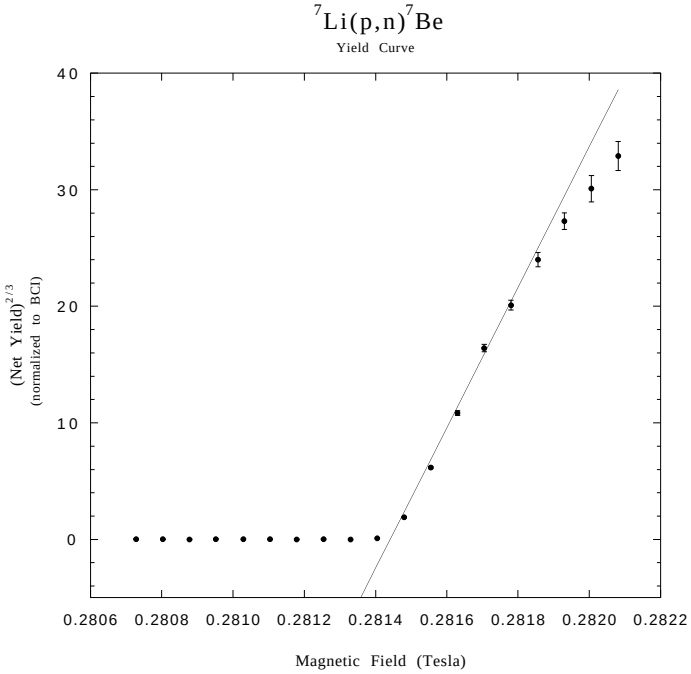

(a) ^{7}Li(p,n)^{7}Be Yield Curve

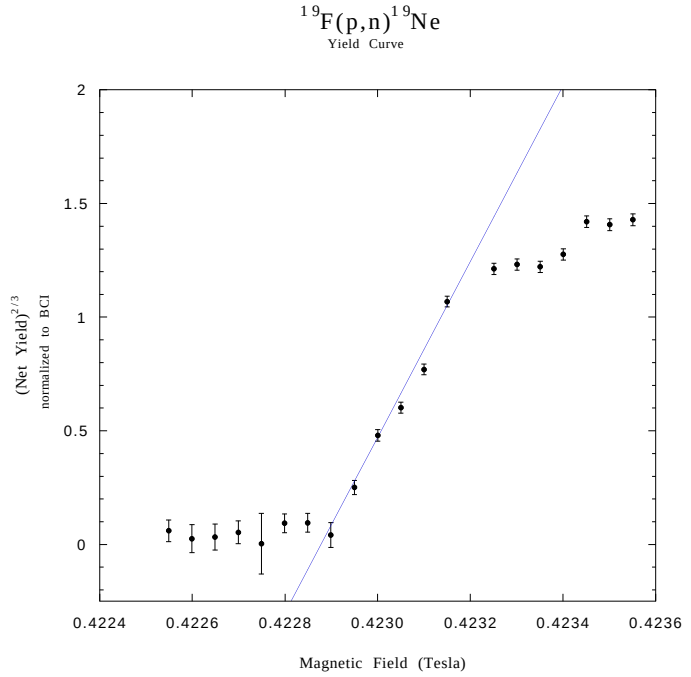

(b) ^{19}F(p,n)^{19}Ne Yield Curve

Figure B.1: Yield curves for ^{7}Li(p,n)^{7}Be and ^{19}F(p,n)^{19}Ne

Table B.2: Results of the 44° and 52° magnet calibrations.

52° beamline		44° beamline	
Reaction	C [MeV/T]	Reaction	C [MeV/T]
^{7}Li(p,n)^{7}Be	211.17 ± 0.9	^{7}Li(p,n)^{7}Be	244.23 ± 0.03
^{19}F(p,n)^{19}Ne	211.03 ± 0.8		244.03 ± 0.06
		^{13}C(p,n)^{13}N	243.99 ± 0.06
		^{19}F(p,n)^{19}Ne	244.13 ± 0.17
		^{27}Al(p,n)^{27}Si	244.17 ± 0.08
Adopted Value	211.10 ± 0.7	Adopted Value	244.09 ± 0.03

B.3 Results and Conclusions

The results for the magnet calibrations of the 52° beamline are given in Table B.2. In order to determine if C for both the 52°- and 44°-line is truly constant, more data points at higher energies are needed. Measurements of (p, p) resonances are the obvious choice. The adopted values were used in calculating the necessary magnetic field settings for all the experiments performed as part of this work.

Appendix C

Data Tables

The analyzed data sets measured for this work are listed in the following tables. The tables are grouped by energy, since the $\sigma(\theta)$ and A_y were taken at (nearly) the same center-of-mass energy (see Section 4.3) and are labeled as such. The values and the respective errors are given in each column. The errors include the uncertainties resulting from counting statistics, background subtraction, and, in the case of the A_y measurements, the statistical uncertainty from the beam polarization determinations. The corresponding systematic errors for the $\sigma(\theta)$ measurements are discussed in Sections 5.2.3 and 5.2.4. There is a 2% systematic error on the A_y measurements originating from the beam polarization determinations. All $\sigma(\theta)$ values are in mb/Sr.

Table C.1: Absolute $\sigma(\theta)$ data at $E_{\text{c.m.}}$= 0.74 MeV.

$\theta_{\text{c.m.}}$	$\sigma(\theta)$	$\Delta\sigma(\theta)$
30.0	2080	30
30.5	1960	20
41.3	686	7
50.0	377	5
60.0	241	3
65.8	205	2
70.0	183	2
80.0	152	2
90.0	134.1	1.5
100.0	127.8	1.6
110.0	122.0	1.3
120.0	120.3	1.5
125.0	120.5	1.6
130.0	121.9	1.3
140.0	124.7	1.4
144.2	125.3	1.3
150.0	126.4	1.4
158.7	128.1	1.4
160.0	130.2	1.4
164.5	129.4	1.7
165.0	130.6	1.5

Table C.2: $\sigma(\theta)$ data at $E_{\text{c.m.}}$= 1.19 MeV.

$\theta_{\text{c.m.}}$	$\sigma(\theta)$	$\Delta\sigma(\theta)$
30.0	650	20
41.3	255	8
50.0	158	5
60.0	120	4
65.8	116	3
70.0	105	3
80.0	101	3
90.0	96	3
100.0	100	3
110.0	112	3
120.0	118	4
130.0	136	4
140.0	145	4
144.2	157	5
150.0	164	5
158.7	167	5
160.0	171	5

Table C.3: A_y data at $E_{\text{c.m.}}$= 1.20 MeV.

$\theta_{\text{c.m.}}$	A_y	ΔA_y
39.6	0.015	0.0014
46.1	0.028	0.0019
52.4	0.044	0.002
58.7	0.057	0.0017
64.8	0.0698	0.0016
70.9	0.0764	0.0017
76.8	0.0806	0.0013
82.6	0.0852	0.0011
88.3	0.0839	0.0011
93.8	0.0839	0.0014
99.2	0.0816	0.0011
104.5	0.0764	0.0015
109.5	0.0702	0.0017
114.5	0.0654	0.0012
119.2	0.0614	0.0013
123.8	0.056	0.002
128.3	0.050	0.002

Table C.4: $\sigma(\theta)$ data at $E_{\text{c.m.}}$= 1.67 MeV.

$\theta_{\text{c.m.}}$	$\sigma(\theta)$	$\Delta\sigma(\theta)$
30.0	310	9
30.5	286	5
41.3	133	3
49.9	98	2
59.9	89	2
65.8	89	1.7
69.9	82.7	1.7
79.9	82.6	1.8
89.9	90.3	1.7
99.9	98	2
109.9	114	2
119.9	132	3
124.9	143	3
129.9	154	3
133.4	161	3
139.9	172	3
144.2	188	4
150.0	200	4
158.7	213	4
160.0	217	4
164.5	224	5
165.0	225	4

Table C.5: A_y data at $E_{\text{c.m.}}$= 1.69 MeV.

$\theta_{\text{c.m.}}$	A_y	ΔA_y
33.1	0.0456	0.0019
39.6	0.085	0.002
46.1	0.114	0.003
52.4	0.143	0.003
58.7	0.161	0.004
64.9	0.169	0.004
70.9	0.179	0.003
76.8	0.185	0.004
82.7	0.185	0.004
88.3	0.179	0.004
93.9	0.168	0.004
99.2	0.16	0.004
104.5	0.147	0.003
109.5	0.138	0.003
114.5	0.122	0.003
119.2	0.108	0.003
123.9	0.098	0.003
128.3	0.089	0.002
132.6	0.077	0.002
136.8	0.072	0.002
140.9	0.064	0.002
144.8	0.056	0.002
148.7	0.049	0.002
152.4	0.045	0.002
156.1	0.040	0.002

Table C.6: $\sigma(\theta)$ data at $E_{\text{c.m.}}$= 2.33 MeV.

$\theta_{\text{c.m.}}$	$\sigma(\theta)$	$\Delta\sigma(\theta)$	$\theta_{\text{c.m.}}$	$\sigma(\theta)$	$\Delta\sigma(\theta)$
29.9	162	4	109.9	102	1.7
41.3	121.3	1.9	119.9	125	3
49.9	113	2	129.9	159	3
59.9	103	2	139.9	185	3
65.8	92.1	1.5	144.3	203	3
69.9	90.2	1.5	149.9	219	4
79.9	84.5	1.6	158.7	246	4
89.9	82.6	1.4	160.0	248	4
99.9	92.1	1.5			

Table C.7: A_y data at $E_{\text{c.m.}}$= 2.35 MeV.

$\theta_{\text{c.m.}}$	A_y	ΔA_y	$\theta_{\text{c.m.}}$	A_y	ΔA_y
26.6	0.079	0.002	109.6	0.247	0.002
33.1	0.132	0.002	114.5	0.217	0.003
39.6	0.152	0.002	119.2	0.199	0.003
46.1	0.166	0.003	123.9	0.1741	0.0018
52.4	0.187	0.002	128.3	0.155	0.002
58.7	0.206	0.002	132.7	0.1310	0.0019
64.9	0.2275	0.0018	136.8	0.1118	0.0013
70.9	0.257	0.002	140.9	0.1001	0.0012
76.9	0.277	0.002	144.9	0.0894	0.0015
82.7	0.298	0.004	148.7	0.0751	0.0015
88.3	0.308	0.004	152.4	0.0652	0.0015
93.9	0.301	0.004	156.1	0.0547	0.0015
99.2	0.290	0.003	159.6	0.0482	0.0015
104.5	0.270	0.003			

Table C.8: $\sigma(\theta)$ data at $E_{\text{c.m.}}$= 3.02 MeV.

$\theta_{\text{c.m.}}$	$\sigma(\theta)$	$\Delta\sigma(\theta)$	$\theta_{\text{c.m.}}$	$\sigma(\theta)$	$\Delta\sigma(\theta)$
30.5	176	2	124.9	123	2
41.3	166.2	1.8	129.9	138.8	1.5
49.9	137	3	133.4	154	2
59.9	117	3	139.9	175	2
65.8	112.3	1.2	144.3	193	2
69.9	99	1.8	149.9	214	2
79.9	80.4	1.5	158.7	241	3
89.9	69.6	0.9	159.9	246	3
99.9	70.0	1.0	164.5	254	4
109.9	82.3	1.0	165.0	258	3
119.9	105.3	1.9			

Table C.9: A_y data at $E_{\text{c.m.}}$= 3.03 MeV.

$\theta_{\text{c.m.}}$	A_y	ΔA_y	$\theta_{\text{c.m.}}$	A_y	ΔA_y
26.6	0.103	0.004	109.6	0.360	0.007
33.1	0.103	0.003	114.5	0.324	0.007
39.6	0.1094	0.0019	119.3	0.284	0.006
46.1	0.115	0.002	123.9	0.249	0.005
52.4	0.125	0.003	128.3	0.226	0.005
58.7	0.143	0.0018	132.7	0.193	0.004
64.9	0.174	0.003	136.9	0.166	0.004
70.9	0.206	0.005	140.9	0.139	0.002
76.9	0.255	0.003	144.9	0.119	0.002
82.7	0.301	0.006	148.7	0.1022	0.0018
88.3	0.353	0.008	152.4	0.090	0.003
93.9	0.384	0.005	156.1	0.075	0.002
99.3	0.396	0.008	159.6	0.062	0.002
104.5	0.381	0.008	166.6	0.0325	0.0016

REFERENCES

[All93a] M. T. Alley and L. D. Knutson, Phys. Rev. C **48**, 1890 (1993).

[All93b] M. T. Alley and L. D. Knutson, Phys. Rev. C **48**, 1901 (1993).

[Alt70] E. O. Alt, P. Grassberger, and W. Sandhas, Phys. Rev. C **1**, 85 (1970).

[Aud93] G. Audi and A. H. Wapstra, Nucl. Phys. **A565**, 19 (1993).

[Bah98] J. N. Bahcall, S. Basu, and M. H. Pinsonneault, Phys. Lett. **B433**, 1 (1998).

[Bar81] P. H. Barker et al., 1981, Second International Conference on Precision Measurements and Fundamental Constants, Gaithersburg MD.

[Bar02] B. R. Barrett, P. Navratil, and J. P. Vary, Nucl. Phys. **A704**, 254 (2002).

[Bec82] H. W. Becker, L. Buchmann, J. Görres, K. U. Kettner, H. Krwinkel, C. Rolfs, P. Schmalbrock, H. P. Trautvetter, and A. Vlieks, Nucl. Instr. Meth. **198**, 277 (1982).

[Bed02] P. F. Bedaque and U. van Kolck, Annu. Rev. Nucl. Part. Sci. **52**, 339 (2002).

[Bel85] L. Beltramin, R. D. Frate, and G. Pisent, Nucl. Phys. **A442**, 266 (1985).

[Ber80] H. Berg, W. Arnold, E. Huttel, H. H. Krause, J. Ulbricht, and G. Clausnitzer, Nucl. Phys. **A334**, 21 (1980).

[Ber90] J. R. Bergervoet, P. C. van Campen, R. A. M. Klomp, J. L. de Kok, T. A. Rijken, V. G. J. Stoks, and J. J. de Swart, Phys. Rev. C **41**, 1435 (1990).

[Bev92] P. R. Bevington and D. K. Robinson, *Data Reduction and Error Analysis for the Physical Sciences*, McGraw-Hill, New York, second edition, 1992.

[Bit79a] G. Bittner and W. Kretschmer, Phys. Rev. Lett. **43**, 330 (1979).

[Bit79b] G. Bittner, W. Kretschmer, and W. Schuster, Nucl. Instr. Meth. **161**, 1 (1979).

[Bit79c] G. Bittner, W. Kretschmer, and W. Schuster, Nucl. Instr. Meth. **167**, 1 (1979).

[Bit87] M. Bittcher, W. Gruebler, V. Konig, P. Schmelzbach, B. Vuaridel, W. Schuster, K. Geissdorfer, W. Kretschmer, S. List, A. Rauscher, R. Schmitt, and G. Zeitler, Helv. Phys. Acta **60**, 77 (1987).

[Bla52] J. M. Blatt and L. C. Biedenharn, Rev. Mod. Phys. **24**, 258 (1952).

[Bla95] T. C. Black, Ph.D. thesis, University of North Carolina at Chapel Hill, 1995, Available from University Microfilms, Ann Arbor, Michigan. Document 1078067.

[Bla00] T. C. Black, 2000, private communication.

[Bla03] T. C. Black, 2003, private communication.

[Bos72] M. Bosterli and G. Hale, Phys. Rev. Lett. **28**, 1285 (1972).

[Bre75] H. Breuer and H. P. Morsch, Nucl. Phys. **A255**, 449 (1975).

[Bro52] R. J. S. Brown, G. D. Freier, H. D. Holmgren, W. R. Stratton, and J. L. Yarnell, Phys. Rev. **88**, 253 (1952).

[Bru98] C. R. Brune, W. H. Geist, H. J. Karwowski, E. J. Ludwig, K. D. Veal, M. H. Wood, A. Kievsky, S. Rosati, and M. Viviani, Phys. Lett. B **428**, 13 (1998).

[Bru01] C. R. Brune, W. H. Geist, H. J. Karwowski, E. J. Ludwig, K. D. Veal, M. H. Wood, A. Kievsky, S. Rosati, and M. Viviani, Phys. Rev. C **63**, 044013 (2001).

[Can00] R. S. Canon, 2000, private communication.

[Can01] W. Canton and W. Schadow, Phys. Rev. C **64**, 031001 (2001).

[Car83] J. Carlson, V. R. Pandharipande, and R. B. Wiringa, Nucl. Phys. **A401**, 59 (1983).

[Car91] J. Carlson, D. O. Riska, R. Schiavilla, and R. B. Wiringa, Phys. Rev. C **44**, 619 (1991).

[Car98] J. Carlson and R. Schiavilla, Rev. Mod. Phys. **70**, 743 (1998).

[Car01] J. Carbonell, Nucl. Phys. **A684**, 218c (2001).

[Cle64] T. B. Clegg, A. C. L. Barnard, J. B. Swint, and J. L. Weil, Nucl. Phys. **50**, 621 (1964).

[Cle95] T. B. Clegg, H. J. Karwowski, S. K. Lemieux, R. W. Sayer, E. R. Crosson, W. M. Hooke, C. R. Howell, H. W. Lewis, A. W. Lovette, H. J. Pfutzner, K. A. Sweeton, and W. S. Wilburn, Nucl. Instr. Meth. **A357**, 200 (1995).

[Cle02] T. B. Clegg, T. V. Daniels, B. Driehuys, M. Fassler, T. Katabuchi, J. Nouls, and H. P. gen. Schieck, in *TUNL Progress Report*, volume XLI, page 124, 2002.

[Coe83] H. T. Coelho, T. K. Das, and M. R. Robilotta, Phys. Rev. C **28**, 1812 (1983).

[Col63] F. D. Colegrove, L. D. Schearer, and G. K. Walters, Phys. Rev. **132**, 2561 (1963).

[Coo79] S. A. Coon, M. D. Scadron, P. C. McNamee, B. R. Barrett, D. W. E. Blatt, and B. H. J. McKellar, Nucl. Phys. **A317**, 242 (1979).

[Det79] J. R. Detomo, H. W. Clark, L. J. Dries, J. L. Regner, and T. R. Donoghue, Nucl. Phys. **A313**, 269 (1979).

[Dod77] D. C. Dodder, G. M. Hale, N. Jarmie, J. H. Jett, J. P. W. Keaton, R. A. Nisley, and K. White, Phys. Rev. C **15**, 518 (1977).

[Dri66] L. Drigo, C. Manduchi, G. C. Nardelli, M. T. Russo-Manduchi, G. Tornielli, and G. Zannoni, Nucl. Phys. **89**, 632 (1966).

[Dwu] DWUCK4 DWBA Computer Code, P. D. Kunz, University of Colorado at Boulder, `http://spot.colorado.edu/~kunz/DWBA.html`, unpublished.

[End90] P. M. Endt, Nucl. Phys. **A521**, 1 (1990).

[Ent02] D. R. Entem, R. Machleidt, and H. Witała, Phys. Rev. C **65**, 064005 (2002).

[Epe01] E. Epelbaum, H. Kamada, A. Nogga, H. Witała, W. Glöckle, and Ulf-G. Meißner, Phys. Rev. Lett. **86**, 4787 (2001).

[Epe02] E. Epelbaum, A. Nogga, W. Glöckle, H. Kamada, Ulf-G. Meißner, and H. Witała, Phys. Rev. C **66**, 064001 (2002).

[Fam54] K. F. Famularo, R. J. S. Brown, H. D. Holmgren, and T. F. Stratton, Phys. Rev. **93**, 928 (1954).

[Fer87] L. S. Ferreira, A. C. Fonseca, and L. Streit, editors, *Models and Methods in Few-Body Physics*, Berlin, 1987, Proceedings of the 8th Autumn Summer School on the Models and Methods in Few-Body Physics, Lisboa, Portugal, Springer-Verlag.

[Fil00] I. N. Filikhin and S. L. Yakovlev, Phys. At. Nucl. **63**, 69 (2000).

[Fis97a] B. M. Fisher, "Progress Towards a 52°-Line Magnet Calibration", TUNL internal report, 1997.

[Fis97b] B. M. Fisher, W. H. Geist, H. J. Karwowski, and E. J. Ludwig, in *TUNL Progress Report*, volume XXXVI, page 142, 1997.

[Fis98] B. M. Fisher, H. J. Karwowski, E. J. Ludwig, D. W. Schiber, and M. H. Wood, in *TUNL Progress Report*, volume XXXVII, page 134, 1998.

[Fis99] B. M. Fisher, A. B. Danner, C. R. Brune, H. J. Karwowski, D. S. Leonard, E. J. Ludwig, G. W. Milanovich, and M. H. Wood, in *TUNL Progress Report*, volume XXXVIII, page 142, 1999.

[Fis00] B. M. Fisher, T. C. Black, C. R. Brune, H. J. Karwowski, D. S. Leonard, E. J. Ludwig, G. W. Milanovich, and M. H. Wood, in *TUNL Progress Report*, volume XXXIX, page 132, 2000.

[Fra55] R. M. Frank and J. L. Gammel, Phys. Rev. **99**, 1406 (1955).

[Fra80] P. L. France and P. Winternitz, J. Phys (Paris) **41**, 1391 (1980).

[Fri99] J. L. Friar, D. Hüber, and U. van Kolck, Phys. Rev. C **59**, 53 (1999).

[Fuk99] Y. Fukuda et al., Phys. Rev. Lett **82**, 2430 (1999).

[Gei98] W. H. Geist, Ph.D. thesis, University of North Carolina at Chapel Hill, 1998, Available from University Microfilms, Ann Arbor, Michigan. Document #9902466.

[Geo98] E. A. George, 1998, private communication.

[Geo03] E. A. George and L. D. Knutson, Phys. Rev. C **67**, 027001 (2003).

[Glö83] W. Glöckle, *The Quantum Mechanical Few-Body Problem*, Springer-Verlag, Berlin, 1983.

[Glö96] W. Glöckle, H. Witała, D. Hüber, H. Kamada, and J. Golak, Phys. Rep. **274**, 107 (1996).

[Gre96] W. Greiner and J. A. Maruhn, *Nuclear Models*, Springer, Berlin, 1996.

[Gup02] D. Gupta, T. C. Black, and E. J. Ludwig, in *TUNL Progress Report*, volume XLI, page 126, 2002.

[Guz03] M. T. Guzy, 2003, private communication.

[Hab67] W. Haberli, Annu. Rev. Nucl. Sci. **17**, 373 (1967).

[Har76] R. A. Hardekopf and D. D. Armstrong, Phys. Rev. C **13**, 900 (1976).

[How01] C. R. Howell, Nucl. Phys. **A689**, 298c (2001).

[Hüb98] D. Hüber and J. L. Friar, Phys. Rev. C **58**, 674 (1998).

[Ima75] K. Imai, K. Nisimura, N. Tamura, and K. Sato, Nucl. Phys. **A246**, 76 (1975).

[Jam94] F. James, MINUIT*: Function Minimization and Error Analysis Reference Manual*, 1994, CERN, `wwwinfo.cern.ch/asdoc/minuit/minmain.html`.

[Jia92] M. F. Jiang, R. Machleidt, D. B. Stout, and T. T. S. Kuo, Phys. Rev. C **46**, 910 (1992).

[Kav66] R. W. Kavanagh and P. D. Parker, Phys. Rev. **143**, 780 (1966).

[Kie93] A. Kievsky, M. Viviani, and S. Rosati, Nucl. Phys. **A551**, 241 (1993).

[Kie94] A. Kievsky, M. Viviani, and S. Rosati, Nucl. Phys. **A577**, 511 (1994).

[Kie95] A. Kievsky, M. Viviani, and S. Rosati, Phys. Rev. C **52**, R15 (1995).

[Kie96] A. Kievsky, S. Rosati, W. Tornow, and M. Viviani, Nucl. Phys. **A607**, 402 (1996).

[Kie97] A. Kievsky, Nucl. Phys. **A624**, 125 (1997).

[Kie99] A. Kievsky, Phys. Rev. C **60**, 034001 (1999).

[Kie01] A. Kievsky, M. H. Wood, C. R. Brune, B. M. Fisher, H. J. Karwowski, D. S. Leonard, E. J. Ludwig, , S. Rosati, , and M. Viviani, Phys. Rev. C **63**, 024005 (2001).

[Kne66] D. J. Knecht, P. F. Dahl, and S. Messelt, Phys. Rev. **148**, 1031 (1966).

[Koi78] Y. Koike and J. Haidenbaurer, Nucl. Phys. **A463**, 356c (1978).

[Kre80a] P. Kreisler, W. Tietsch, and K. Bethge, Nucl. Instr. Meth. **177**, 521 (1980).

[Kre80b] W. Kretschmer, G. Pröbstle, and W. Stach, Nucl. Phys. **A333**, 13 (1980).

[Lac80] M. Lacombe, B. Loiseau, J. M. Richard, R. V. Mau, J. Côté, P. Pirés, and R. de Tourreil, Phys. Rev. C **21**, 861 (1980).

[Leo98] D. Leonard et al., in *TUNL Progress Report*, volume XXXVII, page 125, 1998.

[Leo02] D. S. Leonard, C. R. Brune, M. M. Fisher, H. J. Karwowski, E. J. Ludwig, G. W. Milanovich, and M. H. Wood, Bull. Am. Phys. Soc. **47**, 214 (2002).

[Low54] R. W. Lowen, Phys. Rev. **96**, 826 (1954).

[Mac87] R. Machleidt, K. Holinde, and C. Elster, Phys. Rep. **149**, 1 (1987).

[Mac01] R. Machleidt, Phys. Rev. C **63**, 024001 (2001).

[Mad71] in *Proceedings of the Third International Symposium on Polarization Phenomena in Nuclear Reactions*, edited by H. H. Barschall and W. Haeberli, page xxv, Madison, Wisconsin, 1971.

[Mar66] J. B. Marion, Rev. Mod. Phys. **38**, 660 (1966).

[Mar00a] L. E. Marcucci, R. Schiavilla, M. Viviani, A. Kievsky, and S. Rosati, Phys. Rev. Lett. **84**, 5959 (2000).

[Mar00b] L. E. Marcucci, R. Schiavilla, M. Viviani, A. Kievsky, S. Rosati, and J. F. Beacom, Phys. Rev. C **63**, 015801 (2000).

[Mar00c] L. E. Marcucci, Nucl. Phys. **A689**, 280c (2000).

[Mat00] M. Matsuda, J. Nagata, H. Yoshino, and Y. Yoshino, Comp. Phys. Comm. **131**, 264 (2000).

[McD64] D. G. McDonald, W. Haberli, and L. W. Morrow, Phys. Rev. **133**, B1178 (1964).

[McS69] D. H. McSherry, S. D. Baker, G. R. Plattner, and T. B. Clegg, Nucl. Phys. **A126**, 233 (1969).

[McS70] D. H. McSherry and S. D. Baker, Phys. Rev. C **1**, 888 (1970).

[Men96] A. J. Mendez, C. D. Roper, J. D. Dunham, and T. B. Clegg, Rev. Sci. Inst. **67**, 3073 (1996).

[Mer98] E. Merzbacher, *Quantum Mechanics*, John Wiley and Sons, New York, third edition, 1998.

[Mor69] L. W. Morrow and W. Haberli, Nucl. Phys. **A126**, 225 (1969).

[Nay77] H. Naylor et al., Nucl. Inst. and Meth. **144**, 331 (1977).

[Nei03] E. M. Neidel, W. Tornow, D. E. González Trotter, C. R. Howell, A. S. Crowell, R. A. Macri, R. L. Walter, G. J. Weisel, J. Esterline, H. Witała, B. J. C. III, R. S. Pedroni, and D. M. Markoff, Phys. Lett. **B552**, 29 (2003).

[Nog00] A. Nogga, H. Kamada, and W. Glöckle, Phys. Rev. Lett. **85**, 944 (2000).

[Nog02] A. Nogga, H. Kamada, W. Glöckle, and B. R. Barrett, Phys. Rev. C **65**, 054003 (2002).

[Nog03] A. Nogga, A. Kievsky, H. Kamada, W. Glöckle, L. E. Marcucci, S. Rosati, and M. Viviani, Phys. Rev. C **67**, 043004 (2003).

[Ohl73] G. G. Ohlsen and P. W. Keaton, Jr., Nucl. Instr. Meth. **109**, 41 (1973).

[Pfi01] B. Pfitzinger, H. M. Hofmann, and G. M. Hale, Phys. Rev. C **64**, 044003 (2001).

[Pig94] M. Pignone, M.Lacombe, and B. Loiseau, Phys. Rev. C **50**, 2710 (1994).

[Pud95] B. S. Pudliner, V. R. Pandharipande, J. Carlson, and R. B. Wiringa, Phys. Rev. Lett. **74**, 4396 (1995).

[Rei03] C. Reißand H. M. Hofmann, arXiv:nucl-th/0301043, 2003.

[Ren99] M. C. M. Rentmeester, R. G. E. Timmermans, J. L. Friar, and J. J. de Swart, Phys. Rev. Lett. **82**, 4992 (1999).

[Roo03] "ROOT Application Framework", 2003, `http://root.cern.ch/`.

[Sai03] SAID PWA Analysis Code, The George Washington University, online version at `http://gwdac.phys.gwu.edu/`, 2003.

[Sch92] R. Schiavilla, R. B. Wiringa, V. R. Pandharipande, and J. Carlson, Phys. Rev. C **45**, 2628 (1992).

[Set95] R. Setze et al., *XSYS Reference Manual*, 1995, TUNL internal report.

[Sha85] D. Shapria, J. L. C. Ford, R. Novotny, B. Shicakumar, R. L. Parks, and S. T. Thornton, Nucl. Instr. Meth. **228**, 259 (1985).

[Sto78] C. Stolk and J. A. Tjon, Nucl. Phys. **A295**, 384 (1978).

[Sto93] V. G. J. Stoks, R. A. M. Klomp, M. C. M. Rentmeester, and J. J. de Swart, Phys. Rev. C **48**, 792 (1993).

[Sto94] V. G. J. Stoks, R. A. M. Klomp, C. P. F.Terheggen, and J. J. de Swart, Phys. Rev. C **49**, 2950 (1994).

[Swa53] P. Swan, Proc. Phys. Soc. A **66**, 740 (1953).

[Sza78a] G. Szaloky, F. Seiler, W. Grübler, and V. König, Nucl. Phys. **A303**, 51 (1978).

[Sza78b] G. Szaloky and F. Seiler, Nucl. Phys. **A303**, 57 (1978).

[Teg83] P. E. Tegnèr and C. Bargholtz, Astrophs. J. **272**, 311 (1983).

[Tho72] P. A. Thompson, *Compressible-Fluid Dynamics*, McGraw-Hill, New York, 1972.

[Tie79] W. Tietsch, K. Bethge, H. Feist, and E. Schopper, Nucl. Instr. Meth. **158**, 41 (1979).

[Til92] D. R. Tilley, H. R. Weller, and G. M. Hale, Nucl. Phys. **A541**, 1 (1992).

[Tom62] T. A. Tombrello, C. M. Jones, G. C. Phillips, and J. L. Weil, Nucl. Phys. **39**, 541 (1962).

[Tom65] T. A. Tombrello, Phys. Rev. **138**, B40 (1965).

[Tor98] W. Tornow, H. Witała, and A. Kievsky, Phys. Rev. C **57**, 555 (1998).

[Tor02] W. Tornow, 2002, private communication.

[Viv95] M. Viviani, A. Kievsky, and S. Rosati, Few Body Systems **18**, 25 (1995).

[Viv98] M. Viviani, A. Kievsky, and S. Rosati, Phys. Rev. Lett. **81**, 1580 (1998).

[Viv01] M. Viviani, A. Kievsky, S. Rosati, E. A. George, and L. D. Knutson, Phys. Rev. Lett. **86**, 3739 (2001).

[Viv02] M. Viviani, 2002, private communication.

[Viv03] M. Viviani, 2003, private communication.

[Wei89] R. Weidmann, "Präzisionsmessung der Analysierskä rke in der Proton - Proton Streuung bei 25.6 MeV", 89, Diploma Thesis.

[Wil82] J. F. Wilkerson, Ph.D. thesis, University of North Carolina at Chapel Hill, 1982, Available from University Microfilms, Ann Arbor, Michigan. Document 3306181.

[Wil83] J. F. Wilkerson, T. B. Clegg, and E. J. Ludwig, Nucl. Inst. Meth. **207**, 331 (1983).

[Wir95] R. B. Wiringa, V. G. J. Stoks, and R. Schiavilla, Phys. Rev. C **51**, 38 (1995).

[Wir00] R. B. Wiringa, S. C. Pieper, V. R. Pandharipande, and J. Carlson, Phys. Rev. C **62**, 014001 (2000).

[Wir02] R. B. Wiringa and S. C. Pieper, Phys. Rev. Lett. **89**, 182501 (2002).

[Wit89] H. Witała, W. Glöckle, and T. Cornelius, Nucl. Phys. **A491**, 157 (1989).

[Wit91] H. Witała and W. Glöckle, Nucl. Phys. **A528**, 48 (1991).

[Wit94] H. Witała, D. Hüber, and W. Glöckle, Phys. Rev. C **49**, R14 (1994).

[Woo00] M. H. Wood, Ph.D. thesis, University of North Carolina at Chapel Hill, 2000, Available from University Microfilms, Ann Arbor, Michigan. Document #9979498.

[Woo02] M. H. Wood, C. R. Brune, B. M. Fisher, H. J. Karwowski, D. S. Leonard, E. J. Ludwig, A. Kievsky, S. Rosati, , and M. Viviani, Phys. Rev. C **65**, 034002 (2002).

[Yak69] O. A. Yakubovsky, Sov. J. Nucl. Phys. **5**, 937 (1969).

[Yos00] Y. Yoshino, V. Limkaisang, J. Nagata, H. Yoshino, and M. Matsuda, Prog. Theor. Phys. **103**, 107 (2000).

[Yuk35] H. Yukawa, Proc. Phys.-Math. Soc. Jpn Ser.3 **17**, 48 (1935).

[Zab80] T. H. Zabel, M. P. Fewell, D. C. Kean, R. H. Spear, and A. M. Baxter, Nucl. Instr. Meth. **174**, 459 (1980).

[Zie85] J. F. Ziegler, J. P. Biersack, and U. Littmark, *The Stopping and Range of Ions in Solids*, Pergamon Press, New York, 1985.